NOTE TO USERS

This reproduction is the best copy available.

uOttawa

L'Université canadienne
Canada's university

FACULTÉ DES ÉTUDES SUPÉRIEURES ET POSTOCTORALES

uOttawa

L'Université canadienne
Canada's university

FACULTY OF GRADUATE AND POSDOCTORAL STUDIES

Mehran Talebinejad

AUTEUR DE LA THÈSE / AUTHOR OF THESIS

Ph.D. (Electrical Engineering)

GRADE / DEGREE

School of Information Technology and Engineering

FACULTÉ, ÉCOLE, DÉPARTEMENT / FACULTY, SCHOOL, DEPARTMENT

Multi-Scale Analysis of Myoelectric Signals

TITRE DE LA THÈSE / TITLE OF THESIS

Ali Miri

DIRECTEUR (DIRECTRICE) DE LA THÈSE / THESIS SUPERVISOR

Adrian Chan

CO-DIRECTEUR (CO-DIRECTRICE) DE LA THÈSE / THESIS CO-SUPERVISOR

EXAMINATEURS (EXAMINATRICES) DE LA THÈSE / THESIS EXAMINERS

Martin Bouchard

James Green

Mohamed El-Tanany

Evelyn Morin

Gary W. Slater

Le Doyen de la Faculté des études supérieures et postdoctorales / Dean of the Faculty of Graduate and Postdoctoral Studies

MULTI-SCALE ANALYSIS OF MYOELECTRIC SIGNALS

BY

MEHRAN TALEBINEJAD

A THESIS IN PARTIAL FULFILMENT OF
THE REQUIREMENTS FOR THE DEGREE OF
DOCTOR OF PHILOSOPHY

THE OTTAWA-CARLETON INSTITUTE FOR
ELECTRICAL AND COMPUTER ENGINEERING (OCIECE)

SCHOOL OF INFORMATION TECHNOLOGY AND ENGINEERING (SITE)
UNIVERSITY OF OTTAWA
OTTAWA, ONTARIO, CANADA
2009

Your file Votre référence
ISBN: 978-0-494-51803-8
Our file Notre référence
ISBN: 978-0-494-51803-8

Abstract

The neuromuscular system is composed of multiple units with highly non-linear deterministic and random characteristics. Such systems generate complex signals that exhibit different characteristics when they are analyzed on different scales, known as multi-scale signals. The myoelectric signal, which is comprised of deterministic (i.e., structured) and random contributions, exhibits multi-scale characteristics. In this work, we present four major paradigms for multi-scale analysis of myoelectric signals; namely, *self-similarity*, *long memory*, *multi-fractality* and *chaos*.

Self-similarity: A novel multi-scale bi-phase power-law is introduced which accurately characterizes surface myoelectric signal power spectrum recorded during moderate contractions. We present a novel methodology, termed the bi-phase power spectrum method which provides unique parameters that are distinctly sensitive to force, joint angle, and fatigue. These parameters could be used as complementary information for conventional myoelectric parameters that are confounded during dynamic contractions.

Long memory: A method for quantitative analysis of long memory, known as detrended fluctuation analysis, is introduced in the context of myoelectric signals. We show the myoelectric signals show both mono- and multi-fractality. A new approach is presented to compute an optimum Hurst exponent for fatigue estimation.

Multi-fractality: A unique multi-fractal process known as multiplicative cascade multi-fractal is introduced in the context of myoelectric signals. A framework for analysis of myoelectric signals using this multi-fractal process is presented for discerning neuropathic conditions.

Chaos: An interesting framework known as power-law sensitivity to initial condition is used to analyze myoelectric signals. This new framework suggests the myoelectric signals are not fully random or fully chaotic but they resemble random fractals and chaotic motions on different scales. The Lempel-Ziv measure is introduced for quantitative analysis of deterministic complexity. We show the binary Lempel-Ziv measure might be affected by a false sense of complexity due to inadequacy of two symbols to characterize motor unit action potentials. A new ternary Lempel-Ziv measure is introduced which resolves limitations of the binary Lempel-Ziv measure. The Lempel-Ziv measure also provides unique characteristics well-suited for fatigue estimation.

We integrate these four aspects along with chaos and random fractal theory and provide a unified framework for multi-scale analysis of myoelectric signals.

Contents

List of figures

List of tables

List of abbreviations

AR ..... autoregressive

BPSM ..... bi-phase power spectrum method

CA ..... classification

CV ..... conduction velocity

DFA ..... detrended fluctuation analysis

eFD ..... estimated fractal dimension

EMG ..... electromyography

FBM ..... fractional Brownian motion

LP ..... linear predictive

LTI ..... linear time invariant

LZ ..... Lempel-Ziv

MCM ..... multiplicative cascade multi-fractal

MDN ..... median frequency

MES ..... myoelectric signal

MNF ..... mean frequency

MU ..... motor unit

MUAP ..... motor unit action potential

NT ..... number of turns

NZC ..... number of zero crossings

RMS ..... root mean square

SFAP ..... single fiber action potential

SNR ..... signal to noise ratio

STFT ..... short time Fourier transform

TVAR ..... time varying autoregressive

WSS ..... wide sense stationary

Chapter 1

1. Introduction

Muscle is a contractile tissue consisting of cellular components that have the ability of physical size transformation. The size transformation and contraction on a cellular level translates into movement and force production of muscles. The natural ability of muscles for movement and production of force, which is regulated through a complex interaction with the human motor nervous system (i.e., neuromuscular system), is evident in all aspects of human life, such as, breathing, heart activity, movement of the eyes and other organs.

Contraction of skeletal muscles involves bioelectrical phenomena within the smallest functional units of the neuromuscular system known as motor units (MUs). It is possible to record this electrical activity, invasively using needle electrodes directly from the muscle, or non-invasively using surface electrodes on the surface of the skin. The act of recording the electrical activity of the muscle is known as electromyography (EMG), and the obtained recording is known as the EMG signal or myoelectric signal (MES). It is preferred to use the term MES instead of EMG signal to avoid confusion between the act of recording and the recorded signal. Throughout this work the term MES is used for the recorded signal by convention.

Understanding the MES helps to understand the muscles and the way they generate bioelectrical signals. It also helps to understand how specific mechanisms and phenomena (e.g., muscle fatigue and neuromuscular disorders) influence the MES and how the MES reflects certain mechanisms and phenomena. This concept of forming a forward and inverse problem is familiar to engineers as a system analysis problem based on the input and output of the system. In this

case, the MES could be considered to be the output of neuromuscular system; meanwhile, information available from the input and the system are limited to physiological knowledge of the neuromuscular system. For example, one could examine the force produced by the muscle using the MES or study the progress of muscle fatigue (i.e., weakness). Figure 1.1, shows a simplified schematic of MES generation.

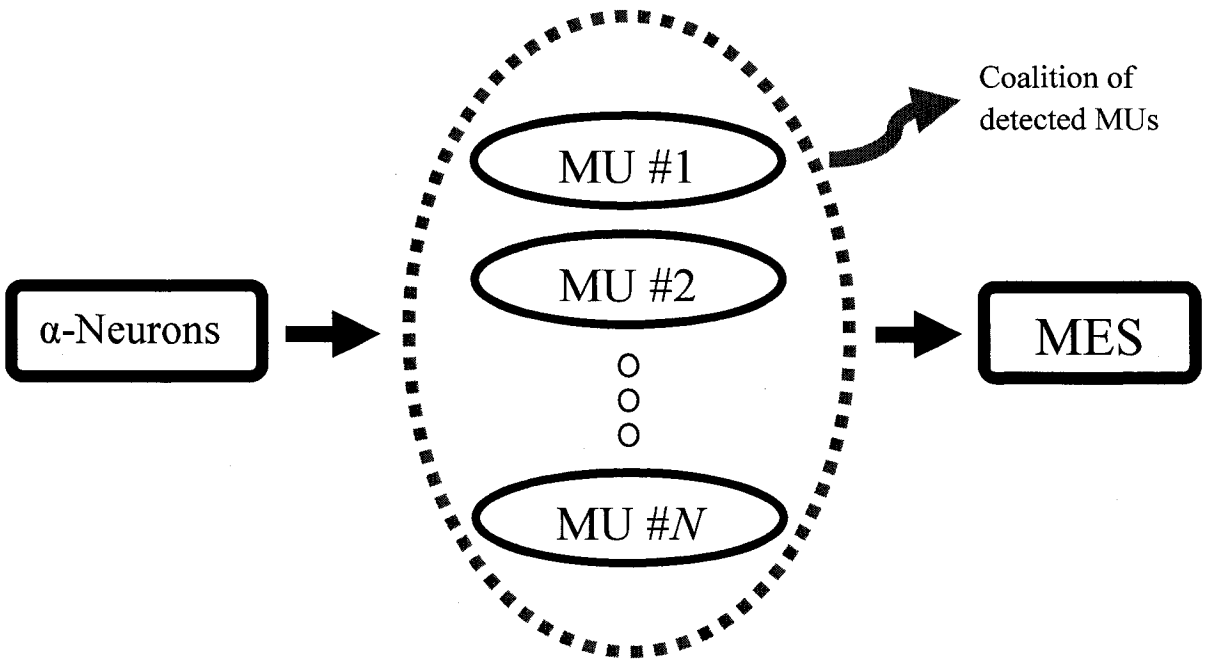

Figure 1.1: Schematics of MES generation.

The motor nervous system innervates a number of muscle fibres during a contraction. A MU consists of a α-motoneuron and the fibers it innervates. Innervated muscle fibers within a MU generate MU action potentials (MUAPs). The innervation process resembles random pulses that activate MUAPs with self-similar structures. The MES is the summation of MUAPs from a coalition of MUs, detected by an electrode.

Previously, MESs have been studied widely for physical medicine and rehabilitation [Merletti and Parker, 2004], neurophysiology and clinical diagnosis [Stalberg and Falck, 1997; Merletti and Parker, 2004], performance and fatigue studies [Farina *et al*, 2001], and recently augmented speech recognition [Chan *et al.*, 2006].

Analyses of MESs are based mainly on conventional measures that are routine and well-known for the analysis of generic biological signals; for example, spectral moments, percentile frequencies (e.g., median frequency (MDN)), linear predictive (LP) coefficients, cepstrum coefficients, wavelet coefficients, root mean square (RMS), number of zero crossings (NZC) and number of turns (NT) are well documented [Finsterer, 2001; Merletti and Parker, 2004].

The origins of the MES comprise multiple subsystems that exhibit both highly non-linear deterministic (i.e., MUs) and random (i.e., innervation) characteristics and are regulated hierarchically (i.e., regulations are distinct for each subsystem). The unique structure of the muscle and origins of the electrical activity suggest it would be very interesting to exploit these unique properties. It is expected that multi-scale characteristics would be exhibited in the MES; multi-scale signals behave differently depending upon the scale at which the data are examined.

One way to exploit the multi-scale characteristics in signal processing is to use existing generic measures at different time scales; however, it is very difficult to analyze a signal at all possible time scales because there can be an infinite number of different scenarios in which the signal must be studied. An alternative way is to develop multi-scale measures that explicitly incorporate the concept of scale and characterize the signal with scale-dependent information; in other words, measures that are able to characterize the signal and identify appropriate scales

simultaneously [Gao, 2000; Hu, 2007]. This type of analysis would be referred to as multi-scale analysis throughout this work.

Recently, there have been a few studies addressing multi-scale aspects of MESs but these are not explicitly under the umbrella of multi-scale analysis and within the category of fractal or chaotic time series analysis [Chang *et al.*, 2004; Gitter *et al.*, 1995; Gupta *et al.*, 1997; Raveir *et al.*, 2005; Shields, 2007; Talebinejad *et al.*, 2006a,b, 2007]. A major difficulty in this area of research is that conventional fractal and chaotic analysis borrowed from other areas of research are not well-defined for MESs. In order to fully characterize such complex signals, the concept of scale has to be explicitly considered, and existing theories need to be used collectively, instead of individually, since on different scale ranges different theories may be more relevant.

1.1. Objectives

In this work, we present a unified approach for multi-scale analysis of MESs. We integrate chaos and random fractal theory, and introduce new multi-scale techniques that can be used for characterizing MESs. These new techniques are compared to existing methodologies and several potential applications are illustrated.

1.2. Contributions

1.2.1. Major contributions

1. **Introduced a novel bi-phase power-law, for characterizing bi-phase multi-scale phenomena.** It is apparent in most biological signals that the multi-scale characteristics do not follow a mono-phase power-law similar to fractional Brownian motion (FBM). We present a novel bi-phase power-law which resembles an extended form of self-

similarity. The bi-phase power-law provides several interesting features such as distinct asymptotically independent fractional-orders and homomorphism. The power spectrum of the MES shows bi-phase characteristics especially during moderate contractions. We present a bi-phase power spectrum method (BPSM) applicable to MESs. It is illustrated that the unique features of the bi-phase power-law can be exploited for improved force and fatigue estimation. This contribution has resulted in the following publications:

1. Talebinejad M., Chan A., Miri A., and Dansereau R. (2008) Fractal analysis of surface electromyography signals: A novel power spectrum-based method. *Journal of Electromyography and Kinesiology*, doi:10.1016/j.jelekin.2008.05.004.
2. Talebinejad M., Chan A., Miri A. (2007) Effects of conduction velocity and spectral compression on the fractal parameters of myoelectric signals. *Proceedings of the 30th Canadian Medical and Biological Engineering Society Conference*, M0087.
3. Talebinejad M., Chan A., Miri A. (2008) Spectrum-based fractal analysis using piecewise statistically self-affine power-laws. *Proceedings of the 31st Canadian Medical and Biological Engineering Society Conference*, A8-3.
4. Talebinejad M., Chan A., Miri A. (2008) Novel power spectrum-based fractal indicators for myoelectric parameters. *Proceedings of the 17th Congress of International Society of Electrophysiology and Kinesiology*, SPO2-3.
5. Talebinejad M., Chan A., Miri A. (2008) Novel fractal indicators with distinct sensitivities to localized muscular fatigue during static contractions. *Proceedings of the 17th Congress of International Society of Electrophysiology and Kinesiology*, MFO1-5.

2. **Introduced a new approach for fatigue estimation using multi-fractal detrended fluctuation analysis (DFA).** Conventional fatigue indices are affected by factors other than fatigue during dynamic contractions (e.g., force and joint angle). We show that with the multi-fractal DFA, it is possible to find time scales at which the myoelectric manifestation of fatigue is more significant compared to other factors. Thus, it is possible to estimate muscle fatigue within these particular time scales more accurately. This approach has demonstrated improvement over the conventional MDN as a fatigue index. This contribution has resulted in the following publications:

    1. Talebinejad M., Chan A., and Miri A. (2008) Fatigue estimation using a novel multi-fractal detrended fluctuation analysis approach. Submitted to the *Journal of Electromyography and Kinesiology*, JEK-D-08-00127.
    2. Talebinejad M., Chan A., and Miri A. (2008) Multi-scale analysis of myoelectric signals: Assessment of long-range dependencies and fractal-scaling-breaks. *Proceedings of the 31st Canadian Medical and Biological Engineering Society Conference*, A4-5.

3. **Introduced a new framework for multiplicative cascade multi-fractal (MCM) modeling of MESs.** The MCM framework has unique characteristics such as primary sensitivity to long-range correlation, and suppressing the effects of noise. We exploit these characteristics and compute a new signal measure that could be used to discern between normal and neuropathic MESs. Using simulated MESs, we demonstrate this new measure outperforms the conventional NT in the presence of additive white Gaussian noise, in terms of classification accuracy. This contribution has been submitted for publication to the *IEEE Transaction on Biomedical Engineering* (Talebinejad M., Chan

A., and Miri A. (2008) Multiplicative multi-fractal modeling of electromyography signals for discerning neuropathic conditions. TBME-00789-2008).

4. **Introduced a new framework for fatigue estimation using Lempel-Ziv (LZ) complexity measure.** We show the LZ measure is sensitive to the changes of MESs due to fatigue and outperforms the conventional MDN for fatigue estimation. We also show the standard binary LZ measure might be affected by a false sense of complexity due to the inadequacy of a binary sequence to characterize MUAPs. We introduce a multi-level LZ measure and demonstrate that a ternary LZ measure outperforms the standard binary measure. This contribution has been submitted for publication to the *Journal of Electromyography and Kinesiology* (Talebinejad M., Chan A., and Miri A. (2008) Fatigue estimation using Lempel-Ziv complexity measure. JEK-D-08-00165).

1.2.2. Other contributions

1. **The existing literatures on fractal analysis of MESs are critically reviewed and the shortcomings and limitations of available methods are discussed.** We demonstrate that the estimated fractal dimension using the Katz and box-counting methods is highly correlated with the amplitude of the MESs and confounded. We also demonstrate the $1/f$ approach is not directly applicable to MESs. This contribution has been published in the *Journal of Electromyography and Kinesiology* (Talebinejad M., Chan A., Miri A., and Dansereau R. (2008) Fractal analysis of surface electromyography signals: A novel power spectrum-based method. doi:10.1016/j.jelekin.2008.05.004).
2. **The structure-function-based method and DFA are evaluated with MESs.** A comprehensive discussion on long memory (i.e., long-range-dependency and correlation) and fractal-scaling-break of MESs is presented. We demonstrate the conventional mono-

fractal approaches (e.g., mono-phase power spectrum method) are ill-defined for analysis of MESs as this signal exhibits both mono- and multi-fractality. This contribution has been submitted for publication to the *Journal of Electromyography and Kinesiology* (Talebinejad M., Chan A., and Miri A. (2008) Fatigue estimation using a novel multi-fractal detrended fluctuation analysis approach. JEK-D-08-00127).

3. **We have shown that the MESs are not fully random or fully chaotic, but they resemble random fractals and chaotic motions when analyzed at specific time scales.** We extend the concept of exponential sensitivity to the initial condition, to power-law sensitivity and time-dependent exponent curves and determine the edge of chaos (i.e., distinctive time scale relations between a random fractal and a chaotic motion) for a MES.

1.3 Thesis structure

In chapter 2, the basic physiology of the muscle and state of the art in analysis of MESs for different applications are presented along with a summary of selected previous research on force and fatigue estimation, myoelectric prosthetic control, myoelectric augmented speech recognition, and clinical diagnosis.

In chapter 3, multi-scale phenomena are introduced; four major paradigms for multi-scale analysis including *self-similarity*, *long-memory*, *multi-fractality*, and *chaos* are presented. These paradigms are discussed in the context of MESs and available literature in this area, is reviewed. DFA, MCM, and power-law sensitivity to initial condition are introduced in this chapter.

In chapter 4, the simulated needle MESs, as well as, experimental data used in this work, are presented; these data include surface MESs recorded during different contraction and fatigue protocols.

In chapter 5, a novel bi-phase power-law and the BPSM are introduced and a human experiment is presented. It is demonstrated that the fractional-orders of BPSM show distinct sensitivities to force, muscle length (joint angle), and fatigue.

In Chapter 6, a new approach for fatigue estimation using multi-fractal DFA is introduced, and results of a fatigue experiment, during static, cyclic and random contractions, are presented.

In Chapter 7, a new framework for MCM modeling of MESs and discerning between normal and neuropathic conditions with results of a simulation study are presented.

In Chapter 8, the LZ measure is introduced, and a new framework for analysis of MESs using LZ measure is presented. Results of a fatigue experiment are also presented.

Chapter 9, lays out the conclusions and future directions in this area of research. Appendices and references are included at the end of the thesis.

Chapter 2

2. Physiology, biophysics and analysis of MESs

MESs generated by skeletal muscles, incorporate central control strategies, signal transmission along nerve fibers and across neuromuscular junction, and electrical activation of the muscle fibers organized in MUs. Figure 2.1, illustrates simplified schematics of the neuromuscular system.

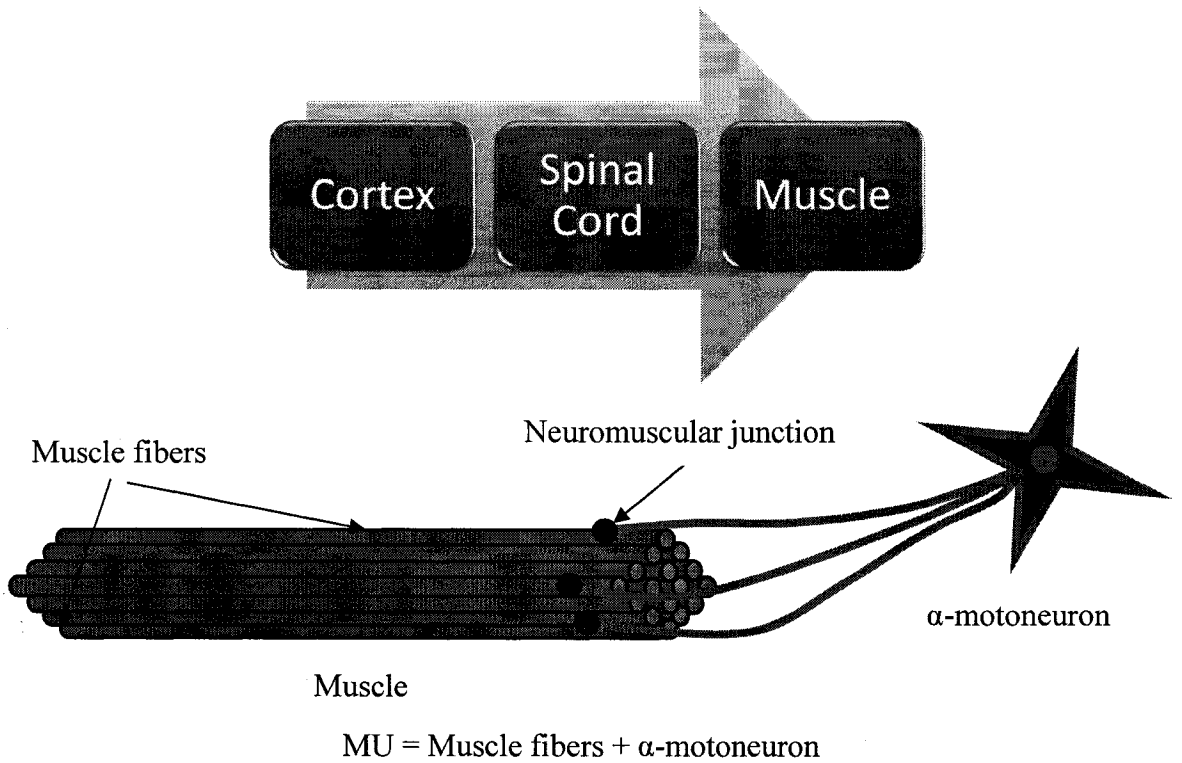

Figure 2.1: A schematic representation of the neuromuscular system.

This chapter is dedicated to: 1) physiology and biophysics behind motor control and muscle contraction, 2) MES detection techniques, and 3) state of the art in MES analysis and applications.

2.1. Basic physiology of motor control and muscle contraction

The central nervous system controls the skeletal muscles by motor programming which takes place in different areas of the cortex. The corticospinal tract is linked to α-motoneurons which are directly controlling the muscle activity. A MU consists of a α-motoneuron in the spinal cord and the muscle fibers it innervates. The number of MUs per muscle in humans may range from about 100 for a small hand muscle to 1000 or more for large limb muscles [Merletti and Parker, 2004]. Earlier studies [Burk, 1981] identified three types of MUs based on physiological properties: 1) fast-twitch with high sensitivity to fatigue, 2) fast-twitch fatigue-resistant, and 3) slow-twitch which is the most resistant to fatigue. The distinct characteristics of different types of MUs are mainly a function of muscle fiber physiological properties and sensitivity to different enzymes and biological by-products, which determine the speed of the force twitch and fatigability.

2.1.1. Isometric contractions

During a contraction, force is regulated by the number of active MUs (i.e., spatial recruitment), and MU activation frequency or firing rate (i.e., temporal recruitment). The greater the number of MUs recruited and the higher the discharge frequency, the greater the produced force will be. The current understanding of MU recruitment is based on the pioneering work of Henneman *et al.*, in the 1960s, who proposed that MUs are always recruited in order of increasing size of the α-motoneurons [Henneman *et al.*, 1960]. This theory known as the *size principle* is well accepted and documented and is often referred to as orderly recruitment.

It is well documented that MU recruitment and firing rate depend primarily on the level of force and speed of a contraction. When low threshold MUs are recruited, muscular contraction is characterized by low force generating capabilities and high fatigue resistance. With requirement for greater force and/or faster contractions, high threshold fatigable MUs are recruited.

The number of active MUs and their firing rate are primarily responsible for the level of force and it is expected that the MES shows direct relationship to these parameters. Indeed, under isometric experimental conditions without fatigue considerations, it is possible to demonstrate that, MES amplitude or the RMS value of the signal show a strong correlation to the level of force (i.e., $r = 0.97\text{-}0.99$ [Merletti and Parker, 2004]).

However, a change in MES should not be automatically attributed to changing spatial and temporal recruitment and force level; the speed of the contraction, the capability of muscle fibers for producing a twitch, and muscle fatigue also influence the myoelectric dynamics and MES.

2.1.2. Dynamic contractions

During dynamic contractions, the physical shape of the muscles varies with movement. This variation affects the capacity of the muscle fibers for force production; that is, the recruitment parameters will also vary when the muscle shape and length (joint angle) is changed to produce a constant amount of force. Meanwhile, muscle movement will also affect the relative location of the innervation zone and the electrode.

Therefore, during a dynamic contraction, without muscle fatigue, the MES will reflect both changes in the level of force and the physical shape of the muscle. In this case, the amplitude or

the RMS is confounded by both mechanisms. It is possible to demonstrate that a simple correlation between the level of force and RMS is not anticipated during dynamic contractions.

2.1.3. Muscle fatigue

Some previous studies [Merletti and Parker, 2004] have shown that the amplitude of MESs increases progressively as a function of time during sustained fatiguing contractions. Although this phenomenon is widely accepted it is not universal and there have been studies in which the amplitude has not increased or decreased [Merletti and Parker, 2004]. It was generally assumed that additional MUs are progressively recruited to compensate for the loss of contractility due to MUs fatigue impairment in cases the amplitude was increased. However, this assumption was simplistic, because it was not possible to justify the muscle's capability to evolve, adapt, and repair itself, or explain cases where the amplitude is not increasing. This led to more in depth research on fatigue.

In common language, fatigue could be described as a feeling or sensation of weakness, or muscle pain or a decrement of performance, which is not particularly suitable for quantification or measurement. A quantitative approach to describing muscle fatigue is often associated with an event such as the inability to continue to perform a task. The engineering approach to fatigue of a material or a mechanism is different with assessment of muscle fatigue, because fatigue is not an irreversible process in the muscle. There are many potential sites of fatigue in the neuromuscular system which could be grouped into three major categories [Merletti and Parker, 2004]: 1) central fatigue, associated with the cortex and spinal cord, 2) fatigue of the neuromuscular junction, and 3) muscle fatigue. All these factors contribute to changes of MES in very complex ways that are not easy to unscramble. To reduce the difficulty of the problem and the number of

factors affecting MES most past research has focused on myoelectric manifestation of muscle fatigue during isometric (constant length), isotonic (constant force) contractions [Merletti and Parker, 2004]. A very restricted contraction protocol is not however reflective of muscle function in daily life and fatigue estimation during dynamic contractions is a major challenge in this area of research [Merletti *et al.*, 2002].

2.1.3.1. Assessment of muscle fatigue

Fatigue is not a physical variable and its assessment requires the definition of indexes related to other measurable variables. In previous studies [Merletti and Parker, 2004], several different indexes have been suggested for measurement of fatigue based on MES analysis. Indexes of fatigue are defined on the basis of the time evolution of the MES; that is, muscle fatigue can be assessed since the very beginning of a muscle contraction.

The most widely used and documented muscle fatigue indexes are based on observed changes of MES conduction velocity (CV). Muscle fiber CV decreases as the contraction progresses in time due to several different mechanisms including accumulation of biological by-products such as acid lactic in the muscle [De Luca, 1984]. This feature is better described in the frequency domain for a stochastic signal like the MES; it was observed that the frequency content of the MES shifts towards lower frequencies as a result of slowing MES. This shift is often tracked using the mean frequency (MNF), or the 50^{th} percentile frequency also known as the MDN [De Luca, 1984].

Fatigue indexes based on the frequency domain MES features are the most commonly used measures for assessment of muscle fatigue [MacIsaac *et al.*, 2006; Merletti and Parker, 2001]. Advances in muscle fatigue estimation will be presented in section 2.4.2.

2.1.4. Neuromuscular disorders

The MES could be also affected by the nervous system or muscle diseases. In this work we limit our scope to one well-known category of neuromuscular disorders, neuropathy. Neuropathy is usually associated with a reduced number of active MUs and reorganization of the muscle fibers to form larger MUs [Stalberg and Falck, 1997]. It is also of interest to discriminate normal, and neuropathic conditions automatically from the MES. Advances in clinical diagnosis will be presented in section 2.5.3.

2.2. Detection techniques

Detection techniques can be divided to two main categories: invasive intramuscular recordings and non-invasive surface recordings.

2.2.1. Intramuscular recordings

Various needle electrodes have been designed for intramuscular recording [Stalberg and Falck, 1997]. Intramuscular needle electrodes are used to make extracellular recordings of MUAPs and muscle fiber action potentials. It is also possible to record the intercellular potentials *in vitro* which are out of the scope of this work.

Typically the recorded signal's amplitude exponentially decreases as the distance between the electrode tip and the muscle fibers increases; thus, the contribution of individual single muscle

fiber action potentials to the recorded MUAP is greatly influenced by the electrode location and shape. Electrodes with small recording surfaces are more selective; conversely, electrodes with larger recording surfaces are less selective and make record from a larger area with smaller amplitudes.

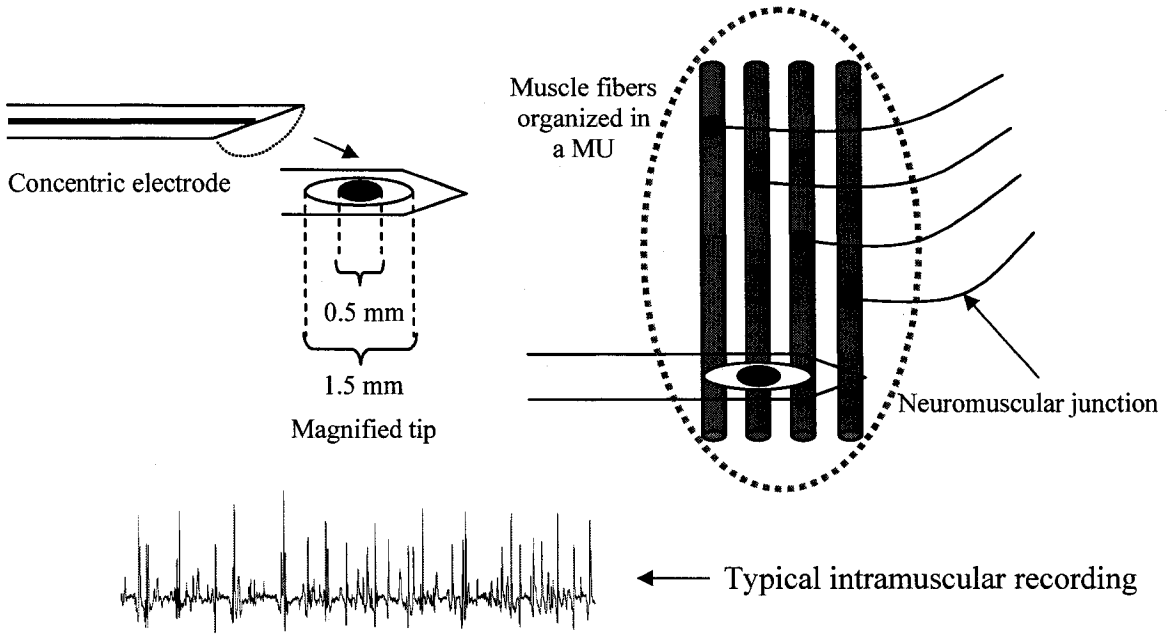

Figure 2.2: Schematics of intramuscular recording using a concentric electrode.

In this work we limit the scope to the most used approach for clinical applications, using concentric needle electrodes. Figure 2.2 shows a schematic of a concentric electrode.

The intramuscular recording is also a summation of MUAPs in both space and time similar to surface MES; in this case the muscle fibers that lie within the tip of the electrode mainly contribute to the signal. The main differences between the intramuscular and surface recordings are: 1) intramuscular recordings are more localized and have a higher spatial resolution

compared to the surface MES, 2) intramuscular recordings have a higher signal to noise ratio (SNR) because they are less influenced by the skin filtering effects (i.e., spatial filtering), and 3) the bandwidth of the intramuscular MES is also higher than surface recordings because there is less tissue between the source and recording site which reduces the tissue filtering effect.

The intramuscular MESs are used commonly for MES decomposition and clinical diagnosis of neuromuscular diseases [Stalberg and Falck, 1997]. Advances in MES decomposition and clinical diagnosis will be presented in section 2.5.3.

2.2.2. Surface recordings

The surface MES is greatly influenced by the electrode size, material, and location on the muscle. Hence, it is very important to follow a set of unified standards to guarantee repeatability and avoid misinterpretation of the results [Merletti *et al.*, 1995].

For surface MES recordings, several types of different electrodes have been introduced and studied [Farina *et al.*, 2001]. In this work we limit our scope to bi-polar configuration for two channel recording.

Two channel recordings using a bi-polar electrode configuration is the most common approach for clinical assessment of muscle. The two channels are used as inputs to a differential amplifier. The resultant MES reflects the difference in the electrode potential under the two poles of the electrode. Schematic representation of this process is shown in Figure 2.3.

The differential bi-polar recordings are a summation of MUAPs in both space and time. It is important to place the bi-polar electrode between the innervation zone and tendon so that the

recordings are consistent for one direction of propagation; however, it is difficult to identify the location of the innervation zone using one set of bi-polar electrodes.

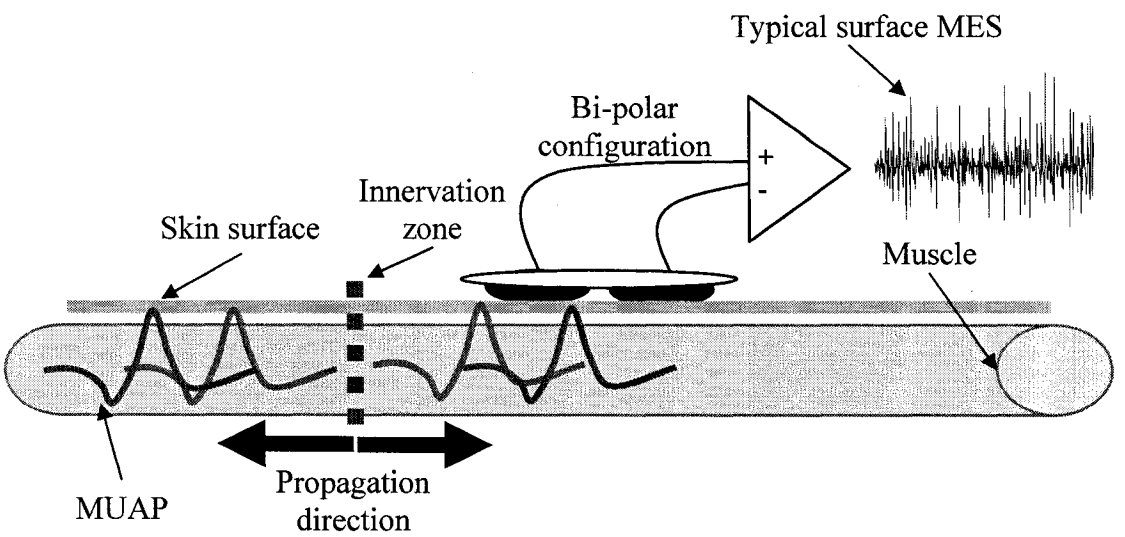

Figure 2.3: Schematics of bi-polar electrode placement and surface recording.

The limitations of the bi-polar electrode configuration in identifying the innervation zone, finding the best recording sites for a specific assessment (e.g., finding the best fatigue site), and poor spatial localization and resolution, motivate multi-channel recording and grid configurations. Several grid and array configurations have been suggested and studied for different applications [Farina, 1999]. Recently electrode grids are being widely used for different applications such as signal decomposition [Merletti *et al.*, 2008].

2.3. MES analysis

MES analysis includes signal processing techniques and mathematical procedures that can be applied to extract information from generic biological signals [Akay , 1996; Merletti and Parker, 2004; Rangayyan, 2005]. MES analysis involves study of the interference pattern that results

from the simultaneous activation of a coalition of MUs detected by surface or intramuscular electrodes. In general, the signal processing techniques applied to the surface MES provide a global description of the bioelectrical activity of the recording site and do not decompose the signal into individual MUs; thus, extracted information are not directly related to physiological phenomena. On the other hand, intramuscular MESs are commonly used for MUAP decomposition [Farina, 2001]. In the reminder of this chapter both scenarios are briefly addressed.

2.3.1. Time domain analysis

Several factors determine the suitability of a signal feature in a particular application. The computational complexity for extraction of a feature is always a major factor; time domain features serve well in terms of computational simplicity and it has been shown that they are very useful for characterization of the surface MES in several applications [Hudgins *et al.*, 1993; Merletti and Parker, 2004]. The four most used time domain features of surface MESs are: 1) mean absolute value, 2) RMS, 3) NZC or sign changes and 4) NT or slope sign changes [Finsterer, 2001].

The mean absolute value and RMS value are the simplest forms for representing the amplitude information of the signal. A high mean absolute value and/or RMS value suggest large signal amplitude and energy. These features are the primary measures for the level of force.

The NZC is the simplest measure of the signal's frequency content which could be extracted from the time domain representation. It is also possible to include a threshold to avoid zero crossings caused by noise [Hudgins *et al.*, 1993]. The NZC is primarily a measure for muscle

activation detection and discrimination between high frequency noise and myoelectric content in a MES. The sign change of the signal's derivatives, NT, has been also widely applied for discrimination between normal and pathological MESs [Merletti and Parker, 2004].

Application of time domain analysis in clinical diagnosis and myoelectric prosthetic control will be further discussed in section 2.5.

2.3.2. Power spectrum analysis

The power spectral density and power spectrum are widely used for analysis of MESs [Merletti and Parker, 2004; Proakis and Manolakis, 2006]. The MES can be considered to be wide sense stationary (WSS) in small intervals (1 to 5 s). The most common technique for estimation of MES power spectrum is Welch's method; this method involves windowing and averaging of the estimates obtained from different consecutive or partially overlapped signal epochs [Proakis and Manolakis, 2006]. Welch's method is central to the study of power spectral moments and percentile frequencies (e.g., MNF and MDN) which is well documented in muscle fatigue studies and will be further discussed in section 2.4.2.

An alternative approach to Fourier-based power spectrum estimation is based on the methods referred to as parametric or model-based (instead of non-parametric in case of Fourier-based approaches). The basis for this type of power spectrum estimation is representation of the signal as the output of a linear time invariant (LTI) filter with white noise as the input. The LTI filter is known as the generation model and the power spectrum of the signal could be easily estimated when the model is identified [Proakis and Manolakis, 2006]. Several different techniques have been proposed for parametric power spectrum estimation, among which autoregressive (AR)

modeling is well studied in the context of MESs [Merletti and Parker, 2004]. Parametric power spectrum estimation is central in MES pattern recognition widely used in different applications including prosthetic control [Englehart *et al.*, 2003] and MES augmented speech recognition [Chan *et al.*, 2006] and will be further discussed in section 2.5.

2.3.3. Coping with non-stationarity and temporal localization

Both non-parametric and parametric methods for power spectrum estimation are limited to an assumption of stationarity (time invariant statistical properties); moreover, they do not provide any time localization. Thus, special care must be taken for time varying, quasi-stationary stochastic processes such as MESs. For example, during an isometric contraction the progress of fatigue will alter the MES statistical properties; this problem is even more dramatic during dynamic contractions when several other time varying factors affect the myoelectric dynamics and the MES.

The simplest approach to resolve the difficulties associated with non-stationarity and time localization is to compute a power spectrum for short signal epochs which could be approximated as WSS; this will also increase the temporal resolution. This approach leads to short-time Fourier transform (STFT) and time-varying autoregressive (TVAR) modeling, which are common techniques for the analysis of non-stationary MESs [Merletti and Parker, 2004; Proakis and Manolakis, 2006].

2.3.4. Multi-resolution and wavelet analysis

Considering STFT and TVAR, the time-frequency resolution depends on the window length used for segmentation; a short window leads to a high resolution in time and a low resolution in

frequency and vice versa for a long window (i.e., time and frequency resolution are dependent according to the *Heisenberg* uncertainty principle). This limitation suggests using variable window lengths for analysis of different frequency ranges might be more informative (i.e., using long windows for low frequencies and short ones for high frequencies). Using a variable window length leads to multi-resolution analysis and wavelet transform, which have been also well studied for the analysis of MESs [Merletti and Parker, 2004; Englehart *et al.*, 2001]. Further discussions on the application of multi-resolution analysis and wavelet transform will be presented in section 2.5.1.

2.3.5. Noise reduction and conditioning

Similar to most biological signals, analysis of MESs is also greatly influenced by noise and interference conditions. Removing the power line 60 Hz noise has been well studied previously [Merletti and Parker, 2004]. A simple notch or comb filtering is commonly used for noise reduction; however, it is preferred to adaptively remove the noise and take special care to preserve the power spectrum as the simple notch and comb filtering greatly influences the power spectrum. Adaptive recursive least-squares filtering is an effective approach for removal of noise and preserving the power spectrum, where a floating channel is used to record the interferences in the recording environment [Talebinejad *et al.*, 2008].

2.4. Force and fatigue estimation

2.4.1. Force estimation

Force estimation is likely the most historical and seminal aspect of MES analysis. Foundations of all MES-based applications are centered on the reflection of the level of force produced by a muscle in its electrical activity and recorded MES.

As mentioned previously, force production is regulated by two main mechanisms: 1) spatial recruitment of MUs, and 2) temporal recruitment and firing rate of the already active MUs. These two mechanisms are present in different proportions and with different strategies in different muscles. In kinesiological and clinical studies estimation of force from the MES is attractive to assess the contribution of a single muscle to the total produced force. Previous studies have shown that there is a high correlation between the level of force and the surface MES amplitude [Merletti and Parker, 2004]. This correlation was found to be linear in some muscles e.g., the muscles controlling the fingers and closer to parabolic in other muscles e.g., the upper *trapezius* and *biceps* [Merletti and Parker, 2004]. Differences in the percentage of spatial and temporal recruitment have been considered as the most likely explanation for these different relations. It should be noted that it is very difficult to explain the relations between the force and surface MES amplitude directly from the neural drive; however, apparently both complex nonlinearities in the relation between the neural drive and surface MES amplitude, and neural drive and force, balance each other and result into a close to linear relationship between force and surface MES amplitude [Merletti and Parker, 2004].

Even when discussing the relations between the surface MES amplitude and force during a short isometric contraction without fatigue, a number of other factors must be taken into account. For example, surface MES amplitude is greatly influenced by the electrode location, subcutaneous fat layer thickness, the inclination of the fibers with respect to the detection system, muscle fiber

CV, MU firing synchronization and cross-talk between the muscle of interest and other nearby muscles. Thus, force estimation is very limited in terms of repeatability and inter- and intra-subject comparison. These conditions are even worse with fatigue considerations and/or during dynamic contractions, because the MES amplitude is also greatly influenced by the progress of fatigue, speed of contraction and muscle shape and length (joint angle).

It was mentioned that the force is affected by the muscle fiber CV; on the other hand some studies show that the muscle fiber CV also changes with force. Hence it is very difficult to unscramble relations between the force and muscle fiber CV [Merletti and Parker, 2004].

The MES power spectrum is also affected by force. In particular the *size principle* paradigm and orderly recruitment suggests there might be an increase in the higher frequency content of the MES caused by the firing of the larger and faster MUs; however, no consistent pattern has been identified by the researchers so far using conventional spectral moments. In some studies the MNF and MDN are increased with an increased force level [Bilodeau *et al.*, 1991], sometimes they are decreased [Bilodeau *et al.*, 1991], and also in other studies the spectral features are insensitive to force level [Arendt-Nielsen *et al.*, 1985]. These inconsistencies could be explained by the different muscles and contraction protocols used in each study [Merletti and Parker, 2004].

Recently different techniques have been proposed for improved force estimation using high density EMG (multi-channel) [Clancy *et al.*, 2000]; however, these are also limited to the previously mentioned restrictions caused by fatigue considerations and/or dynamic contractions [Merletti and Parker, 2004].

Meanwhile, MES amplitude will likely remain the most important indicator of muscle activation and force in the near future, simply because there are no substitutes at this time nearly as useful as MES amplitude (we will introduce a complementary force index in chapter 5).

Figure 2.4 shows sample MESs recorded during an isometric contraction of the *biceps* with three different force levels (the electrode location is the same in all cases). It is clearly noticeable that the amplitude of the signals is increased as the force level is increased. The RMS values could be easily used in this case to discriminate between the force levels.

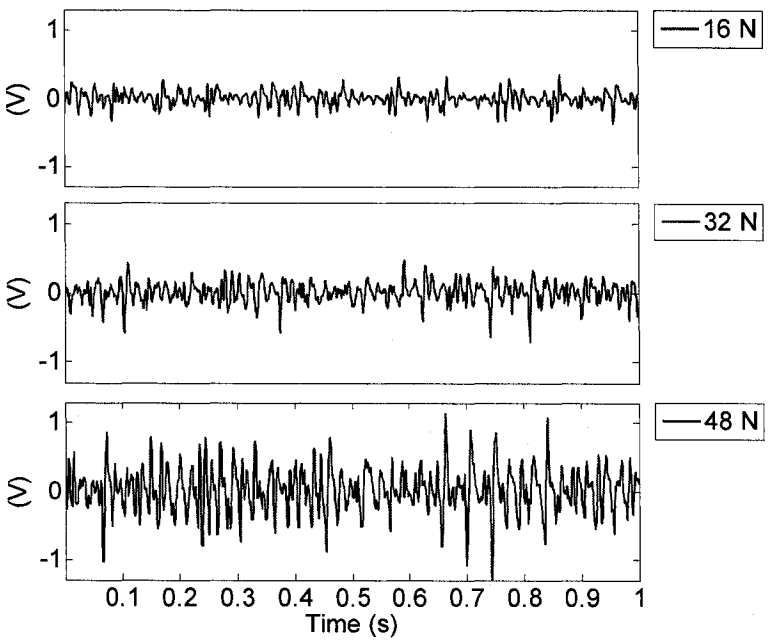

Figure 2.4: Sample MESs recorded during isometric constant force contractions with three different force levels, 16, 32, and 48 N with RMS values 0.052, 0.183, and 0.343 respectively.

2.4.2. Fatigue estimation

Fatigue was previously introduced in section 2.1.3 as an experience of our daily life, with a very complex definition. Fatigue estimation is one of the most challenging tasks for researchers in this

area. Accurate and reproducible fatigue estimation using surface MES is of interest for a wide variety of applications, including sport performance and clinical studies.

Previous studies have shown that the MES changes characteristically with fatigue and it is possible to assess the progress of fatigue using myoelectric parameters. During isometric constant force contractions, muscle conduction velocity decreases with fatigue and this phenomenon is reflected in a decrease of the MDN of the MES [De Luca, 1984]. Consequently, tracking the MDN has been well-established as the gold standard for muscle fatigue assessment with MES under static conditions [Merletti and Parker, 2004]. During dynamic contractions however, when muscle length (joint angle) and/or force vary, MDN measurements are also influenced by factors other than muscle fatigue; the depth of active and detectable MUs for example, has been shown to significantly influence the MES frequency content, and MDN, through spatial filtering [Merletti and Parker; 2004]. Moreover, muscle innervation zone changes and/or end-effects also contribute to confounded frequency content. Thus, conventional frequency parameters are confounded during dynamic contractions [Merletti and Parker, 2004; Bonato, 2001; Karlsson *et al.*, 2000; MacIsaac *et al.*, 2001a,b].

Different methods have been proposed which show improvement for fatigue estimation when compared to the conventional MDN during dynamic contractions. Bonato *et al.* [2000] developed a new time-frequency approach to track fatigue named the instantaneous mean frequency. MacIsaac *et al.* [2001] proposed a processing strategy based on short time Fourier transform to track fatigue with the mean frequency. Farina *et al.* [2004] proposed an approach to track fatigue based on the changes of conduction velocity. Recently, MacIsaac *et al.* [2006] proposed a multi-variable approach to extract a fatigue index from multiple myoelectric

parameters which also shows improvement over mean frequency and instantaneous mean frequency. The multi-variable approach outperforms single fatigue indices by exploiting more than one confounded fatigue measure. It is desirable to find more reliable parameters to assess the myoelectric manifestation of fatigue, which is the objective of this work. Such parameters could also be used as inputs to the multi-variable approach and would be expected to further improve its performance and reliability.

These new techniques show improvement compared to conventional MNF/MDN approaches [MacIsaac *et al.*, 2001a,b], however, accurate fatigue estimation especially during dynamic contractions is still far from ideal, but current techniques and in particular MNF/MDN approaches will remain as the main fatigue indices in the near future (we will introduce complementary fatigue indices in chapters 6 and 8).

We conclude the discussion on fatigue estimation in this section with a typical example of fatigue estimation during an isometric voluntary constant force contraction of the *biceps brachii* until complete exhaustion. The descriptions of the data used in this example can be found in chapter 4. Figure 2.5 shows the power spectra of MESs recorded from the first 5 s and the last 5 s of the contraction. The power spectrum is estimated using the Welch's method with 0.5 s windowing and 50 % overlap between the consecutive windows. The power spectrum of the last 5 s (MDN = 57.34 Hz), clearly shows a shift towards lower frequencies and a higher energy (RMS = 0.54) compared to the power spectrum of the first 5 s (MDN = 70.67, RMS = 0.31). It is important to note that the contraction is constant force; however the energy of the signal and the RMS is increased which is most likely caused by the increased averaged firing rate of the MUs due to the muscle fatigue. This also demonstrates the confounded effects of force and fatigue on

the RMS of the signal which will be further discussed in chapters 5, 6 and 8. Overall, the MDN provides a fair index for the muscle fatigue in this simple contraction protocol.

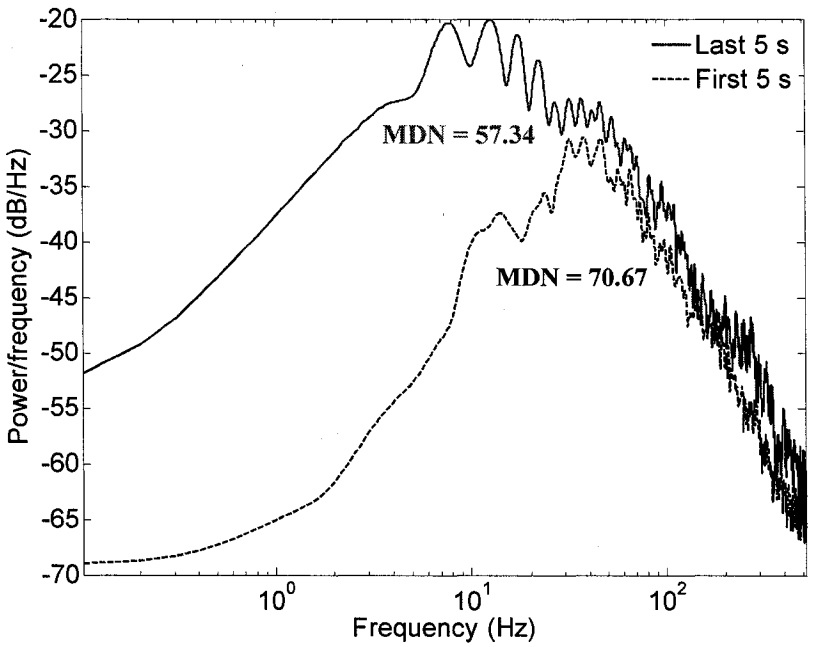

Figure 2.5: Shift of spectral content of MES towards lower frequencies due to muscle fatigue.

2.5. Applications

2.5.1. MES prosthetic control

The surface MES has been widely researched for control of powered prostheses [Merletti and Parker, 2004; Englehart *et al.*, 1999; Parker and Scott, 1985]. This control approach, referred to as myoelectric control, has found widespread use for individuals with amputations or congenitally deficient upper limbs. Figure 2.6, shows block diagram schematics of the essential elements of a normal and myoelectric control system.

The concept of myoelectric control was introduced in 1940s, however significant progress in myoelectric control development was achieved in 1960s when the first commercial system controlling a powered hand was produced in the USSR [Kato *et al.*, 1965]. Pattern recognition-based myoelectric control was first carried out in 1968 [Merletti and Parker, 2004], and since then myoelectric control has made a great impact in clinical applications.

Almost every possible combination of different MES features (including time domain features, AR, LP, and wavelet coefficients) and different classification schemes (including linear and polynomial classifiers, artificial neural networks, self-organizing maps, genetic algorithms, and hidden Markov models) have been well studied and documented [Englehart *et al.*, 1999, 2001, 2003; Hudgins *et al.*, 1993; Chan and Green, 2007].

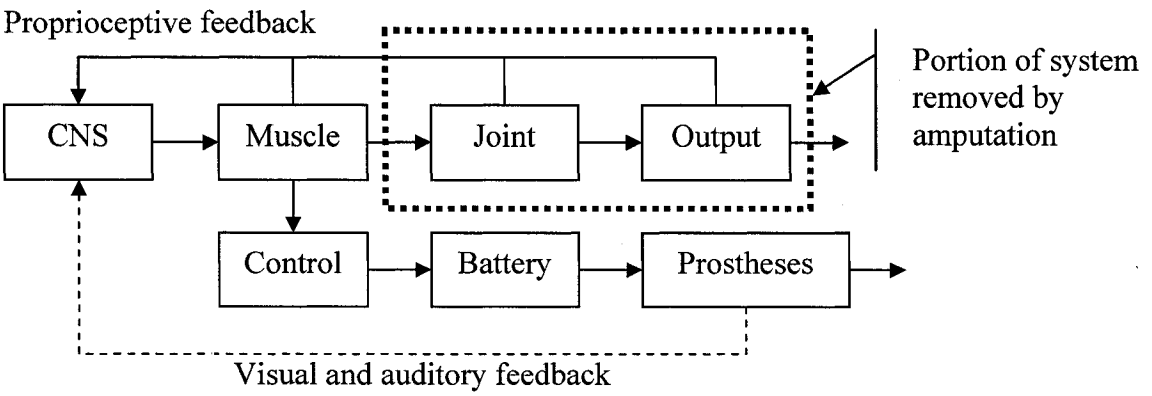

Figure 2.6: Block diagram schematics of normal and myoelectric control systems. Based on [Merletti and Parker, 2004].

Despite the wide variety of studies in this area, simple LP coefficients along with linear classification is the most used approach for myoelectric control at this time and likely will remain as the most used approach in near future because its accuracy is very close to other more complicated approaches [Chan and Green, 2007].

2.5.2. MES augmented speech recognition

Central to MES augmented speech recognition is the presence of speech information in facial muscles; that is, facial muscles show unique characteristics when different words (combination of different phonemes) are uttered. These unique characteristics could be exploited with a pattern recognition scheme for speech recognition. MES augmented speech recognition (combination of MES and acoustic speech) shows improved classification accuracy and performance in environments with acoustically noisy conditions [Chan *et al.*, 2006], because the MES is not affected by the acoustic noise.

Previous studies are mostly based on whole word level speech recognition [Chan *et al.*, 2006], but recently this concept has been extended to phoneme-based speech recognition as well [Scheme *et al.*, 2007]. This area is very new and there are still major developments on the way.

2.5.3. MES decomposition and clinical diagnosis

It has been previously established that MUs are the basic building units of the neuromuscular system. Studying MU recruitment, and firing rate modulation can lead to an understanding of motor control and pathological alterations of the neuromuscular system [Zwarts *et al.*, 2000].

Conventionally, for clinical applications the MES is examined by visual inspection and/or listening to the signal through a loudspeaker and pathological conditions are readily detectable in severe cases. In neuropathic disorders, the excited motor neurons are reduced in number and

muscle fibers give larger MUs, which generate MUAPs of higher amplitude and longer duration than normal. This reflects as a weaker sound from the loudspeaker [Okajima *et al.*, 2000]. In myopathic disorders, due to loss of individual muscle fibers, MUAPs are low in amplitude and short in duration. This reflects as a loud sound from the loudspeaker [Merletti and Parker, 2004]. These frequency changes of the MES in neuromuscular disease conditions led to frequency domain analysis for diagnostic purposes; however, in practice it is easier and more efficient to exploit the time domain characteristics of MES for discrimination between normal, neuropathic and myopathic conditions. Traditionally, NT and mean amplitude has been the most commonly used MES features for clinical examinations and have been also used in commercial EMG systems [Abel *et al.*, 2006]. The ratio NT/mean amplitude has been found to decrease in cases of neuropathy and increase in myopathies [Arabadzhiev *et al.*, 2008]. Recently, several signal processing techniques have been proposed to improve the traditional turn analysis [Englehart *et al.*, 1999; Arikidis *et al.*, 2002; Abel *et al.*, 2006]. However, manifestation of neuromuscular disorders in MES are often subtle, particularly in the early stages of a disease or in less severe cases, which makes applications of signal processing techniques for automatic diagnosis very limited in practice. Furthermore, the MES is non-stationary and transient which also limits the applicability of many signal processing techniques; this has led to a great interest in time-frequency approaches [Arikidis *et al.*, 2002; Englehart *et al.*, 2001; Christodoulou and Pattichis , 1999].

MES decomposition is the process of identification and classification of individual MUAPs in the MES interference pattern. It is possible to use surface or intramuscular MES for this task. Traditionally intramuscular MES is the primary basis for MUAP decomposition because it is

very difficult or almost impossible to identify individual MUs in the surface recordings; however, recently surface MES decomposition has been improved using multi-channel high density recordings [Merletti *et al.*, 2008].

Conventionally unsupervised clustering is the main approach for MUAP identification. The classification accuracy then could be improved with further supervised classification of MUAPs.

Emerging techniques for MES decomposition include, wavelet transform, higher order statistics, and Bayesian learning approaches [Hamilton-Wright and Stashuk, 2005].

Decomposition for clinical purposes including discrimination between normal, myopathy, and neuropathic MES has been well studied previously [Stalberg and Falck, 1997]. It is also interesting to discriminate between different types of neuromuscular disorders directly from the raw MES to avoid complex decomposition procedures; this aspect will be further discussed in chapter 7.

2.6. Summary

Electromyography and analysis of MESs are well established areas of research and a comprehensive introduction is out of the scope of this work. In this chapter, we provided a brief overview of this area with special stress on the points that will be further discussed in this work.

As it was shown, signal processing techniques and approaches used for analysis of MESs are well advanced and established and are mainly based on the assumption that the origins of MESs are inherently stochastic and random; however, there exist great difficulties and limitations for estimation of force and fatigue. Moreover, the foundations of the current state of the art in MES analysis for other applications such as myoelectric control, MES augmented speech recognition,

and clinical diagnosis are still confounded when muscles are moving and/or fatigued; that is, the accuracy of classification schemes in prosthetic control, and MES decomposition will dramatically decrease with movement and fatigue. Thus improved force and fatigue estimation will ultimately elevate state of the art in most MES applications.

On the other hand, given the neuromuscular structure and origins of MESs it seems simplistic to assume that the MESs are purely random; there is strong evidence of highly non-linear deterministic and chaotic dynamics in the neuromuscular system (e.g., structured nature of the MUs). The architecture of the neuromuscular system suggests great potentials to exploit the multi-scale characteristics of the MESs which is not widely studied.

In the reminder of this work we will focus on multi-scale aspects of myoelectric dynamics and MESs.

Chapter 3

3. Multi-scale phenomena and multi-scale analysis of MESs

3.1. Multi-scale phenomena

Analysis of a complex phenomenon regulated by several factors is influenced greatly by the scales in which the phenomenon is analyzed. Such a phenomenon, also known as a multi-scale phenomenon is usually seen in complex interconnected systems which exhibit both highly non-linear deterministic as well as random characteristics [Barenblatt, 2003].

The neuromuscular system also resembles a complex interconnected system (i.e., the central and peripheral nervous system and muscle), and its electrical activity is also generated from both structured (e.g., muscle fiber geometry and MUAP shape) and random (e.g., innervation process) origins. The complexity and the large number of factors affecting the MES (i.e., tens to hundreds of MUs) suggest multi-scale analysis would be well-suited for the analysis of MESs; a similar argument could be applied to other biological signals (e.g., the electroencephalogram) [Bassingthwaighte, 1994].

As mentioned in chapter 2, one way to analyze the MES is to employ conventional techniques (e.g., RMS, MDN, and AR coefficients). One can attempt to extend the analysis to different scales by simply repeating the analysis in all possible scales (e.g., by scaling the time axis). An alternative way is to develop measures that explicitly incorporate the concept of scale and characterize the MES with scale-dependent information; such measures could effectively complement conventional signal processing approaches.

In the reminder of this chapter we will show how it is possible to accomplish this goal based on chaos and random fractal theory. Four major paradigms for multi-scale analysis of a time series will be presented and discussed in the context of MESs. These four paradigms are: 1) *self-similarity*, 2) *long memory*, 3) *multi-fractality*, and 4) *chaos*. Figure 3.1, illustrates these four paradigms.

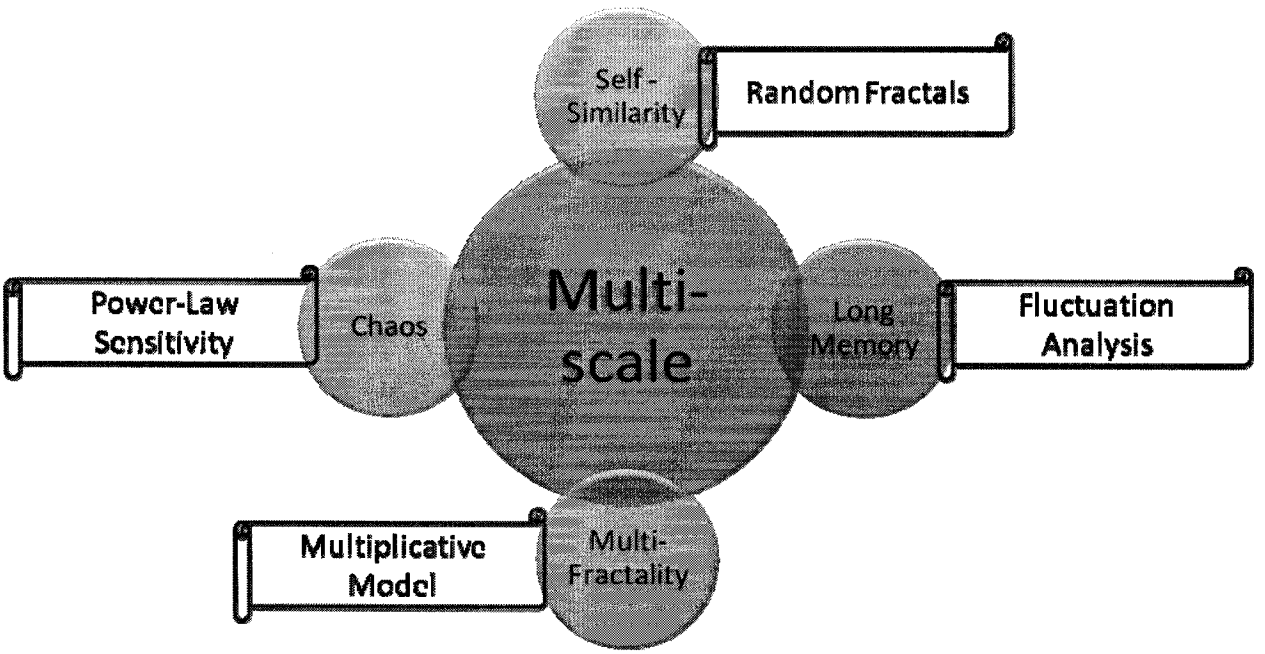

Figure 3.1: Diagram of material covered in chapter 3.

First, the concept of *self-similarity* which is at the center of fractal geometry, and $1/f$ processes will be presented. We will show that the classic $1/f$ approach is not directly applicable to MESs.

Second, we discuss the concept of dominant complexity and *long memory* in the context of MESs and expand multi-scale analysis to structure-function-based approach and DFA for quantification of long memory.

Third, we introduce the concept of *multi-fractality* and the MCMs and present a practical approach for MCM modeling.

Fourth, we present a *chaos* framework for time series analysis. We show that the MESs exhibit power-law sensitivity to initial condition. We show MESs are not fully random or chaotic, but they resemble random fractals and chaotic motions on different time scales.

3.2. Fractal geometry

Euclidean geometry is about regular shapes such as, lines, squares, circles and spheres. But most natural elevations and surfaces such as, mountains, clouds, and coast lines do not follow a simple regular form, and Euclidean geometry might not be sufficient to characterize them accurately. This limitation of Euclidean geometry motivated Mandelbrot to create a new branch of science, the fractal geometry [Mandelbrot, 1968, 1974, 1982, 1997].

The intuitive definition of a fractal is a set that shows irregular but self-similar features on many or all scales. Self-similarity means that part of an object is similar to other parts or to the whole object (e.g., Koch's snowflake [Mandelbrot, 1982]). Fractal geometry provides an elegant framework for the study of many natural phenomena which show exact or statistical self similarity.

A train of single muscle fiber action potentials originating from a distinct muscle fiber show self-similarity because they have a distinct originating source. It is possible to mathematically demonstrate that superposition of a number of distinct self-similar processes is also self-similar [Gao, 2000]. Thus, the MES is expected to exhibit characteristics of self-similarity.

Mathematically, a fractal is characterized by a power-law relation. In the reminder of this chapter the concept of power-law behaviour is discussed and is extended to MESs.

3.2.1. Morphological power-law behaviour

Imagine, we are tiny people walking on a jagged route similar to a MES. The number of steps we need to take is a function of our step size. Hence the length of the route could be approximated as

$$L = N(\varepsilon)\cdot\varepsilon, \varepsilon \to 0, \qquad (3.1)$$

where L is the approximated length, $N(\varepsilon)$ is the number of steps and ε is the step size. If $N(\varepsilon)$ and ε are related to each other with a power-law relation in this form

$$N(\varepsilon) \sim \varepsilon^{-D}, \varepsilon \to 0, \qquad (3.2)$$

where D is known as the topological dimension, or morphological dimension. Note, in Eq.(3.2), $\sim$ denotes a functional equivalency between the number of steps and the step size. When D is an integer the route is a regular surface which could be characterized by the Euclidean geometry. For example consider a line, $N(\varepsilon)$ and ε are directly related in this case and we can conclude that $D = 1$; that is why a line is known to be 1 dimensional. For an isolated point $N(\varepsilon)$ is always 0, which leads to a $D = 0$, which is why an isolated point is 0 dimensional. However, for most natural phenomena D is not an integer and is fractional. For a time series, when D is fractional, it is in the range $1 < D < 2$, and emphasizes a fragmented, and irregular geometry. When D is fractional it is also known as a fractal dimension.

The relationships between the number of steps and the step size of tiny people walking on a jagged route is the simplest form of power-law behaviour; this is the basis for several signal

processing techniques for computing the fractal dimension of a signal (time series, image or volumes). For example, the two most common methods for the analysis of fractal characteristic of MESs are the box-counting method [Turner *et al.*, 1998] and the Katz method [Katz, 1989], which are directly based on the above definition of fractal dimension [Anmuth *et al.*, 1994; Gitter *et al.*, 1995; Gupta *et al.*, 1997; Mesin *et al.*, 2008; Shields *et al.*, 2006; Xu and Xiao, 1997].

Despite widespread applications of these morphological methods for the analysis of MESs, we have previously shown that they associate serious limitations and difficulties [Talebinejad *et al.*, 2006b, 2007, 2008e]. For example, the estimated fractal dimension (eFD) using the morphological methods and in particular Katz's method is highly correlated with the amplitude of the signal; thus, the eFD simply follows the amplitude and does not provide any information beyond that. This correlation was noted in [Anmuth *et al.*, 1994; Gitter *et al.*, 1995; Shields *et al.*, 2006] but the authors failed to recognize the dominant effect of amplitude. Indeed we have shown that constant amplitude scaling, which should not affect the eFD, is correlated with the eFD computed by Katz's method [Katz, 1989]. The box-counting method, results in saturated fractal dimensions 0.5 above topological dimension for sampled signals; that is, for sampled time series the eFD with saturate around 1.5. This saturation could be explained by the finite precision of the sampled signals. For example, saturation of eFD, using the box-counting method, is seen in [Xu and Xiao, 1997]. In this work, the authors explain that the saturation in eFD is caused by the saturation of the recruitment of a number of MUs and their firing rate; however, it is more likely caused by the estimation method itself. These limitations could be explained by the finite

precision and resolution of sampled data; thus, ε is bounded and cannot approach zero [Talebinejad *et al.*, 2008e].

Overall, for sampled data and in particular for random processes, morphological methods associate serious difficulties and shortcomings. This motivates methods that exploit the statistical characteristics of a signal to analyze the fractal characteristics.

But before proceeding any further let us ask this question: how does morphological power-law behaviour helps us with multi-scale analysis? Well, according to Eq.(3.2) the fractal dimension could be used to characterize a signal on a wide range of scales were the scale is ε. We shall discuss this further shortly.

In the reminder of this chapter we will extend the simple morphological power-law relation to statistical properties and beyond.

3.2.2. Self-similarity and probabilistic power-law behaviour

It was mentioned previously that central to fractal geometry is the concept of self-similarity. To introduce a rigorous mathematical definition for self-similarity imagine we are looking for self-similarity in a deterministic time series (e.g., Weiestrass time series [Turner *et al.*, 1998]). Intuitively, we have to magnify the signal or zoom into it and look for similar patterns. For a time series magnifying is equal to scaling the time axis with a scale λ, where $0 < \lambda < 1$. If after magnifying, the time series keeps its functional form, we can conclude that the time series shows self-similarity. Mathematically, this could be translated to a relation in this form

$$X(t) = \lambda^{-H} X(\lambda t), \qquad (3.3)$$

where the $X(t)$ is the time series, $X(\lambda t)$ is the magnified version of the time series and H is the self-similarity exponent also known as the Hurst exponent, which is a fractional-order. In this case, after magnifying the time series the functional form of samples is preserved (i.e., self-similarity) and it is only scaled, exhibiting a power-law relation to the magnification factor λ. The scaling is regulated by the self-similarity exponent, which is related to the fractal dimension of the time series through a linear transformation. A deterministic time series satisfying Eq.(3.3) is known as a deterministic mono-fractal, which shows deterministic self-similarity (also known as self-affinity). This concept could be extended to random processes (e.g., FBM [Turner *et al.*, 1998]); that is, instead of exact self-similarity we might observe statistical self-similarity in this form

$$\Pr[X(t)] = \lambda^{-H} \Pr[X(\lambda t)], \qquad (3.4)$$

where the $\Pr[X(t)]$ is the probability distribution of the time series, $\Pr[X(\lambda t)]$ is the probability distribution of the magnified version of the time series and H is the self-similarity exponent also known as the Hurst exponent, which is a fractional-order (Appendix A, shows derivation of Eq.(3.4) for FBM). In this case, after magnifying the time series the functional form of distribution of samples is preserved (i.e., probabilistic or statistical self-similarity) and it is only scaled and shows a power-law relation to the magnification factor λ. The scaling is regulated by the self-similarity exponent, which is related to the fractal dimension of the time series through a linear transformation. A random time series satisfying Eq.(3.4) is known as a random mono-fractal, which shows probabilistic or statistical self-similarity (also known as a random scaling fractal).

Most remarkably, a statistical mono-fractal shows self-similarity in all aspects of its statistical properties. For example, it could be mathematically demonstrated that the mean, variance, autocorrelation and power spectrum of a mono-fractal time series also show self-similarity in this form

$$E[X(t)] = \lambda^{-H} E[X(\lambda t)], \qquad (3.5)$$

where $E[X(t)]$ denotes the expected value (mean) of the time series $X(t)$,

$$Var[X(t)] = \lambda^{-2H} Var[X(\lambda t)], \qquad (3.6)$$

where $Var[X(t)]$ denotes the variance of the time series $X(t)$,

$$R_X[X(t)] = \lambda^{-2H} R_X[X(\lambda t)], \qquad (3.7)$$

where $R_X[X(t)]$ denotes the autocorrelation of the time series $X(t)$,

$$S(f) = \lambda^{-2H-1} S(f/\lambda), \qquad (3.8)$$

where $S(f)$ denotes the power spectral density of the time series $X(t)$.

Statistical mono-fractals are the most intensively studied form of fractals. They have found numerous applications in many areas of science and engineering. In signal processing, the most common approach for characterizing fractal characteristics of a signal is based on the power spectrum analysis and solution of Eq.(3.8) which is in this form

$$S(f) = 1/f^{2H+1}, \qquad (3.9)$$

which shows that the power spectrum of a statistical mono-fractal shows a power-law relation with frequency regulated by the Hurst exponent. The processes that show a power spectrum in form of the Eq.(3.9) are known as $1/f$ processes and analysis of a power spectrum using Eq.(3.9) is known as the $1/f$ approach. Central to $1/f$ processes is the assumption that the process is inherently random. Thus, the underlying system responsible for it has infinite degrees of freedom and state variables. Such a system could be presented in the form of a fractional-order differential equation with a single fractional-order. This concept is further discussed in section 3.6 along with chaos theory.

The $1/f$ approaches have been widely studied [Chang *et al.*, 2004, 2007]. These $1/f$ approaches include modeling the MES power spectrum with Eq.(3.9), and/or modeling the MES as a $1/f$ process and then applying Eq.(3.9) to the power spectrum of the model. Central to these approaches is an optimization procedure to fit a single line to the $1/f$ power spectrum; for example, using a least squares procedure.

However, as discussed in chapter 2, the MES power spectrum does not show $1/f$ characteristics; the $1/f$ processes are mono-phase in terms of slope (i.e., linear) in a bi-logarithmic plot, but the MES does not exhibit a linear log-log power spectrum [Talebinejad *et al.*, 2008e]. Thus, approximating the MES power spectrum as a $1/f$ power-law is ill-defined. Figure 3.2, shows a typical MES power spectrum and a typical FBM power spectrum in a bi-logarithmic plot.

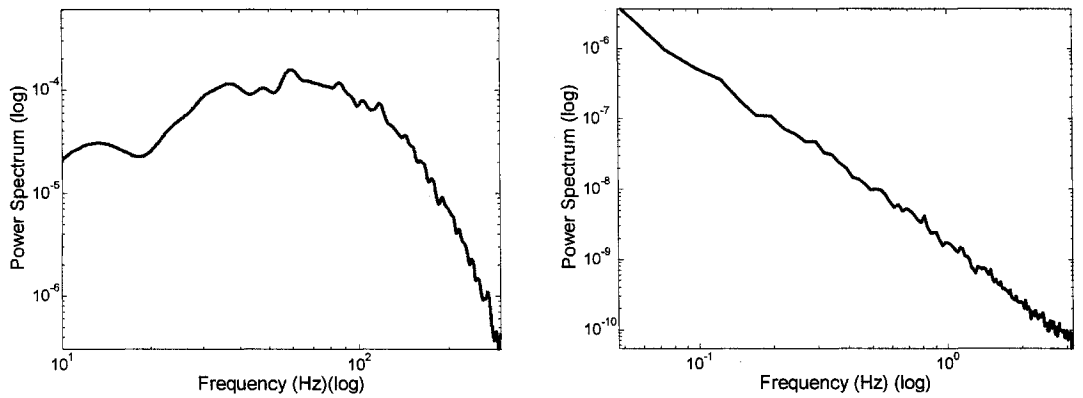

Figure 3.2: Bi-logarithmic plot of (a) typical MES and (b) typical FBM power spectrum.

Raveir *et al.* [2005], proposed a piecewise $1/f$ approach to approximate the MES power spectrum as two $1/f$ processes as shown in Figure 3.3. In this approach the power spectrum is divided into two partitions: one high frequency partition and one low frequency. Each partition is approximated with a $1/f$ power-law; the slope of each power-law is then held as a fractal indicator for each partition. The power spectrum modeling involves two separate optimizations to fit a line onto the high and low frequency partitions.

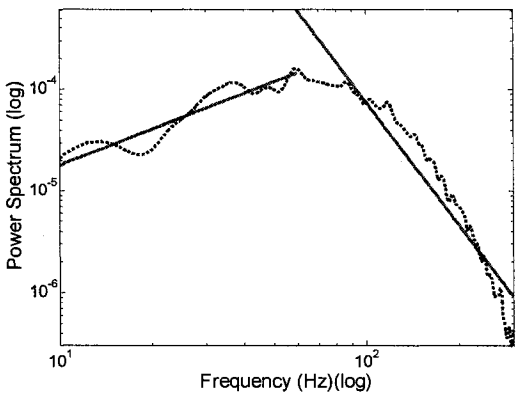

Figure 3.3: Piecewise $1/f$ approach for approximating the MES power spectrum.

The piecewise $1/f$ routine has demonstrated potential and is a systematic research tool for power spectrum-based fractal analysis that acknowledges the known bi-phase nature of the MES power

spectrum; however, there are some issues in the methodology. First, the power spectrum is partitioned into high and low frequency regions according to the peak frequency. This criterion is not necessarily optimal for partitioning the power spectrum nor mathematically justified to present a statistically self-similar behaviour. Second, high and low frequency indicators are computed separately; how they relate to each other is unclear. In particular, using the $1/f$ routine for positive slopes is not mathematically validated to represent a strict self-similar power spectrum (see Eq.(3.9)). Third, approximating the curve of the MES power spectrum with two lines as it is done in [Raveir *et al.*, 2005] is not representative of the true power spectrum (high modeling error).

But before proceeding any further let us repeat this question again: how does $1/f$ power-law behaviour and statistical self-similarity help us with multi-scale analysis? Well, according to Eq.(3.4)-(3.9) the Hurst exponent could be used to characterize a signal on a wide range of scales were the scale is λ.

In Chapter 5, we present a novel approach inspired by the piece wise $1/f$ approach with which these limitations and shortcomings are resolved.

3.2.3. Notion of dominant complexity

Let us recall the analogy of tiny people walking on a jagged route represented by the MES. We have explained that the irregular, and fragmented surface of the route could be represented by a power-law, whether it is morphological, statistical and mono-phase or bi-phase and similar to extended self-similarity seen in the MESs. Representing the jagged route by a single power-law implies the tiny people had more or less the same difficulties throughout the entire route. They are happy if we assess their frustrations for walking down a bumpy road with a single number as

the complexity of their route. This implies a single level, whether it is represented by a fractal dimension, a Hurst exponent, or two fractional-orders, is sufficient to represent the dominant complexity of the route. But what if the tiny people had a much more difficult route at some parts of their way, and they believe averaging out their frustrations is not representative? In this case, a single level of complexity is not sufficient to assess their frustrations.

Now back to signal processing. A signal which could be represented by a single power-law is known as a mono-fractal. It is appropriate to characterize such a signal according to its power spectrum. The error associated with the power spectrum modeling in the case of $1/f$ processes and bi-phase power-law could also be used to quantify the degree of fractality. Of course, modeling the power spectrum with a power-law must be accurate enough to conclude the signal is showing mono-fractality and that the computed fractional-order(s) are well representative of the actual signal. Since single level complexity may not be sufficient, this has led to the concept of multi-fractals.

In the reminder of this chapter we investigate other aspects of multi-scale phenomena and look for solutions to resolve shortcomings of single power-laws and dominant complexity.

3.3. Long memory and structure-function-based multi-fractal analysis

Previously, the $1/f$ processes and the Hurst exponent were introduced. The fractal dimension and the Hurst exponent could be also interpreted in terms of *persistence* of a process. For a time series the Hurst exponent H ranges between 0 and 1. When $0 < H < 1/2$, the $1/f$ process is said to have an anti-persistent correlation, which means it has a high fractal dimension and is very random (e.g., white noise). Similarly, when $1/2 < H < 1$, the $1/f$ process is said to have a

persistent correlation, which means it has a low fractal dimension and is very structured (e.g., coloured noise). In the same line, a persistent $1/f$ process is said to have long-range-dependency or long memory which is a result of being structured and having a low level of randomness; in other words, a process with long memory is more predictable compared to an anti-persistent highly random process. For example a line with a dimension of 1 is very persistent and highly predictable, but white Gaussian noise with a fractal dimension close to 2 is anti-persistent with a high randomness.

A popular approach for assessment of long-rang-dependency and long memory of a time series is the structure-function-based analysis [Gao *et al.*, 2007]. In this approach, first a random walk $\{y(k), k = 1, 2, \ldots, N\}$ is constructed from a zero mean time series $\{X(t), t = 1, 2, \ldots, N\}$ as

$$y(k) = \sum_{t=1}^{k} X(t), \qquad (3.17)$$

After the random walk is constructed a structure-function is defined in this form

$$Z^q(m) = \left\langle \left| y(k+m) - y(k) \right|^q \right\rangle \sim m^{\zeta(q)}, \qquad (3.18)$$

where $< >$ denotes averaging over all possible pairs of $(y(k+m),y(k))$, varying k. We then examine whether a power-law relation exist between the Z and m for some real value of q, which is a moment-order. If a power-law regime exists, the time series shows fractality. Negative and positive q values emphasize small and large absolute increments of $y(k)$, respectively. Thus, the approach allows focusing on different aspects of the random walk. Moreover, if the Hurst exponent, $H(q)$ defined as

$$H(q)=\zeta(q)/q\,, \qquad (3.19)$$

is a constant function of q, the time series is said to be mono-fractal with a single level of complexity; otherwise, the time series is a multi-fractal. How well the power-law relation of Eq.(3.18) is approximated by a single line in a bi-logarithmic plot also gives a measure of the degree of fractality. It is possible to show that the fractal dimension of a time series could be also computed based on the $H(q)$, where $H(q)$ quantifies the randomness of the underlying renewal process responsible for a time series.

To better appreciate this approach let us return to our analogy. We ask the tiny people to keep a record of their route (random walk construction). Then compare different parts of the route with each other. If the differences are negligible we conclude that their route was a mono-fractal; otherwise a single complexity measure was not enough to assess the route and the road was multi-fractal. If a time series is multi-fractal, there are potentially infinite ways to quantify its complexity (i.e., fractal dimension) with different values of q, and a single fractal dimension is not enough for representation of the time series.

Linear or other trends often exist in experimental data which might deteriorate the fractality of a signal [Peng *et al.*, 1995]. Thus, it is recommended to perform de-trending before the application of structure-function-based analysis. A simple approach for de-trending a time series is to divide the random walk into a number of partitions, approximate each partition with a linear regression, and then apply the structure-function-based analysis to the differentiated time series from the approximated lines in each partition [Peng *et al.*, 1994].

Another popular approach for detrended structure-function-based analysis is known as multi-fractal DFA [Chen *et al.*, 2002, 2005]. In this approach, after the random walk is constructed, it is divided into $\lfloor N/m \rfloor$ non-overlapping segments ($\lfloor \cdot \rfloor$ is the floor operator which rounds down to the nearest integer). Each segment is then approximated using a linear regression, which is known as the local trend. Finally, a detrended random walk, which is the difference between the original random walk and the local trend, is computed [Hu *et al.*, 2001]. The detrended random walk is denoted as $\{y_d(k), k = 1, 2, \ldots, N\}$. One examines an ensemble average in this form

$$Z^q(m) = \left\langle \sum_{k=1}^{m} |y_d(k)|^q \right\rangle \sim m^{\zeta(q)}, \qquad (3.20)$$

where $< >$ denotes averaging over all possible segments, varying k, and then examines whether a power-law relation exist between the $Z(m)$ and m for some real value of q, which is a moment-order.

In Chapter 6, we will discuss DFA in the context of MES and introduce a new approach for fatigue estimation.

3.4. Multi-fractality and multiplicative model

Another interesting aspect of random fractal theory is the MCM. MCM has been studied previously for modeling internet traffic [Gao, 2000; Gao *et al.*, 2007; Zheng *et al.*, 2005]] and neural activity [Zheng *et al.*, 2005]. Central to MCM is the concept of multiplicative multi-fractality [Oswiecimka *et al.*, 2005].

Consider a unit interval, associated with a unit mass, which can be partitioned into a series of small intervals with length ε. Let w_i be the weight associated with the ith interval. The sum of the weights, subjected to a moment order, is expressed as

$$M_q(\varepsilon) = \sum_i w_i^q , \qquad (3.21)$$

where q is a real moment-order; positive values of q emphasize the large weights and negative values of q emphasize the small weights. If there exists a power-law regime between the moments and the length of intervals in this form

$$M_q(\varepsilon) \sim \varepsilon^{\tau(q)}, \varepsilon \to 0 , \qquad (3.22)$$

for real valued q and $\tau(q)$, the weights show fractality [Gao *et al.*, 2007]. For a better characterization, $\tau(q)$ is normalized in this form

$$D_q = \tau(q)/(q-1), \qquad (3.23)$$

where D_q is known as the generalized dimension spectrum. If D_q is a constant function of q, the weights are mono-fractal; otherwise, they are multi-fractal [Gao *et al.*, 2007]. In practice, the length of intervals ε may have a finite precision (e.g., sampled signals), and the above definition of a single-stage MCM is not directly applicable.

As an alternative to single-stage MCM, a multi-stage MCM could be adopted, which is more appealing when working with sampled time series. At stage 1, a unit interval associated with a unit mass, could be partitioned into two fractions, r and 1 - r and assigned to the left and right segments, respectively. In general, the parameter r (multiplier) is a random variable regulated by

a probability distribution function. Each of the new segments could be further partitioned into two fractions following the same rule applied to the unit mass (i.e., dyadic partitions) at each stage up to stage N. At stage N, the model reaches the smallest resolvable scale (i.e., finite precision). This procedure is illustrated schematically in Figure 3.4. The multiplier r, is written as r_{ij}, with i indicating the stage number, and j indicating the position of a weight within a stage. Note that the scale or precision associated with stage i is 2^i.

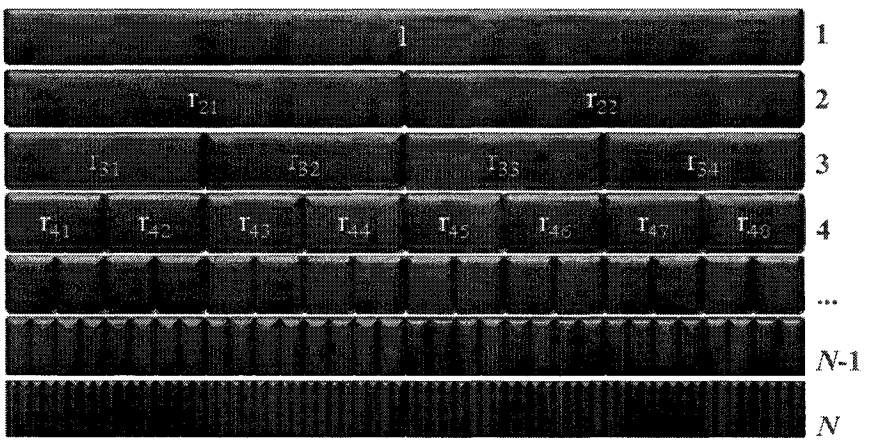

Figure 3.4: Schematic illustrating the construction of a MCM with N stages.

When we have access to a time series, constructing a MCM model can be carried out in the reverse direction; that is, starting at stage N, and by dyadic combination of all samples [Gao *et al.*, 2007]. This procedure is illustrated schematically in Figure 3.5 for a signal $\{X(t)\}$ with 8 samples, which are normalized to have a sum of one. The weights are simply added in a dyadic format. Note that after construction of this model by summation, it is possible to represent it in the form of a multiplicative model similar to Figure 1, by starting at stage 1 and computing the multipliers r_{ij} at each stage (e.g., $r_{21} = [X(1)+X(2)+X(3)+X(4)]$ and $r_{22} = 1-r_{21}$). Thus, Figures 3.4 and 3.5 are inter-changeable when $N = 4$.

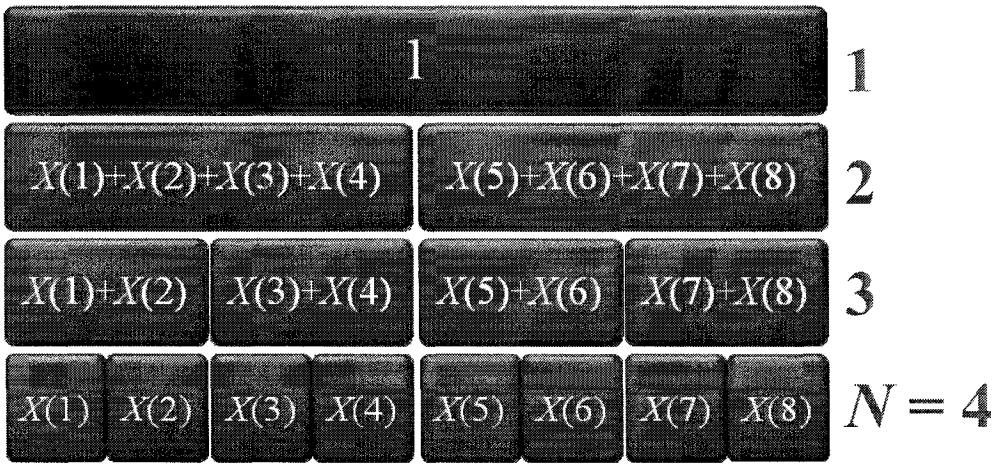

Figure 3.5: Schematics of reverse MCM modeling for a signal with 8 samples.

The generalized dimension spectrum D_q could be computed readily with Eq.(3.21), based on a MCM model similar to Figure 3.5 (in this case with 4 stages) [Gao *et al.*, 2007]. Moreover it is possible to show that the multipliers show a normal distribution around 0.5 for experimental data and that the variance of their distribution is closely related to randomness, long memory, and the Hurst exponent [Gao *et al.*, 2007; Kantelhardt *et al.*, 2001, 2002].

Several interesting models have been based on such multiplicative procedure in science and engineering with different multiplier probability distributions (e.g., binomial, Gaussian, and etc), for example for modeling turbulent fluid with a Poisson distribution [She *et al.*, 1991].

In chapter 7, we introduce MCM for the analysis of MESs. We show the simulated needle MESs exhibit multi-fractal characteristics. We also introduce a new method for discerning neuropathic signals based on MCM.

3.5. Chaotic time series analysis

So far with random fractal theory we have been assuming that the MESs are inherently random. Such signals could be presented in the form of a fractional-order differential equation.

Let us pose the question: can a highly irregular time series arise from a deterministic system which has a few degrees of freedom and state variables instead of a random system? The answer is yes; a chaotic system is capable of just that [Sprott, 2003]. This is also referred to as chaos theory. At the center of chaos theory is the concept of sensitive dependence on initial condition; that is, a minor disturbance in the initial conditions of a chaotic system leads to entirely different outcomes. Mathematically, sensitive dependence on initial condition is characterized as an exponential divergence in this form

$$\xi(t) \sim \xi(0) e^{\lambda_1 t}, \qquad (3.24)$$

where $\xi(0)$ is a small disturbance at time 0 causing a small divergence between two trajectories, $\xi(t)$ is the effect of that small disturbance at time t which is a large exponential divergence between the two trajectories, and λ_1 is the largest positive Lyapunov exponent. Moreover, because the trajectories are bounded after an exponential divergence they are on average attracted to a point in the phase space known as a strange attractor, which is also characterized by its power-law behaviour and is a fractal [Hu, 2007]. Conventionally, it is assumed that a time series with an estimated positive largest Lyapunov exponent and a fractal dimension is chaotic (however a counter-example is a $1/f$ process, this will be further discussed shortly). This is the basis for the dynamical test of chaos in which a set of phase space vectors are constructed by embedding and delaying a time series of the form

$$V_i = [X(i), X(i+L), ..., X(i+(m-1)L)], \qquad (3.25)$$

where m is called the embedding dimension and L the delay time. After phase space construction the Lyapunov exponents could be estimated. There are several approaches for estimation of Lyapunov exponents. In this work we will describe an interesting approach with which it is also possible to optimize the embedding of Eq.(3.25), known as time-dependent exponent curves [Gao and Zheng, 1994]. In this approach a set of measures are defined in this form

$$\Lambda(k) = \left\langle \log\left(\frac{\|V_{i+k} - V_{j+k}\|}{\|V_i - V_j\|} \right) \right\rangle, \qquad (3.26)$$

where $< >$ denotes ensemble average of all possible pairs of (V_i, V_j) defined by Eq.(3.26). The most remarkable feature of Eq.(3.26) is that $\Lambda(k)$ also includes a notion of scale where the scale is k denoting the difference between the phase space vectors in the numerator also known as evolution time. Moreover, $\Lambda(k)$ could be used to estimate the Lyapunov exponents on a wide range of scales determined by the evolution time k as

$$\log \xi(k) \approx \Lambda(k) = \left\langle \log\left(\frac{\|V_{i+k} - V_{j+k}\|}{\|V_i - V_j\|} \right) \right\rangle. \qquad (3.26)$$

Now back to the dynamical test for chaos. It is possible to show that a $1/f$ process might have a positive Lyapunov exponent; moreover, as we have shown in the beginning of this chapter a $1/f$ process also has a fractal dimension. But clearly a $1/f$ process could be inherently random and not chaotic. This is where the conventional dynamical test for chaos fails.

In the reminder of this section we will present a new concept known as power-law sensitivity to initial condition, which was first introduced by Gao *et al.* [2007]. This provides an interesting framework within which it is possible to address the shortcomings of the dynamical test for chaos in the case of $1/f$ processes and also bridge the gap between random fractal theory and chaos theory [Cencini *et al.*, 2000]. Moreover, this new concept also helps in better understanding of MESs and answering this question: is MES random or chaotic?

3.3.1. Power-law sensitivity to initial condition

Let us recall the essence of chaos which was exponential sensitivity to initial condition and was represented in this form

$$\xi(t) \sim \xi(0) e^{\lambda_1 t}, \qquad (3.28)$$

which satisfies

$$\frac{d\xi(t)}{dt} \sim \lambda_1 \xi(t). \qquad (3.29)$$

Now consider a generalized form of Eq.(3.29) in this form

$$\frac{d\xi(t)}{dt} \sim \lambda_q \xi(t)^q, \qquad (3.30)$$

where the parameter q has been introduced. When $q = 1$, Eq.(3.30) reduces to the conventional exponential sensitivity to initial condition of Eq.(3.29) and characterizes a chaotic time series. But when $q < 1$, as we will show, Eq.(3.30) interestingly includes $1/f$ processes. Recall a $1/f$ time series $\{X(t)\}$ and its power-law behaviour which was reflected in the variance as

$$Var[X(t)] = \lambda^{-2H} Var[X(\lambda t)], \qquad (3.31)$$

where H is the Hurst exponent. Eq.(3.31) implies the variance of $\{X(t)\}$ increases with t in this form

$$Var[X(t)] = t^{H}. \qquad (3.32)$$

Consider Eq.(3.32) as a exponential divergence caused by the increasing variance with evolution of time and notice the striking similarity to the exponential sensitivity to initial condition. Eq.(3.32) also satisfies

$$\frac{dVar[X(t)]}{dt} = Ht^{H-1} = HVar[X(t)]^{1-\frac{1}{H}}, \qquad (3.33)$$

and by translating Eq.(3.33) into the form of Eq.(3.30), we find that

$$q = 1 - \frac{1}{H}, \qquad (3.34)$$

and

$$\lambda_q = H, \qquad (3.35)$$

where for a valid Hurst exponent in the range $0 < H < 1$, the parameter q is within this range $-\infty < q < 0$. This explains why, for a $1/f$ time series, the largest Lyapunov exponent is positive and the time series also has a fractal dimension while it is not chaotic; that is, the divergence of variance which is an immediate result of statistical self-similarity resembles exponential sensitivity to initial condition and could be mistaken as chaos.

Interestingly, the above discussion suggests the time-dependent exponent curves computed from the phase space vectors will also show power-law behaviour with the evolution time in the case of $1/f$ processes but they have a linear envelope for a chaotic motion. This could be used to characterize the edge of chaos in a time series and understand whether a time series is fully random, chaotic or neither [Gao *et al.*, 2007].

Now back to the neuromuscular system and MESs. As previously mentioned the neuromuscular system is comprised of both structured and highly non-linear deterministic (MUAPs) and random contributions (innervation). Figure 3.6, shows the time-dependent exponent curves for a typical surface MES with evolution time k, ranging between 1 to 100 when the embedding dimension m = 3, and time delay L = 1.

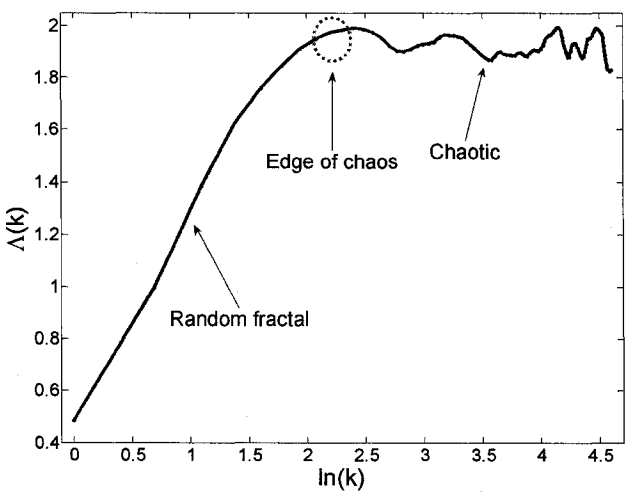

Figure 3.6: Time-dependent exponent curves for a typical MES. The plot implies the MES is neither fully random nor chaotic.

Figure 3.6, shows that in small scales (small evolution time before $e^{2.2}$) the MES exhibits random fractal like characteristics (power-law behaviour) and for larger scales chaotic characteristics (approximately constant envelope). Thus, the MES is neither fully random nor chaotic. This

result is expected given the origins of MESs which are not fully random or fully chaotic including structured deterministic and stochastic contributions. These results motivate applying random fractal theory in conjunction with chaos theory for characterization of MESs.

In Chapter 6, we will show the Hurst exponent computed using DFA is saturated around zero at higher scales where the samples do not show long-range correlations and are anti-persistent. The scaling in DFA is very close to the scaling involved for computing the time-dependent curves. An increased evolution time in Eq.(3.26), suggests a wider ensemble with more samples which is consistent with an increased scaling in DFA. According to the time-dependent exponent curves the signal resembles a chaotic motion at higher scales where the Hurst exponent is saturated around zero; thus, it would be interesting to characterize the complexity of the signal at these higher scales, especially because random fractal theory is not adequate. One way to deal with this problem is to employ time-dependent exponent curves. [Tsallis *et al.*, 1997]. Estimation of time dependent exponent curves is not easy and associates practical difficulties [Gao *et al.*, 2007]. This motivates using equivalent methods that are more appealing in terms of computation and provide a measure of complexity for chaotic motions similar to the time-dependent exponent curves. In Chapter 8, we will introduce the LZ complexity measure [Amigo, 2004; Costa *et al.*, 2005; SzcZepaski *et al.*, 2003], which is a scale-independent measure closely related to the time-dependent exponent curves. It provides a measure of deterministic complexity anticipated in chaotic time series. We will also introduce a new framework for fatigue estimation using the LZ measure.

3.4. Summary

In this chapter, four major paradigms for multi-scale analysis of MESs, 1) self-similarity, 2) long memory, 3) multi-fractality, and 4) chaos, were presented.

Each paradigm provides unique scale-dependent information about the MES. In the reminder of this work each of these aspects are exploited for force and fatigue estimation and discrimination between normal and neuropathic MESs.

Chapter 4

4. Simulated and experimental MESs

This chapter includes description of simulated and experimental MESs used in this work. In figure 4.1, the material that will be covered in this chapter is illustrated.

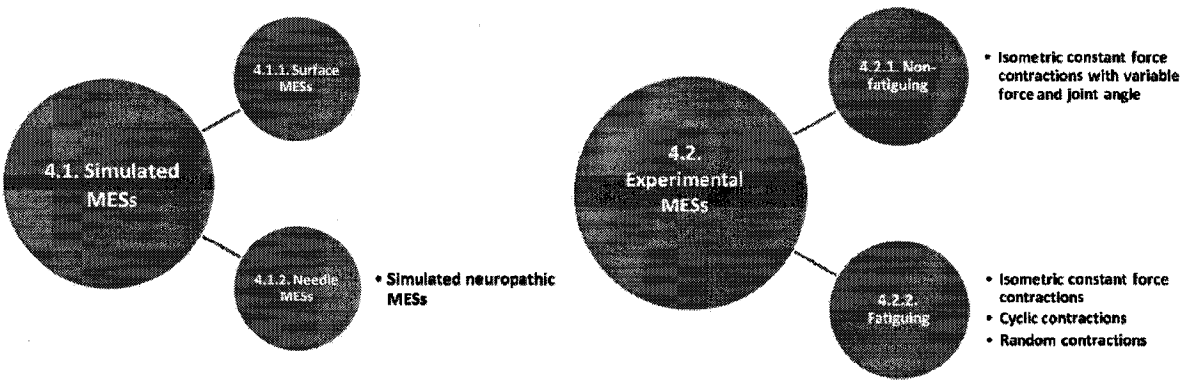

Figure 4.1: Diagram of material covered in chapter 4.

4.1 Simulated MESs

4.1.1. Simulation of surface MESs

As presented in chapter 2, the MU is the smallest independent functional unit of skeletal muscle, consisting of an α-motoneuron, the descending axon, and the muscle fibers that it innervates. An activated α-motoneuron sends out a series of neural firings to the muscle fibers. The timing of each firing, can be modeled as a stochastic point process, which contains important information regarding the underlying neural structures and strategies of the motor control scheme [Farina *et al.*, 2001, 2002]. During an isometric constant force contraction, the α-motoneuron firing sequences can be further modeled as renewal processes, in which case the inter-pulse intervals

have identical, independent probability distribution functions. Therefore, the simplest simulation model for sequences of α-motoneuron firings is to generate independent sequences of random numbers with an appropriate probability distribution; however, this assumes that there exists no inter-correlation among the sequences of different α-motoneurons, which is not valid in general. This has led to introduction of simulation strategies which take into account the MU synchrony [Merletti and Parker, 2004] and common drive [De Luca, 1982], which are out of the scope of this work.

An activated muscle fiber produces an electrical depolarization, known as the single fiber action potential (SFAP). SFAPs originate at the motor end plate, which is the point where the motor nerve innervates the muscle fiber, and propagates down the fiber axis. The summation of the SFAPs from the muscle fibers within a motor unit is known as the MUAP as shown in figure 4.2.

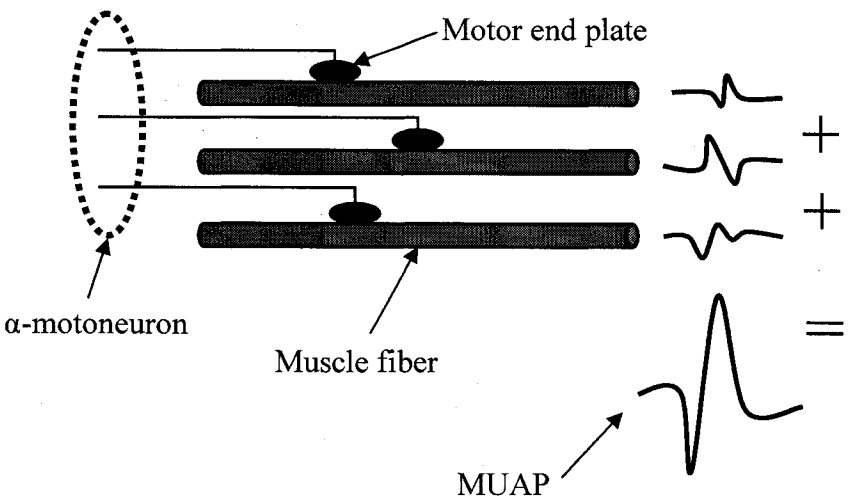

Figure 4.2: Schematics of MUAP generation from the superposition of SFAPs.

Each MUAP has the same wave shape if the measurement geometry remains constant because the action potentials are all-or-nothing phenomena. The MUAP train can be modeled as the

mathematical convolution of the firing instants (a sequence of impulses) with the MUAP wave shape. The MES can be considered as a signal where the contributions of all active MUs are summed. Contributions of the individual MUs can barely be recognized because of the extensive overlapping when there are a large number of active MUs. Nevertheless, the surface MES's global characteristics are largely dependent on the properties of the contributing MUs such as number, firing rate, and depth of active MUs and muscle conduction velocity; Figure 4.3 shows a schematic of MES generation.

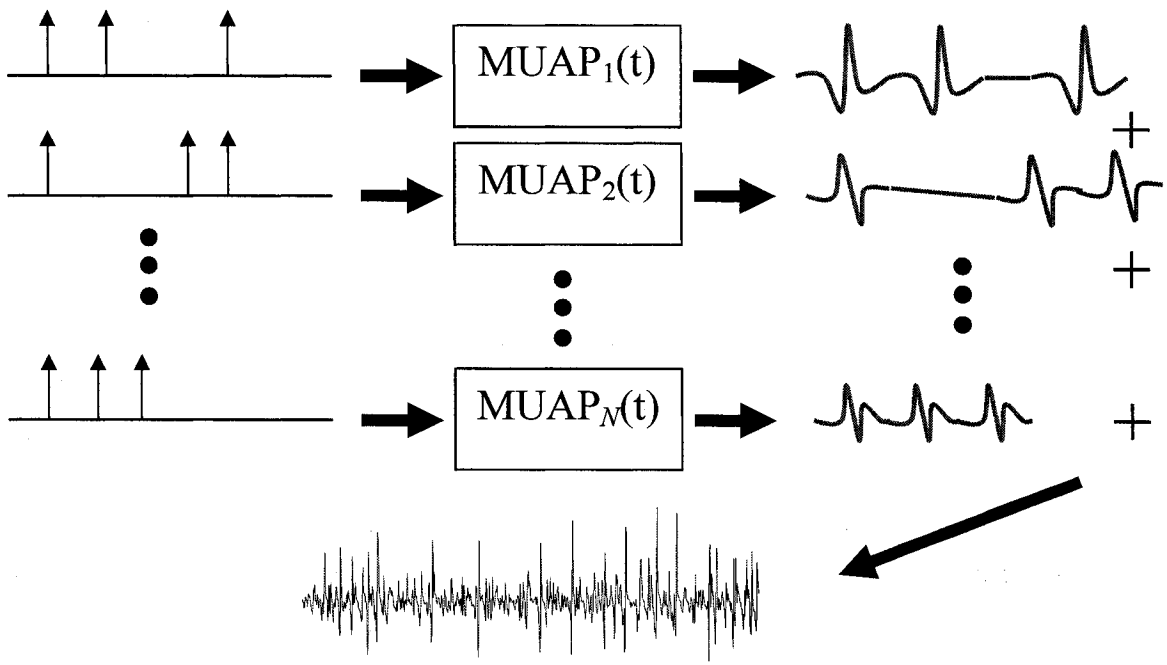

Figure 4.3: Schematic of MES generation from superposition of MUAPs.

The total duration of a single fiber depolarization is around 2-3 ms according to [De Luca, 1989] and other similar studies [Merlleti and Parker, 2004]. The number of fibers in a MU is greatly variable. Ideally, it is of interest to randomize the number of fibers in each MU with a normal

distribution with mean around 40 and variance around 20. The biceps contains 100 to 300 MUs. For moderate contractions 10 to 30 active MUs is very much consistent with experimental data. For higher level contractions it is not expected that 50 MUs fire at one time. For an average biceps length around 10 to 15 cm, expected fiber length is 2 to 3 cm. Considering the innervation zone at the belly of the biceps (right in the middle of biceps) a standard electrode location is 2 to 3.5 cm away from the innervation zone. It is very important that the electrode is not exactly on the innervation zone as it was discussed in chapter 2. The innervation zone will have some dispersion which is normally assumed to be around 2 to 3 mm for a healthy muscle. The inter-pulse intervals between the MUAPs or the firing rate is expected to be around 100 ms or 10 Hz for moderate contractions with some deviation the firing rate is likely higher around 50 ms or 20 Hz for higher levels of contraction. The depth of detected MUs is greatly influenced by the fat layer under the skin and other physical characteristics of a human. According to experimental data and by comparison of the MDN and bandwidth of experimental and simulated MESs, on average it could be anywhere between 5 to 20 mm. The muscle fiber conduction velocity is reported to be around 6 to 8 m/s for a non-fatiguing condition and could decrease to 2 to 3 m/s [De Luca, 1989]. To emulate the effects of muscle length (joint angle), and fatigue the depth of detected MUs and muscle fiber conduction velocity could be manipulated.

A set of simulation parameters for surface MESs, for an average size muscle like the *biceps brachii*, which are very useful for researchers to unify their simulations and repeatability of their experiments, are integrated and presented in table 4.1. Values are based on the references and discussions presented in this section.

Table 4.1: Myoelectric parameters for simulation of surface MESs during biceps contractions.

Depolarization duration	# of fibers in MU	# of active MUs	Length of fiber	Distance from innervation zone to electrode
2-3 ms	20-60	10-50	2-3 cm	2-3.5 cm
Innervation zone dispersion	**MUAP inter-pulse interval**	**Depth of detected MUs**	**Muscle fiber conduction velocity**	**Electrode properties**
2-3 mm	50-100 ms σ = 10-20 ms	5-25 mm σ = 5-10 %	2-8 m/s σ = 3-5 %	Bi-polar with 4-5 cm separation between the poles

4.1.2. Simulation of needle MESs

Most commonly clinical MES analysis is performed using needle recordings. The essentials of needle recording were presented in chapter 2. The principles of simulation for needle recordings are also very similar to the discussions that were presented in the previous section. There are several available software applications for simulation of intramuscular MESs; in this work we use a simulator previously developed by Hamilton-Wright and Stashuk [2005]. This simulator is interesting because it allows for emulating neuromuscular disorders including the myopathic and neuropathic conditions that were explained in section 2.5.3.

In the model, MUs are positioned within a circular cross section of a cylindrical muscle. The overall muscle radius is estimated based on the number of MUs to be simulated, their expected MU territory diameters and fiber densities. The algorithm used to position MU territory centers is analogous to the scattering of seeds across a surface. A given MU territory center location is determined by adding a random number and offset to a point randomly chosen from a regular grid. Once MU territory centers are placed, fibers are assigned to MUs. This process occurs as the axon of a motor neuron grows into a region of muscle and produces twigs which attach to a set of nearby fibers. This development, over a cross section of mature muscle fibers, appears to be randomly assigned among the selection of MUs which cover the region. Muscle fibers of

different MUs appear to be randomly interleaved and adjacent fibers are not likely to belong to the same MU. The last step in the physical construction of the muscle is to determine the coordinate of the neuromuscular junction for each fiber. The neuromuscular junction positions, and muscle fiber conduction velocities, are the major causes of temporal dispersion among the muscle fiber potential contributions of the fibers within an MU and, hence, of the complexity of the MUAP spike component. The neuromuscular junction locations for a single MU are assumed to be Gaussian distributed with zero mean, and a standard deviation based on the MU territory diameter. During signal simulation the electrode tip or side port location is typically specified in order to explore various quadrants of a muscle. Figure 4.4, shows a schematic of a muscle, MU, fibers, and electrode based on this model.

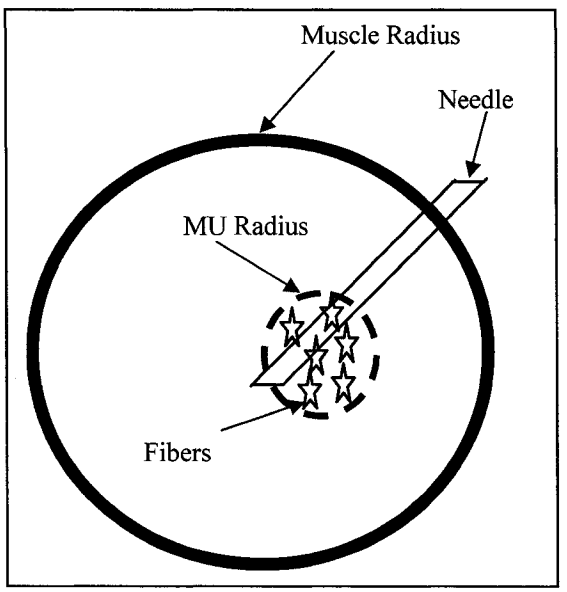

Figure 4.4: Location of muscle, MU, and fibers relative to a concentric needle electrode. Based on [Hamilton-Wright and Stashuk, 2006].

This model incorporates important aspects of neuromuscular physiology and the development of the physical structure and organization of muscle, and MESs generated by this model reflect the

structure and activity of a muscle in a way similar to the reflection provided by real signals detected from real muscle. Table 4.2, summarises the model parameters used for simulation of intramuscular MESs.

Table 4.2: Myoelectric parameters for simulation of needle MESs during biceps contractions.

# of MUs	# of fibers in MU	Muscle fiber density	Muscle fiber area	MU diameter
200	40 $\sigma = 20$	10 mm^2	0.0025	Min: 2 mm Max: 8 mm
Firing rate	**Produced force**	**Electrode properties**	**Neuropathic affection**	**Reference setting**
Min: 8 Hz Max: 20 Hz	10 % of maximum voluntary contraction	Concentric Cannula radius and length = 0.5 and 10 mm	50 % of the muscle fibers	Tip versus cannula

More details on this simulator can be found in [Hamilton-Wright and Stashuk, 2006]. Additional settings were considered for neuromuscular disorders. For simulation of neuropathic MESs the model allows MU enlargement and de-ranged neuromuscular junctions by adjusting a parameter between 0 to 75 %, which denotes the percentage of MUs that are affected by enlargement and de-ranged neural drive. We simulated neuropathic signals when 50 % of the muscle fibers were affected by the neuropathic condition.

4.2. Experimental MESs

4.2.1. Non-fatiguing isometric constant force contractions

Data were collected from ten healthy males (age 22 to 34; average age 26). MES signals were recorded from the belly of the *biceps brachii* of the right arm using surface Duotrode electrodes (Myotronics, USA, model 6140), which are an Ag-AgCl electrode pair spaced 1.9 cm apart. An Ag-AgCl Red Dot electrode (3M, USA, model 2237) was placed on the elbow as a reference

electrode. The MESs were amplified (Grass-Telefactor, USA, model 15A54) and sampled at 1000 Hz using a 12-bit analog-to-digital converter board (National Instruments, USA, model PCI-6071E). The amplifier's variable gain was adjusted between 100 and 1000, such that the maximum dynamic range of the analog-to-digital converter was used without over-ranging. The amplifier's filters were set with a pass band of 1 Hz to 300 Hz. This frequency range was assigned considering the higher degree of self-affinity of the MES obtained using local fractal analysis in the range of 20 Hz to 280 Hz. This research was reviewed and approved by the Carleton University Research Ethics Committee.

A central pulley apparatus, shown in Figure 4.5, was used to elicit constant force contractions at four joint angles: 60°, 90°, 120°, and 150°, where 180° is considered full elbow extension. Three weights were used in this study: 1.13 kg (2.5 lb), 2.27 kg (5 lb), and 3.40 kg (7.5 lb), requiring a moment of 16 N, 32 N, and 48 N on the handle, respectively, to maintain a constant joint angle. The moment is always orthogonal to the line connecting the handle to the center of the apparatus. Each contraction was held for 18 seconds and there was at least 1 minute of rest between each trial to avoid muscle fatigue. The first 3 seconds of recorded data during the 18 second contractions were removed before processing to avoid the transitional period. Each subject repeated the contractions for all twelve joint angle-force combinations three times. Joint angle-force combinations were randomized to avoid ordering effects.

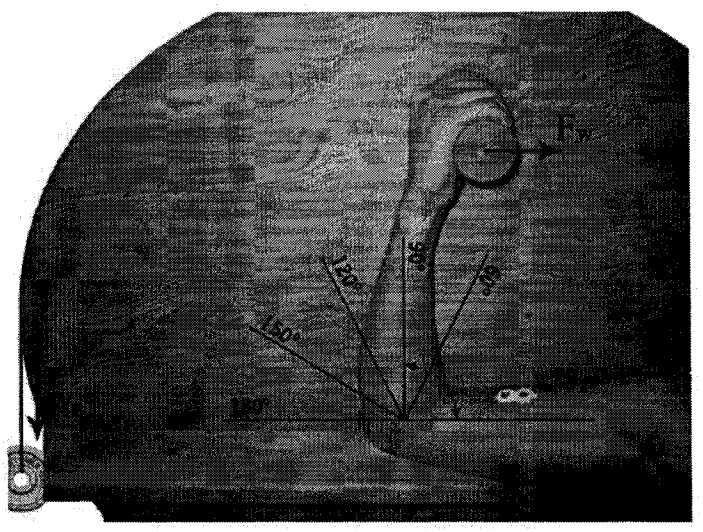

Figure 4.5: Central pulley apparatus, where w_n is the weight and F_w is the required moment by the weight.

Pre-processing noise reduction (i.e., in particular 60 Hz power line noise) and power spectrum estimation are critical stages in MES processing. A reference 60 Hz power line noise was simultaneously recorded during the data collection. Using this noise data, power line interference was filtered out from the MES data using a second order recursive least squares adaptive noise cancellation filter [Monson, 1996].

4.2.2. Fatiguing contractions

These data were previously reported in [MacIsaac *et al.*, 2006]. Ten healthy subjects (average age 25 years) participated in this experiment. The apparatus used during the fatigue tests consisted of a large disc attached to a central pulley at its axis as previously described in [MacIsaac *et al.*, 2001b]. The central pulley and disc were supported with a frame allowing each participant to rest the upper arm upon a platform while flexing and extending at the elbow which was aligned with the pulley-disc axis (similar to the apparatus shown in Figure 4.5). The disc-pulley apparatus was equipped with an ergonometer so that joint angle could be monitored and

recorded. The ergonometer also was used to provide a visual target for the user to have real-time feedback on their joint angle.

During the full course of each fatigue test, the surface MES was measured from the *biceps brachii* using a set of Ag-Ag/Cl Red Dot surface electrodes. Electrodes were placed midway between the belly of the muscle and the tendon on the proximal side, approximately 2 cm apart, in bipolar configuration. From the electrodes, the MES was processed first through a preamp configuration described previously in [Lovely, 1993], and then through a Tektronix AM502 differential amplifier system. The combined gains were set between 1 K and 40 K, depending upon the participant, and the low and high cutoff frequencies of the amplifier were set to 1 Hz and 1000 Hz, respectively. From the amplifier, the signal was connected to an oscilloscope for display, and through an anti-aliasing filter (cutoff frequency, f_c = 500 Hz) for digital storage. Both the MES and the signal from the ergonometer were sampled at a rate of f_s = 1024 Hz and recorded through a National Instruments CIO-DAS16/33i A/D board as described previously in [MacIsaac *et al.*, 2006].

Each participant underwent three fatigue tests: 1) static test, 2) cyclic test, and 3) random test. For the static test, each participant held a load (30% of a maximal voluntary contraction held at 130°) with the elbow fixed at 90° until the static position could no longer be maintained. For the cyclic test, participants flexed and extended at the elbow to track a target displayed on a computer screen until the arm could no longer be lifted through the motion. The target moved cyclically between 50° and 130° at a rate of about 32°/s. For the random test, participants also tracked the target until the arm could no longer be lifted through the motion, but for this test the target moved randomly according to a uniform distribution between 50° and 130°, also at a rate

of about 32°/s. During all three tests, participants received real-time tracking feedback by observing a signal from the ergonometer, properly calibrated, on the computer screen alongside the target. Because a number of reasons can cause participants to end a fatigue test without fatiguing (psychological motivation, non-muscular related injuries etc.), a downward trend in sequential MDN estimates obtained from static MES segments was used to verify that myoelectric changes were manifesting as fatigue progressed, so it was necessary to intermittently interrupt each dynamic test with a static contraction. Thus, at the beginning of every minute during both the cyclic and random fatigue tests, the target remained fixed at 90° for 10 s as described previously in [MacIsaac *et al.*, 2006]. An ANOVA analysis was then employed to confirm the presence of myoelectric manifestation of fatigue for all data. The ANOVA tested for significant slope of changes in the MDN (significance threshold $\alpha_T = 0.05$), which indicates the presence of myoelectric manifestation of fatigue. The presence of myoelectric manifestation of muscle fatigue was confirmed for all tests and all subjects as the MDN exhibited a significant downward slope ($p < 0.05$).

A reference 60 Hz power line noise was simultaneously recorded during the data collection. Using this noise data, power line interference was filtered out from the MES data using a second order recursive least squares adaptive noise cancellation filter as described previously in section 4.2.1.

This chapter included description of simulated and experimental MESs used in this work. The experiments and results carried on these data will be presented in next chapters.

Chapter 5

5. Self-similarity: Bi-phase power spectrum method

The ubiquity of confounded force, muscle length (joint angle), and fatigue effects in MESs was covered in section 2.4. It was also demonstrated in section 3.2.2, that the MES power spectrum is not mono-phase. In this chapter we introduce a bi-phase power-law which could be used to characterize an extended form of self-similarity. A novel power spectrum-based method, named BPSM, for multi-scale analysis of MESs is also presented. Using human experimental data, we show BPSM provides parameters that have distinct sensitivities to force, muscle length (joint angle), and fatigue.

5.1. Extended self similarity and bi-phase power-law behavior

The MES power spectrum does not resemble mono-phase $1/f$ characteristics (section 3.2.2). The power spectrum of surface recordings of the MES, during moderate contractions, exhibits a bi-phase curvature; this is what motivated Raveir *et al.* [2005], to propose a piecewise $1/f$ approach. As previously discussed in section 3.2.2, this method has its limitations.

We take a step ahead and push the envelope even more and ask this question: are there other forms of self-similarity which better represent MESs? The answer to this question is yes. As we zoom into a signal, if the functional form of samples or the distribution of samples remains unchanged and only scaled, self similarity is observed. In case of $1/f$ processes, the functional form of the distribution of samples is preserved with magnification and they are subjected to a scaling and show a power-law regime which is regulated with a single fractional-order. The key to a more general form of self-similarity is that the scaling could be regulated with more than a

single fractional-order. For example, in the case of the MES power spectrum a tempting power-law is one that is bi-phase regulated by two fractional-orders; a fractional-order for lower frequencies and a fractional-order for higher frequencies.

Following Tatom [1989], we propose a bi-phase power-law in this form

$$S(f)=c\left(\frac{f}{f_0}\right)^{2g}\Big/\left(\left(\frac{f}{f_0}\right)^{2}+1\right)^{q+g}, \qquad (5.1)$$

where $S(f)$ denotes the power spectrum of the time series $X(t)$, c is a scaling factor related to the energy of the signal according to Parsval's theorem [Monson, 1996], g is a fractional-order regulating the power-law in lower frequencies, q is a fractional-order regulating the power-law in higher frequencies, and f_0 is a characteristic frequency in which the power spectrum phase changes and governs the separation of high and low frequency partitions [Talebinejad *et al.*, 2008e].

The most remarkable characteristic of this bi-phase power-law is that a time series with such power spectrum shows extended self-similarity in this form

$$\Pr[X(t;f_0)]=\frac{\lambda^g}{\lambda^{q+g}}\Pr[X(\lambda t;f_0/\lambda)], \qquad (5.2)$$

which denotes by scaling the time axis or magnification of the time series $X(t)$ with λ, the functional form of the probability distribution of samples is preserved and they are only subjected to a scaling and show a power-law regime in form of the Eq.(5.1) which is regulated by two fractional-orders (Appendix B, shows the derivation of Eq.(5.2)). Central to a bi-phase power-law is the assumption that the process is inherently random and the underlying system responsible for it has infinite degrees of freedom and state variables, and is in the form of a fractional-order differential equation with two fractional-orders. This concept was discussed in

section 3.5 along with the chaos theory. Figure 5.1, shows a typical MES power spectrum, recorded from the *biceps* during a moderate contraction, modeled using the bi-phase power-law.

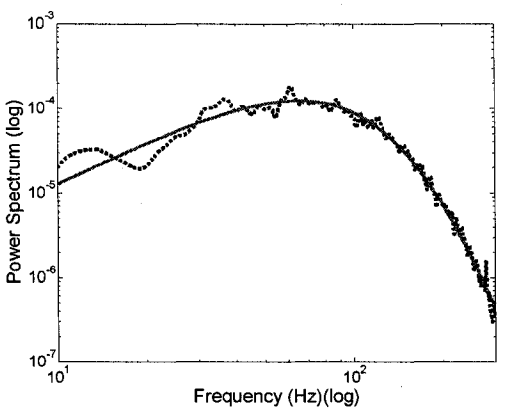

Figure 5.1: A typical MES power spectrum modeled using the bi-phase power-law.

The bi-phase power-law provides an accurate approximation for the MES power spectrum, which suggests MESs show extended self-similarity. The bi-phase power-law also implies that the high and low frequency content of the MES show distinct self-similarities, and the superposition of them shows an extended form of self-similarity.

This bi-phase power-law leads to several interesting properties. First of all, q and g give distinct frequency association; that is, the asymptotic form of the power-laws in the higher and low frequency ranges are independent from each other which can be written in a slope-intercept form (i.e., $y = mx + b$) as

$$S(f)_{dB} \approx 2g \cdot 10\log_{10}\frac{f}{f_0} + 10\log_{10} c \qquad \text{for} \qquad 0 < f << f_0, \qquad (5.3)$$

$$S(f)_{dB} \approx -2q \cdot 10\log_{10}\frac{f}{f_0} + 10\log_{10} c \qquad \text{for} \qquad f >> f_0, \qquad (5.4)$$

where in Eq. (5.3) and Eq. (5.4) the asymptote slopes are controlled separately by g and q, the static gain c controls the intercept of the high and low frequency power spectrum, and f_0 is the knee frequency. In this chapter, we will exploit this characteristic and demonstrate that q and g

could be used to separate the effects of force and joint angle which are confounded in conventional MES parameters [Talebinejad *et al.*, 2006, 2007, 2008a].

Moreover, a frequency compression (i.e., scaling in the frequency domain, $f \rightarrow \beta f$), will not affect the fractional-orders; that is, the fractional-orders are insensitive to spectral compression due to the homomorphism of the power-law. In this chapter, we will exploit this characteristic and demonstrate that the q and g are also insensitive to muscle fatigue and spectral compression due to decreased muscle fiber conduction velocity, and q could be used for force estimation during fatiguing contractions which is not possible using the conventional MES parameters [Talebinejad *et al.*, 2007, 2008c, 2008d].

5.1.1. Power-law estimation

It is also important to note that the optimization in $1/f$ approaches is trivial and can be easily accomplished (e.g., least squares line fitting). The general estimation problem for the four parameters of Eq. (5.1) is not easily solved, mainly because of difficulties in linearizing $S(f)$ with respect to f_0; however, once an estimate for f_0 is established, estimates for q, g and c can be computed using a standard least squares method. After the computation of q, g and c, an iterative procedure can be adopted to refine the f_0 estimate. We propose an optimization algorithm for the bi-phase power-law of Eq.(5.1). First, we rewrite Eq. (5.1) and let ($Q = q + g$, $G = g$, and $K = cf_0^{2q}$), in this form

$$S(f) = K\left(f^{2G}\right)/\left(f^2 + f_0^2\right)^{Q}, \qquad (5.5)$$

which is less constrained for linearizing and easier to manipulate. Now, consider a logarithmic error function $e(Q, G, C, f_0)$ in the following form with $C = \log K$,

$$e(Q,G,C,f_0) = \frac{1}{N}\sum_{i=1}^{N}\left(\log S(f_i) - \log \hat{S}(f_i)\right)^2 \qquad (5.6)$$

where $\hat{S}$ is the estimated power spectrum of the signal, S is the power spectrum of the model, N is the number of power spectrum samples, and f_i is the corresponding frequency of the i^{th} sample. Having an estimate for f_0 (the peak frequency f_m of $\hat{S}$ can be used for the first iteration), Eq. (5.6) is minimized when $\partial e/\partial G = \partial e/\partial Q = \partial e/\partial C = 0$. Differentiating Eq. (5.6) with respect to Q, G, and C, it is easy to show how these parameters can be estimated by a standard least squares approach and by solving a linear system of equations [Talebinejad *et al.*, 2008e] (Appendix C, shows the standard least squares solution). In our proposed algorithm, we perform a partial differentiation on the error with respect to f_0, and compute the new estimate of f_0 by finding the root of the non-linear function of one variable in the form

$$\frac{\partial e}{\partial f_0} = \frac{1}{N}\sum_{i=1}^{N}\left(\log S(f_i) - \log \hat{S}(f_i)\right)\left(\frac{2Qf_0}{f_0^2 + f_i^2}\right) = 0 . \qquad (5.7)$$

We use an inverse quadratic interpolation method [Brent, 1973] to obtain a solution for Eq. (5.7). The solution is used for updating the parameters computed using the least squares iteratively until Eq.(5.6) is lower than some threshold in this algorithm. This approach results in values for the four parameters by minimizing the logarithmic error of Eq. (5.6).

But before proceeding any further let us repeat this question again: how does bi-phase power-law behavior and extended statistical self-similarity help us with multi-scale analysis? Well, according to Eq.(5.2) the fractional-orders could be used to characterize a signal on a wide range of scales where the scale is λ.

5.2. Experimental methods

5.2.1. Data

MES data used in this experiment were previously described in section 4.2. The non-fatiguing data were used to investigate the effects of force and joint angle on fractional-orders. The data recorded during fatiguing static contractions were used to investigate the effects of fatigue on fractional-orders.

5.2.2. Analytic methods

Five methods were evaluated and compared: the Katz method [Katz, 1988], the box-counting method [Turner *et al.*, 1998], the piecewise $1/f^{\alpha}$ approach [Ravier *et al.*, 2005], the proposed BPSM approach, and the MDN routine.

The power spectrum is used for the latter three methods. The power spectrum of the MES was estimated using Welch's method [Monson, 1996], which is a non-parametric method. The ergodicity and pseudo-stationary characteristics of MESs make them well suited for a time-slice averaging algorithm such as Welch's method compared to the periodogram, which is not statistically consistent for estimating the power spectrum [Monson, 1996]. For averaging, a Hamming window with a temporal width of 256 samples (0.256 sec) was applied, with a 50 % window overlap.

5.2.2.1. Katz method

The eFD was computed for the Katz method [Katz, 1988], using the following equation, applied to the interference pattern,

$$eFD = \frac{\log(n)}{\log(n) + \log\left(\frac{d}{L}\right)} \qquad (5.8)$$

where n is the number of samples, L is the total length of the planar waveform and d is the measurement diameter. In this method, the total length L (i.e., the sum of all distances between successive points) and the diameter d (i.e., the farthest distance between the first point and any other point) are estimated directly from the signal's interference pattern.

5.2.2.2. Box-counting method

The eFD computation for the box-counting method [Turner *et al.*, 1998] was performed by first covering the MES interference pattern by square boxes with side lengths of $1/2^m$, where m is the recursion number (an integer between 1 and 8 in this study). The slope of the bi-logarithmic plot of the number of boxes versus the box side length was then computed using a linear least squares regression.

5.2.2.3. Piecewise $1/f^{\alpha}$ approach

To compute the spectral slopes using the piecewise $1/f^{\alpha}$ approach [Ravier *et al.*, 2005], Welch's estimated power spectrum was partitioned according to the peak frequency f_m, and then spectral slopes were computed using a least squares line fit on each partition of the power spectrum. The frequency range for linear regression was 20 Hz to 280 Hz. This frequency interval generally contains most of the spectral information for a MES [Merletti and Parker, 2004]; moreover, it is shown that the degree of self-affinity is higher in this range.

5.2.2.4. Bi-phase power spectrum method

The BPSM parameters were computed from the estimated power spectrum according to the method described in section 5.1.1. The lower and higher frequency limits for regression were 20 Hz and 280 Hz, respectively. The error threshold of the iterative algorithm was set to 4e-8.

5.2.2.5. Median frequency

The MDN was computed as the 50^{th} percentile frequency from the estimated power spectrum in the 20 Hz to 280 Hz frequency interval for comparison to other indices.

5.2.2.6. Statistics

Statistical analysis was performed using a *general linear model repeated measures* [Field, 2005] procedure to examine two major issues:

1. Significant effects caused by the force and joint angle on the estimated parameters (sensitivity).

2. Consistency of sensitivity to force and/or joint angle, among the subjects.

To answer the first question, the probability value (p-value) obtained by the analysis of variances was examined and a binary decision was made. The hypothesis that the mean values of the measurements are the same and there is no sensitivity to force or joint angle is accepted if the p-values are greater than an alpha level of $\alpha_T = 0.05$; otherwise, it is accepted that there is sensitivity. To answer the second question, based on the inter-subject standard deviation and all single trials, the probability of seeing the sensitivity among the subjects is computed. For further

insight into the distinct sensitivity of parameters, a ratio of variation is also defined based on the range of changes with force and joint angle.

5.3. Results

5.3.1. Consistency of power spectrum modeling

Figure 5.1, shows an example of power spectrum modeling for one subject. The mean squared error of the piecewise $1/f$ approach, across all subjects, was as high as 20 % of the total energy under the power spectrum curve in some cases. The average mean squared error of piecewise linear modeling was 13.4 % of the total power spectrum energy.

The mean squared error of BPSM was less than 10 % of the total energy under the power spectrum in all cases. The average modeling error rate was 5.8 % of the total power spectrum energy. The average error rate shows the consistency of this approach between the subjects; it is not intended as a measure of goodness of the modeling. In addition to demonstrating good consistency of the BPSM in modeling the power spectrum, the error rate implies that all the data exhibit behavior close to a multi-scale self-affine signal. Higher error rates were obtained in a few subjects whose MES power spectrum was close to flat in the lower frequencies and/or the estimated characteristic frequency was very small.

5.3.2. Effects of force on fractional-orders and eFDs

The high frequency indicator q and scaling factor c computed using BPSM are significantly affected by changes in force ($p < 0.001$). Figure 5.2, shows a consistent trend between these indicators and force. Error bars of mean values show the inter-subject variations. The eFD using Katz method is also significantly affected by changes of force, in a manner similar to the RMS,

as shown in Figure 5.2. The low frequency indicator g, characteristic frequency f_0, spectral slopes and eFD using box-counting method are insensitive to changes of force ($p > 0.05$).

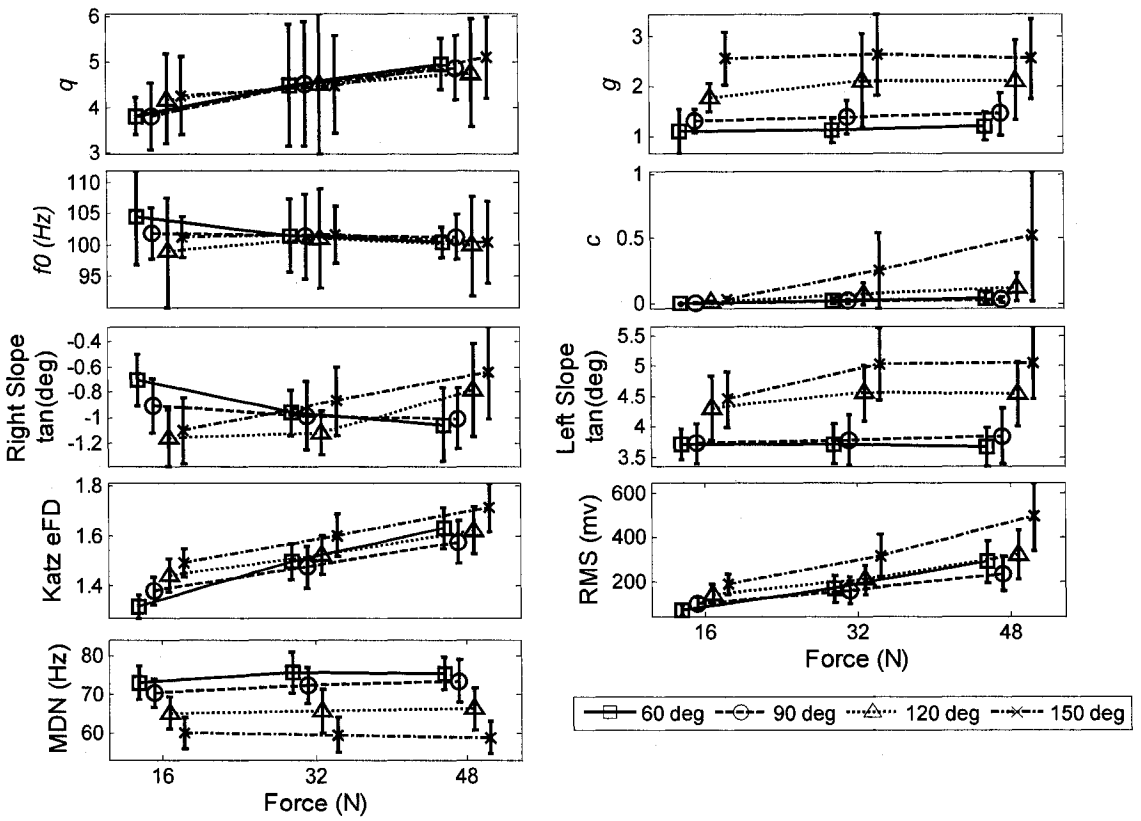

Figure 5.2: The BPSM fractional-orders, spectral slopes, Katz eFD, MDN and RMS vs. force level for different joint angles.

Table 5.1, shows the probability of having force sensitivity among the subjects. All the force sensitive parameters are reliable in the sense that they occur with high probability in this experiment.

Table 5.1: Probability of having a significant force effect among the subjects.

Parameter	q	c	Katz eFD	RMS
Pr[.]	91.67 %	95.83 %	100 %	100 %

5.3.3. Effects of joint angle on fractional-orders and eFDs

The low frequency indicator g, computed using BPSM and the left slope computed using the $1/f^{\alpha}$ method are significantly affected by changes of joint angle ($p < 0.001$). Figure 5.3, shows a consistent trend between these indicators and force. Error bars of mean values show the inter-subject variations. The eFD using the Katz method is also significantly affected by changes of force similar to the RMS as shown in Figure 5.3, as is the scaling factor c. The high frequency indicator q, characteristic frequency f_0, right slope, and eFD using box-counting are insensitive to changes of joint angle ($p > 0.05$).

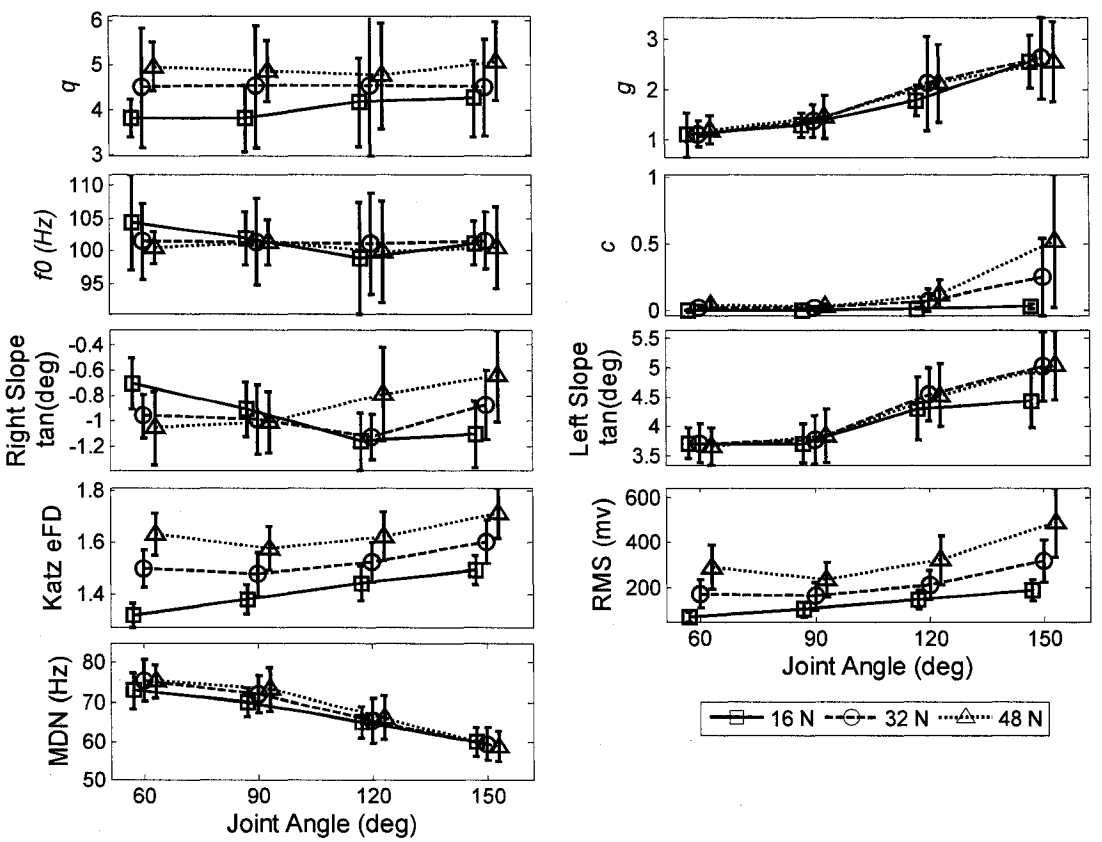

Figure 5.3: The BPSM FIs, spectral slopes, Katz eFD, MDN and RMS vs. joint angle for different force levels.

Table 5.2, shows the probability of having joint angle sensitivity among the subjects. All the joint angle parameters are reliable in this sense with having high probabilities in this experiment except for the left slope (Pr = 88.23 %).

Table 5.2: Probability of having a significant joint angle effect among the subjects.

Parameter	*g*	*c*	Left Slope	Katz eFD	RMS
Pr[.]	94.32 %	100 %	88.23 %	100 %	100 %

5.3.4. Effects of fatigue on fractional-orders

The high and low frequency fractional-orders are not significantly affected by fatigue (p = 0.453, 0.671). Figure 5.4, shows a consistent insensitive trend between the fractional-orders and fatigue. The characteristic frequency is correlated with time similar to MDN. The RMS is increasing with time; this increase does not affect the fractional-orders because its dynamics are different from a short contraction and recruitment is in an equilibrium state and not orderly according to the *size principle* paradigm.

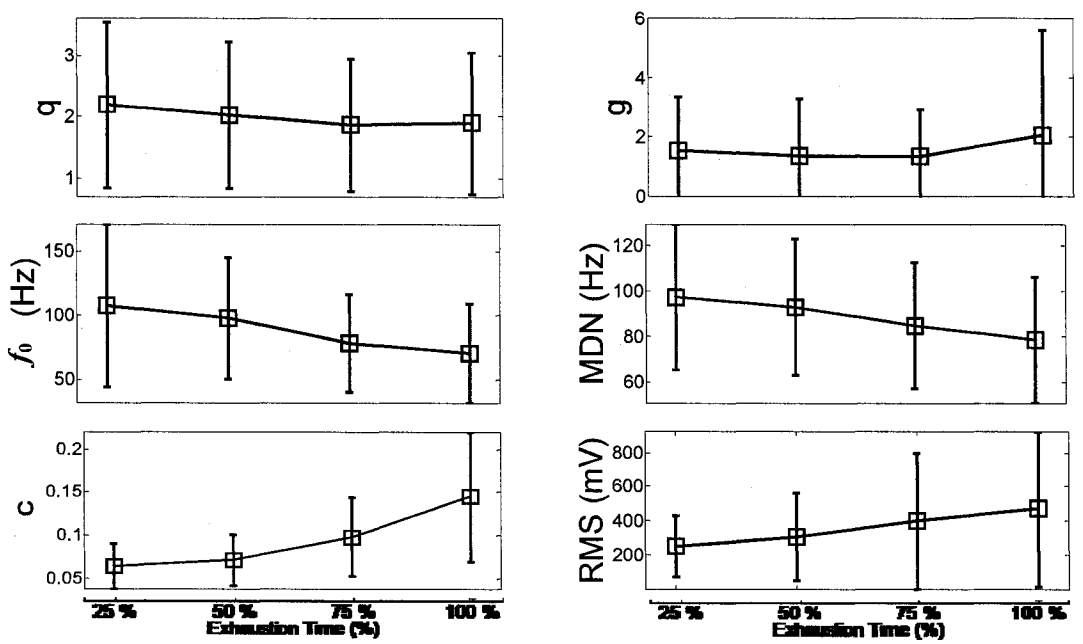

Figure 5.4: The averaged parameters and their standard deviations vs. progress of time.

5.3.5. Summary of the results and statistics

Table 5.3 summarizes the results of all parameters including the fractional-orders, eFDs, RMS and MDN.

Table 5.3: Analysis of variance p-values ($\alpha_T = 0.05$).

MES Parameter	Force	Joint Angle
q	**< 0.001**	0.241
g	0.234	**< 0.001**
f_0	0.112	0.095
c	**< 0.001**	**< 0.001**
Right Slope	0.272	0.721
Left Slope	0.213	**< 0.001**
Katz eFD	**< 0.001**	**< 0.001**
Box-Counting eFD	0.650	0.800
MDN	< 0.830	**< 0.001**
RMS	**< 0.001**	**< 0.001**

The p-values are compared to the significance threshold which is $\alpha_T = 0.05$; values higher than α_T imply insensitivity and values less than α_T indicate a significant effect (in bold). The Mauchly's Test of Sphericity validates the assumption of sphericity ($s = 2.21$).

The error rate of linear regression is also reported in Table 5.4, which inversely indicates the degree of linear correlation.

Table 5.4: Error (%) of linear regression.

MES Parameter	Force	Joint Angle
q	28.33 %	27.54 %
g	22.59 %	23.31 %
f_0	29.21 %	28 .50 %
c	22.39 %	21.63 %
Right Slope	27.32 %	28. 53 %
Left Slope	29. 66 %	28. 43 %
Katz eFD	15.75 %	15. 43 %
Box-Counting eFD	10.43 %	11.12 %
MDN	19.45 %	18.23 %
RMS	15.98 %	20.08 %

Table 5.5 presents the ratio of force-joint angle variation based on the ranges of indices to compare the variations caused by the force and joint angle.

Table 5.5: Ratio (%) between the variations of force and the variations of joint angle.

Parameter	Ratio
q	244 %
g	4 %
f_0	110 %
c	97 %
Right Slope	112 %
Left Slope	15 %
Katz eFD	115 %
Box-Counting eFD	105 %
MDN	6 %
RMS	117 %

5.4. Discussion

The sensitivity of the high frequency indicator q to force is due to changes of high frequency content of the signal from temporal and spatial MU recruitment; meanwhile, insensitivity of the low frequency indicator g to force is also consistent with the high frequency effects of the MU recruitment. These finding are also consistent with the improved force estimates obtained by high pass filtering of the MES in [Potvin and Brown, 2003], which suggest there are more force information in high frequency content.

The sensitivity of the low frequency indicator g to joint angle is due to changes of low frequency content of the signal from changes in tissue thickness and depth of the detected MUs; meanwhile, insensitivity of the high frequency indicator q to joint angle is also consistent with low frequency effects of the depth of MUs and our simulated studies [Talebinejad *et al.*, 2006b]. This also suggests that the recruitment variations caused by varying joint angle do not have a significant effect on the high frequency power spectrum.

The results show that the asymptotic high frequency power spectrum is mainly affected by the recruitment strategy, and effects of joint angle are very small on this frequency region. Results

also show that the asymptotic low frequency power spectrum is mainly affected by the joint angle and effects of force are very small on lower frequencies.

The insensitivity of the characteristic frequency f_0 to both force and joint angle is mainly caused by the fact that the underlying distributions are not consistently shifted towards higher or lower frequencies when the MUs recruitment and/or depth are changed.

The scaling factor c is sensitive to both force and joint angle because c reflects changes in the power and area under the power spectrum. The trends of c are close to RMS, which is expected as they both reflect the signal power.

The results of this experiment are consistent with our simulation studies with regards to the BPSM parameters and the effects of MU recruitment and depth of detected MUs [Talebinejad *et al.*, 2006a].

Overall, the eFD computed using the Katz method is confounded by force and joint angle effects. This eFD also mimics the RMS trends, which is consistent with the prediction of high correlation between this eFD and measures of the signal amplitude. The eFD using the box-counting method consistently saturates around 1.5, which explains its insensitivity to both force and joint angle.

The right slope of the piecewise $1/f^{\alpha}$ approach is insensitive to force. It was expected that sensitivity of the right slope to force would be observed because of the high frequency effects of MU recruitment, similar to the results of Ravier *et al.* [2005] and sensitivity of the high frequency indicator q; however, partitioning the power spectrum with respect to the peak frequency and modeling it using a bi-logarithmic line does not seem to show a significant effect in this experiment. Avoidance of the transitional period and the range of the applied weights in

our study may explain this inconsistency when compared to Ravier *et al.* [2005]. Insensitivity of the right slope to joint angle is also consistent with the low frequency effects of the MU depths.

Insensitivity of the left slope of the piecewise $1/f^{\alpha}$ approach to force is consistent with the high frequency effects of MU recruitment; meanwhile, sensitivity to joint angle is consistent with the low frequency effects of the MUs depth. The left slope is not as reliable as the other low frequency indicators in the sense of probability of consistency among the subjects in this experiment.

The ratio of variation also supports the results of analysis of variance in terms of sensitivity and shows that the ratio of force-joint angle variation is very high in q and very low in g, which also suggests that the ratio of joint angle-force variation is high and low for g and q, respectively. The high linear regression error rates suggest that although the trends are consistent a simple linear correlation should not be anticipated.

The fractional-orders q and g show distinct sensitivities to force and joint angle; this verifies the hypothesis of sensing the effects of force and joint angle exploiting the texture of the high and low frequency portions of the MES power spectrum. The eFD and RMS, however, are confounded by both force and joint angle effects. This is mainly due to changes of the amplitude and total power under the spectrum. In BPSM, the total power is controlled by the scaling factor c, which is separated from the fractional-orders because of the power spectral separation of the fractional-orders. This unique characteristic allows the fractional-orders to only sense the asymptotic self-affine characteristics of the power spectrum.

Comparison of fractional-orders to MDN is also very interesting. Sensitivity of the MDN to joint angle has been also reported previously [MacIsaac *et al.*, 2001a]. Effects of the force on MDN

are not consistent in the available literature [Merletti and Parker, 2004]. In this study, MDN is not sensitive to force.

Although accurate for most MESs recorded during moderate contractions, for a few subjects whose MES power spectrum was close to flat in lower frequencies and/or estimated characteristic frequency was very small, BPSM was insufficient. This limitation might also be problematic during zero effort contractions when the power spectrum is not bi-phase. In such cases, it is not appropriate to use the BPSM and alternative approaches must be employed.

5.5. Conclusions

The revelation of the limitations of previous methods (i.e., Katz, box-counting, and $1/f^{\alpha}$) in this work is important given that they have been (and still are) the primary fractal analysis methods used in this area of research [Anmuth *et al.*, 1994; Chang *et al.*, 2000, 2004, 2007, Chen *et al.*, 2006; Talebinejad *et al.*, 2006a, 2006b]. These limitations motivated our work; introducing the BPSM, a novel power spectrum-based method for fractal analysis of MES, including an algorithm for the extraction of fractional-orders. This method provides a more sophisticated framework for fractal analysis of MESs and presents a bi-phase power-law which has a great potential for a variety of MES applications.

We evaluated BPSM in the context of force and joint angle and have shown how fractional-orders extracted by this method reflect changes in the MESs. The BPSM has demonstrated parameters capable of sensing force and joint angle effects separately. Simulation results [Talebinejad *et al.*, 2007] have been reaffirmed with experimental results presented in this chapter. This analysis method provides discriminatory information, which would be useful in

applications, such as classifying MESs (e.g., prosthetic control, or differentiating muscular diseases).

It was shown that high and low frequency indicators q and g are also insensitive to changes of the muscle fiber conduction velocity and spectral compression due to the muscle fatigue [Talebinejad *et al.*, 2007]. When the measured action potentials expand due to a low conduction velocity, their underlying distribution is not changed and is only shifted towards lower frequencies. The insensitivity of g and q is due to the homomorphism [Talebinejad *et al.*, 2007] of the bi-phase power-law which separates the effects of conduction velocity and spectral compression from the fractional-orders.

In terms of computational complexity, bi-phase power-law estimation is more time consuming compared to the $1/f$ approach and spectral moments. The required time greatly varies depending on each case (1 min to 20 min, for 15 to 25 s signals). It is possible to expedite the recursive procedure by manual setting of initial characteristic frequency for each case with trial and error.

Chapter 6

6. Long memory: Fatigue estimation using DFA

This chapter presents a novel multi-fractal DFA-based approach for fatigue estimation. This approach exploits the statistical self-similarity and long-range correlation of surface MESs at different time scales. This approach provides a fatigue index which outperforms the conventional MDN during cyclic and random contractions. As discussed in section 2.4.2, MDN is confounded by factors, such as force and joint angle.

The complex nature of the MES originating from multi-layered hierarchically structured (i.e., MU action potentials) and random (i.e., neural innervation) contributions suggest multi-scale characteristics; that is, when the MES is analyzed on different scales, different characteristics are exhibited [Gao *et al.*, 2007]. In chapter 5, a study was presented that also confirms that this signal shows some form of extended self-similarity that resembles multi-scale characteristics. Thus, one could analyze the MES on different scales and look for certain characteristics that are of interest for a specific application. In the case of fatigue estimation during dynamic contractions, it is of interest to look for scales in which the effects of varying force, muscle length (joint angle), and innervation zone are minimal, while the myoelectric manifestation of fatigue is more significant (i.e., an optimum scaling range for fatigue estimation).

In this chapter, we introduce a novel approach based on DFA with which it is possible to analyze the MES on a wide range of scales and identify the most appropriate time scales in which the myoelectric manifestation of fatigue is more significant compared to factors other than fatigue. We evaluate this approach with a human experimentation, in which participants perform static,

cyclic, and random contractions and compare the multi-scale fatigue index to conventional MDN.

6.1. Multi-fractal DFA

Multi-fractal DFA [Gao and Royshowdhury, 2000; Peng *et al.*, 1994] has been studied extensively for determining the long-range correlation and statistical self-similarity of random processes [Gao *et al.*, 2007; Chen *et al.*, 2002, 2005; Talkner and Weber, 2000] and was introduced earlier in section 3.4.

After applying the multi-fractal DFA to a time series and obtaining a power-law regime based on Eq.(3.20), one could compute the Hurst exponent by approximating the whole power-law; however, as shown in chapter 5, the MES does not follow a mono-phase power-law similar to $1/f$ processes, and it is ill-defined to approximate the MES's power-law with a single line; that is, there exists fractal-scaling-breaks in the power-law at which the slopes of the power-law changes. In this chapter we introduce a novel approach to exploit this very characteristic.

For fatigue estimation, MES recorded during an elongated contraction is segmented into several non-overlapping analysis windows, where the fatigue state is assumed to be constant in each window. For each analysis window, a fatigue index is estimated. Performance of the fatigue index could be assessed considering the ideal case for a fatigue estimator to have a mono-tonic decrease from its initial value to some final value which corresponds to the time instance in which the subject cannot continue the contraction anymore. Previous studies show that a simple linear regression is adequate for quantification of performance of fatigue indices [Merletti and Parker, 2004].

In our proposed approach the power-law is divided in to a series of localized truncated power-laws, presuming that the approximation with a single line is acceptable within small scaling ranges that imply the localized statistical characteristics show fractality. Then, a series of Hurst exponents are computed for each truncated power-law according to Eq.(3.20). It is expected that the myoelectric manifestation of fatigue affects the statistical characteristics of the MES, and thus the Hurst exponent of each truncated power-law. Among a series of Hurst exponents, corresponding to different local time scales, the optimum scaling range for fatigue estimation is considered as the one that shows the best linear regression with the progress of time. The proposed approach includes three main stages (presented schematically in Figure 6.1):

1. dividing a signal into a number of analysis windows and computation of a random walk for each window;

2. detrending, computation of a power-law using DFA, and computation of a series of local Hurst exponents; and

3. finding the optimum time scales for fatigue estimation in terms of linear regression.

6.2. Experimental methods

6.2.1. Data

The fatiguing MES data recorded from human subjects during static, cyclic and random contractions were used in this experiment (refer to section 4.3). Data were then divided into 4 s non-overlapping analysis windows (2^{12} = 4096 samples roughly corresponding a full arm extension or flexion at a rate of 32°/s); for each analysis window the level of fatigue was assumed to be constant.

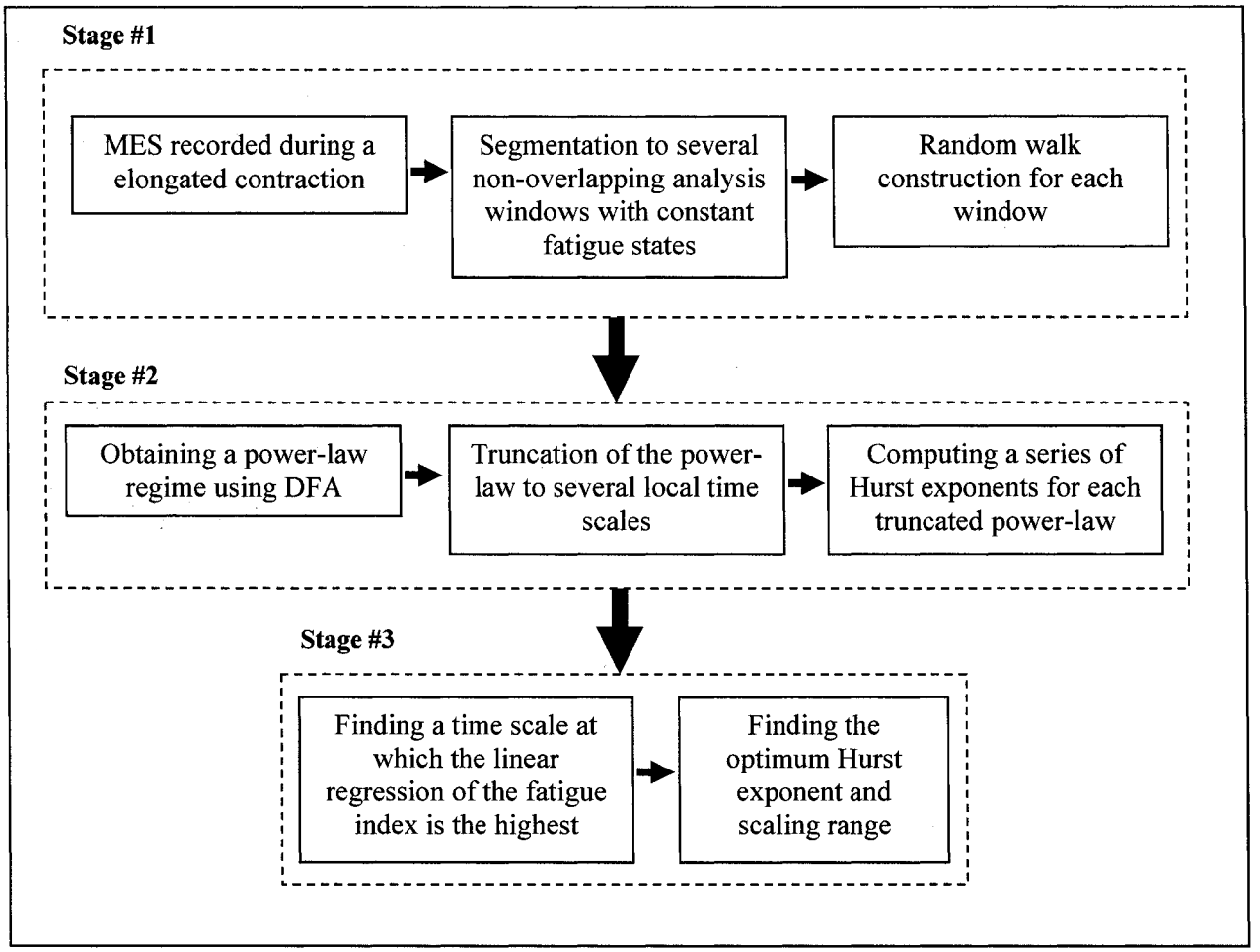

Figure 6.1: Block diagram illustration of the algorithm.

6.2.2. Analytic methods

Two different parameters were evaluated and compared: the optimum Hurst exponent for fatigue denoted as H, and the conventional MDN.

6.2.2.1. Optimum Hurst exponent

The optimum Hurst exponent was computed according to the algorithm described in section 6.1.1. The scale m (see Eq.(3.20)) was varied between 2^2 to 2^{12}, using increments of $2^{0.1}$. The power-law was obtained by considering Eq.(2) in a $\log_2$-$\log_2$ plot. The power-law regime was

then divided into 10 localized truncated power-laws (i.e., local time scales are $n < \log_2(m) < n+1$, $n = 2, 3, \ldots, 11$) and each truncated power-law was approximated by a linear regression using a standard least squares approach. Similarly, the power-law regime was then divided into 5 localized truncated power-laws (i.e., local time scales are $n < \log_2(m) < n+2$, $n = 2, 3, \ldots, 10$), and each truncated power-law was also approximated by a linear regression. The Hurst exponent was computed for each truncated power-law according to Eq.(3.20). This procedure was repeated for q values ranging between 2 to 3 with 0.1 steps.

For assessment of linear regression to identify the optimum Hurst exponent a linear regression coefficient was computed for each localized power-law as

$$r = \left| \frac{\sum_{i=1}^{N} (l_i - \bar{l})(i - \bar{i})}{\left[\sum_{i=1}^{N} (l_i - \bar{l})^2 \sum_{i=1}^{N} (i - \bar{i})^2 \right]^{1/2}} \right|, \qquad (6.1)$$

where

$$\bar{l} = \frac{1}{N} \sum_{i=1}^{N} l_i \text{ and } \bar{i} = \frac{1}{N} \sum_{i=1}^{N} i. \qquad (6.2)$$

The l_i denotes the Hurst exponent value of the lth local power-law at the ith analysis window. The local Hurst exponent with the highest linear regression coefficient was held as the optimum Hurst exponent corresponding to the optimum local scales.

6.2.2.2. Median frequency

The MDN was computed as the 50th percentile frequency from the estimated power spectrum for each 4 s analysis window. The power spectrum was estimated using the Welch's method

[Monson, 1996], which is a non-parametric method. The ergodicity and pseudo-stationary characteristics of MESs make them well suited for a time-slice averaging algorithm such as Welch's method compared to the periodogram which is not statistically consistent for estimating the power spectrum [Monson, 1996]. For averaging, a Hamming window with a temporal width of 1024 samples (1 s) was applied, with a 50 % window overlap.

6.2.2.3. Statistics and performance analysis

A generalized linear model repeated measures procedure was used to examine differences between the fatigue indices H, and MDN, as well as contraction conditions between all subjects. An ANOVA was used to evaluate differences between the fatigue indices and contraction conditions with threshold $\alpha_T = 0.05$. Test of Sphericity validates the assumption of sphericity ($s > 2$).

The performance of each fatigue index was assessed in terms of wellness of its linear regression similar to Eq.(6.1) and (6.2) as

$$r = \left| \frac{\sum_{i=1}^{N} (I_i - \bar{I})(i - \bar{i})}{\left[\sum_{i=1}^{N} (I_i - \bar{I})^2 \sum_{i=1}^{N} (i - \bar{i})^2 \right]^{1/2}} \right|, \qquad (6.3)$$

where

$$\bar{I} = \frac{1}{N} \sum_{i=1}^{N} I_i \text{ and } \bar{i} = \frac{1}{N} \sum_{i=1}^{N} i. \qquad (6.4)$$

The I_i denotes the fatigue index value at the ith analysis window.

6.3. Results

6.3.1. Evaluation of power-law regime

The power-law regime, shown in Figure 6.2, clearly shows that the MES exhibits both mono- and multi-fractality on different time scales; that is, the Hurst exponent is not a constant function of moment-order in lower scales before $m = 6$, which is consistent with multi-fractals, but it is almost a constant function of moment-order at higher scales after $m = 6$, which is consistent with mono-fractals as previously covered in section 3.3. This explains the naiveness of using a single fractal dimension to characterize the MES. Figure 6.2, also illustrates why using a single mono-phase power-law in the form of a $1/f$ processes is ill-defined for MESs; it is also noticeable that the power-law exhibits an extended form of self-similarity similar to the bi-phase power-law presented in chapter 5. Meanwhile, approximating the truncated power-laws with a single line in each segment is well-justified and representative (least squares linear regression error was lower than 10^{-20} in all cases). The saturation of the power-law for moment-orders higher than $q = 3$ around the power-law justifies limiting the moment-orders to the range 2 to 3 to reduce the computational complexity of this approach.

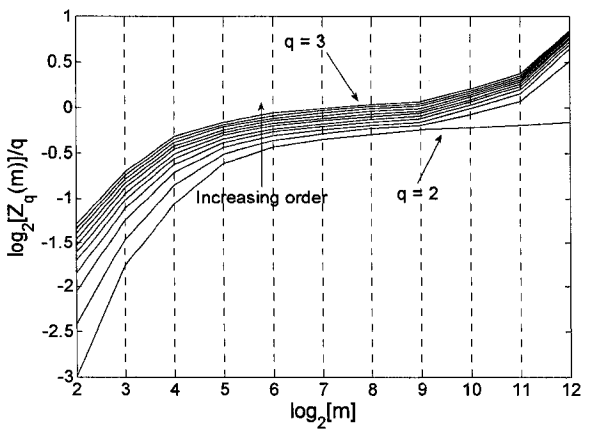

Figure 6.2: Power-law regime obtained for a typical segment.

Figure 6.3 shows typical power-law regimes of unfatigued (first 4 s window of a contraction) and fatigued (last 4 s window of a contraction) states. The power-law experiences two main changes with the progress of fatigue: 1) an increasing power-law towards larger values at all scales, and 2) an increase of the Hurst exponent at lower scales. These two changes will be discussed shortly in section 6.4.

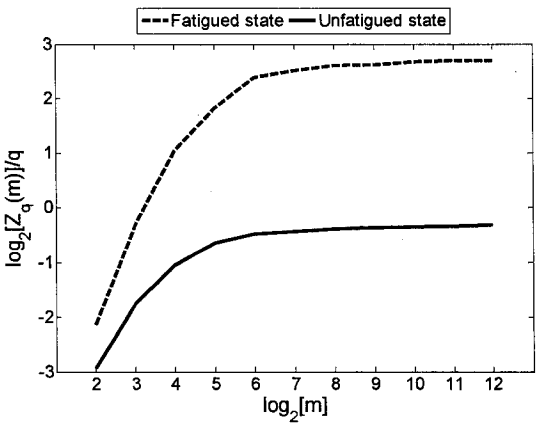

Figure 6.3: Comparison of power-law from unfatigued and fatigued states.

Figure 6.4 shows the corresponding Hurst exponents for 10 consecutive truncated power-laws at different scaling ranges obtained with $q = 2$. It is noticeable that the difference between the Hurst exponents is larger at smaller time scales.

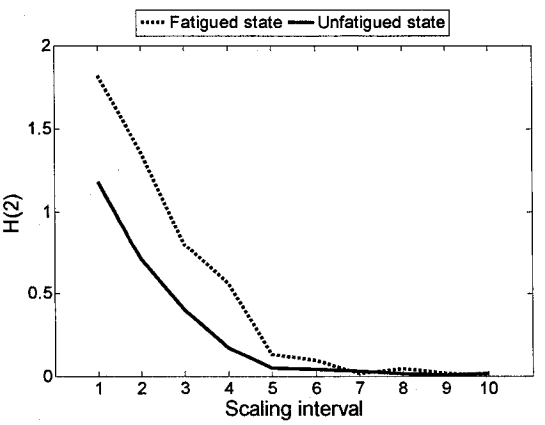

Figure 6.4: Hurst exponents for 10 consecutive scaling ranges in unfatigued and fatigued states.

6.3.2. Comparison of fatigue indices

Figure 6.5, shows the normalized MDN (MDN_N) and normalized H (H_N), for all three tests for one subject. After normalization the dynamic range of the parameters are restricted to 0 to 1 for better visualization and comparison.

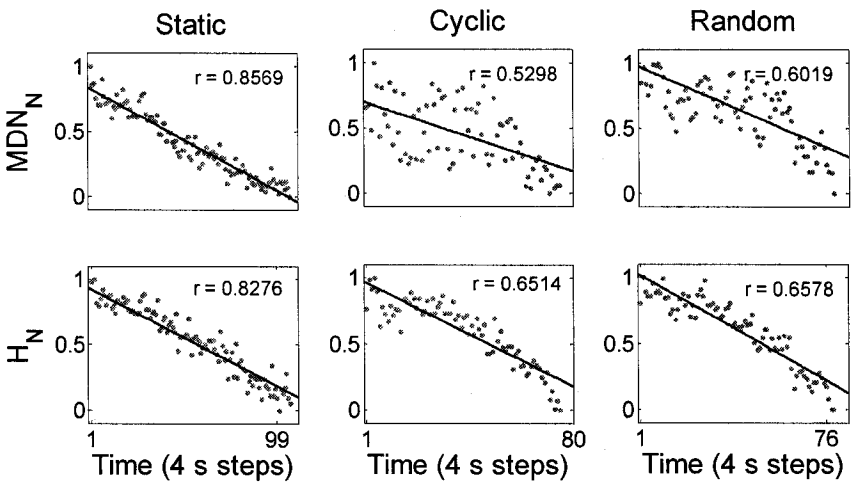

Figure 6.5: Fatigue indices normalized for better visualization and comparison from subject 9.

Figure 6.6, depicts the averaged linear regression coefficients across all subjects for all three tests and the inter-subject variability in form of error bars.

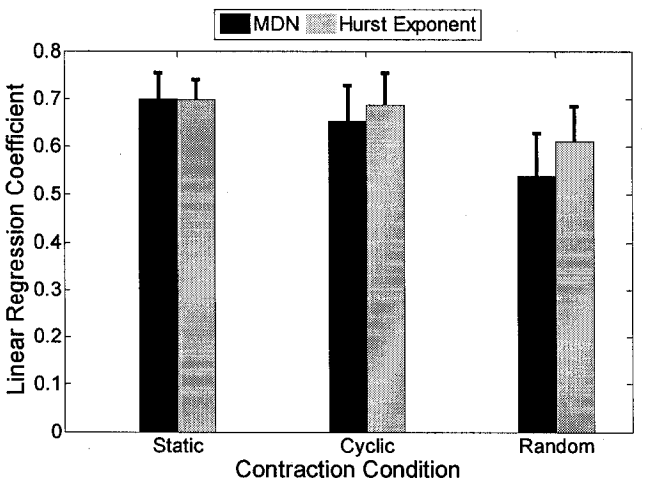

Figure 6.6: Comparison of H and MDN during static, cyclic and random contractions.

Table 1, shows the linear regression coefficients of both parameters for all subjects. According to the results of repeated measures procedure H and MDN are significantly different ($p < 0.001$) in all three contractions. The contraction condition also significantly affects the fatigue indices ($p < 0.001$). Table 1 lists the linear regression coefficients for all 10 subjects. The number of cases where H had the highest linear regression coefficient are 2/10 for static contractions, 10/10 for cyclic contractions, 10/10 for random contractions.

Table 6.1: Linear regression coefficients for all 10 subjects.

Subject	Parameter	Static	Cyclic	Random
S1	MDN	0.6367	0.6187	0.5159
	H	0.6998	0.6525	0.6164
S2	MDN	0.7145	0.7596	0.5839
	H	0.7098	0.7611	0.6212
S3	MDN	0.6129	0.6878	0.4521
	H	0.6118	0.7017	0.5159
S4	MDN	0.6345	0.4997	0.4321
	H	0.6278	0.5519	0.5497
S5	MDN	0.7711	0.7862	0.6428
	H	0.7018	0.8023	0.6712
S6	MDN	0.6310	0.6834	0.6202
	H	0.6947	0.6998	0.7048
S7	MDN	0.7853	0.6812	0.5319
	H	0.7299	0.7119	0.5924
S8	MDN	0.6583	0.6023	0.5932
	H	0.6489	0.6324	0.6495
S9	MDN	0.8569	0.5298	0.6019
	H	0.8276	0.6514	0.6578
S10	MDN	0.6913	0.6852	0.4131
	H	0.6898	0.7002	0.5388

6.4. Discussion

The MDN's performance in tracking fatigue is better than the optimum Hurst exponent during static contractions and outperforms it in terms of linear regression in 80% of cases. This could be explained by the sensitivity of MDN to statistical changes of MES in all time scales which makes it a useful scale-independent indicator. The optimum Hurst exponent is scale-dependent and is isolated to changes of certain time scales and is exposed to a limited amount of information.

During cyclic and random contractions when the MDN is affected by factors other than fatigue, isolation of the Hurst exponent to certain time scales is advantageous. As shown in the results, the optimum Hurst exponent has a greater linear regression compared to MDN for dynamic contractions. This could be explained as the MDN reflects global changes of MES which includes changes of force, muscle length (joint angle), and innervation zone, but it is possible to look for time scales in which all other factors are minimum but the myoelectric manifestation of fatigue and obtain a more accurate fatigue index in terms of its linear regression. Intuitively, it is expected that different time scales are affected with different varying factors during dynamic contractions with different levels of significance and the presented approach which identifies the optimum time scales exploits this feature and outperforms the MDN.

Changes of the Hurst exponent due to the myoelectric manifestation of fatigue could be attributed to expanded MU action potentials in time which results in an increased long-range correlation along the MES at small time scales as well as formation of trivial correlations which could be caused by an increased level of MU synchrony [Farina *et al.*, 2002]; thus, the Hurst exponent is affected by both peripheral and central myoelectric manifestation of fatigue which could be also a contribution that results in better performance of the Hurst exponent compared to MDN which is solely reflecting the changes of muscle conduction velocity during dynamic contractions. The power-law regime also experiences an increase which does not affect the Hurst exponent due to its homomorphic separation similar to factional-order(s) of a power-law presented in chapters 3 and 5. This increase is consistent with dependency of the power-law regime value to the amplitude of the signal and that the amplitude of the signal is also increasing with the progress of fatigue. Increased amplitude could be attributed to an increased number of firing MUs and/or their discharge rate [Merletti and Parker, 2004] which affects the power-law

value at all scales. Our experiments using simulated MESs also confirm that an increment in recruitment followed by increased signal amplitude also raises the power-law value at all scales and does not affect the Hurst exponent. This implies that the Hurst exponent is insensitive to the changes in recruitment strategy and any changes that have a constant effect on all time scales similar to magnification of the whole signal which yields greater amplitude. Thus, it is most remarkable that the changes of the Hurst exponent could be mainly attributed to the changes of persistence among the firing MUs and the correlation between the discharges.

Moreover, it was observed that the optimum Hurst exponent is commonly within the smaller time scales (i.e., small m values). In smaller time scales, the Hurst exponent is primarily affected by the correlation of adjacent samples; it is expected that adjacent samples reflect local trends of force, muscle length (joint angle), and innervation zone location; that is, adjacent samples are likely to be recorded when the force, muscle length (joint angle), and distance between the electrode and innervation zone are pretty much constant and form a local trend. Better performance of the optimum Hurst exponent in fatigue tracking compared to MDN during dynamic contractions could be also attributed to the removal of local trends from the constructed random walk.

Conventionally the Hurst exponent is defined to be positive and smaller than 1; however, after the random walk construction the DFA is expected to estimate a positive Hurst exponent smaller than 2 [Gao *et al.*, 2007]. The power-law regime also suggests that the MES shows persistence at lower scales (i.e., higher Hurst exponents) and resembles coloured noise. At the larger time scales the MES resembles a highly random white noise. These characteristics are very important in interpretation of the power-law; at smaller scales the degree of randomness is lower and the MES resembles a random fractal; at larger time scales the Hurst exponent saturates around zero

and the DFA is not capable of distinguishing the MES from white noise. It is also possible to show that in most cases when the scale-dependent Lyapunov exponents are positive, at larger scales MES resembles a chaotic motion which is also consistent with inadequacy of the Hurst exponent at larger time scales.

6.5. Conclusions

A novel approach for extraction of multi-scale parameters from MES with an application for fatigue estimation was presented. The optimum Hurst exponent increases with the progress of fatigue, which suggests the MES becomes statistically more persistent which could be explained by the time expansion of MU action potentials due to a lowered muscle fiber conduction velocity and an increased MU firing synchrony. The optimum Hurst exponents also show a greater degree of linear regression with the progress of fatigue. It can provide a robust method of tracking muscular fatigue, and is more accurate compared to MDN during cyclic and random contractions.

In terms of computational complexity, the DFA is also faster than Welch's method for power spectrum estimation. In this work, power-law estimation for each segment required only 1.53 s, for 4 s signals, while power spectrum estimation required over 50 s in most cases.

Chapter 7

7. Multi-fractality: MCM for discerning neuropathic MESs

The MES changes characteristically with neuromuscular disorders as discussed previously in section 2.5.3. For example, neuropathic conditions (e.g., nerve injury) are associated with a reduced number of active MUs and reorganization of the muscle fibers to form larger MUs [Stalberg and Falck, 1997]. This phenomenon affects the frequency content of the MES and can be perceived in severe cases during zero effort contractions by visual inspection and/or listening to the signal via a loudspeaker [Okajima *et al.*, 2000]. During voluntary contractions, the number of the contributing MUs and their firing rate increases, and the MES becomes very complex; in such cases, simplistic manual inspection is not very informative and a quantitative approach for discerning pathological MESs is of interest.

In chapters 5 and 6, it was demonstrated that the MES shows some form of extended self-similarity that resembles multi-scale characteristics [Talebinejad *et al.*, 2008e]. Thus, one could analyze the MES on different scales and look for certain characteristics that are of interest for a specific application.

In this chapter, we introduce a new method for multi-scale analysis of MESs based on an interesting fractal process known as, MCM [Gao *et al.*, 2007] previously covered in section 3.4. We evaluate MCM with simulated needle MESs and present an experiment for discrimination of normal and neuropathic MESs. MCM modeling is also compared to the conventional NT in the presence of additive white Gaussian noise which is the typical noise in clinical settings and/or interference caused by the cross-talk of other nearby muscles.

7.1. Experimental methods

7.1.1. MCM modeling

MCM modeling in this chapter is similar to section 3.4. In practice, the mean of the MES is removed, so the weights introduced in section 3.4, are oscillatory between negative and positive values; therefore, the sum of the weights according to Eq.(3.21) may be zero or negative for odd moment-orders. In both cases the signal would not show a power-law regime. A simple solution is to use the absolute value of the signal to make sure all samples are positive, which is what was done in this work.

7.1.2. Number of turns

The NT was estimated as the number of turn points that are greater than 100 μv [Finsterer, 2001]. We identify the turn points by identifying all the samples that are higher than 100 μv in the vicinity of a local maximum or minimum and save their time indexes. We then compute the derivative of the time indexes which could be divided into two categories, 1) index derivative for time indexes that correspond to the turn points and the samples in their vicinity that are greater than 100 μv, is equal to 1, and 2) at instances when the turn points and the samples in their vicinity are smaller than 100 μv the index derivative is greater than 1, this is only reflected once a time for all the samples smaller than 100 μv between two valid turn points. Number of times the derivative of indexes are higher than 1 could be used to estimate the NT.

7.1.3. Simulation of needle MESs

The data described in section 4.2, which consisted of 100 sets of normal and 100 sets of neuropathic signals simulated at 10 % of the maximum voluntary contraction (MVC) was used in this work. Each signal was 1.024 s long with sampling rate of 16 kHz (2^{14} samples per signal).

7.1.4. Classification

For classification a standard fuzzy *k*-means procedure [Duda *et al.*, 2001] was performed to classify the signals into two categories, normal and neuropathic.

7.2. Results and discussions

7.2.1. Appropriate scales for analysis

Figure 7.1, shows the power-law regimes obtained after the construction of the MCM model for two sets of simulated MESs, one normal and one neuropathic.

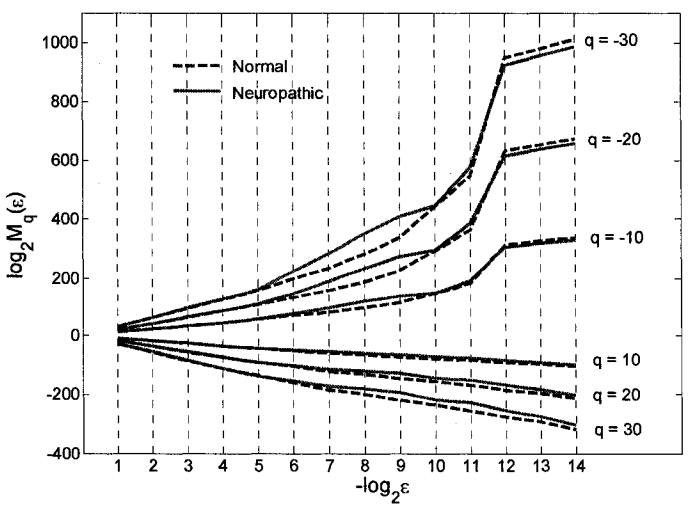

Figure 7.1: Power-law regimes obtained using different moment orders.

The $\log_2 M_q(\varepsilon)$, characterizes individual samples at stage $N = 14$, which is the lowest possible scale for the signals containing 2^{14} samples. Fractal analysis is not meaningful at stage 14 because individual spikes and the noise between them are analyzed. To exploit the statistical self-similarity and long-range dependency along the signal, more samples denoting larger scales need to be analyzed. As the stages progress towards the stage 1, the scale becomes larger. Stage 10 corresponds to 2^4 samples or 0.97 ms (16 Hz), which is smaller than the maximum firing rate (i.e., inter-spike interval) of the simulated signals (i.e., 20 Hz). Thus, fractal analysis is meaningful starting at stage 9, when the scale is definitely larger than average inter-spike interval between the samples (i.e., 32 Hz). Indeed the power-law regimes, shown in Figure 7.1, are fairly linear from stage 9 to stage 1.

7.2.2. Appropriate scales for discrimination

Figure 7.2 shows the generalized dimension spectrum computed for both power-laws that were shown in Figure 7.1.

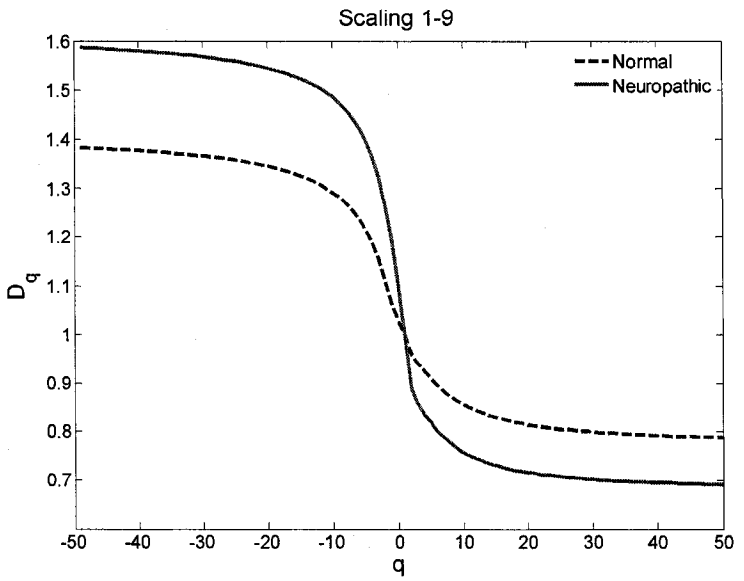

Figure 7.2: Spectrum of generalized dimension spectrum computed over a wide range of moment orders between scales 1 to 9.

It is also noticeable in Figure 7.1 that the differences are larger between stages 5 to 9 compared to stages 1 to 5. This could be explained by the very large scales at stages 1 to 5, which result in blurred information that is not very informative to discriminate between both signals. Figure 7.3, shows restricted generalized dimension spectrums between stages 1 to 5 and 5 to 9. The restricted generalized dimension spectrum computed between stages 5 to 9, has a much higher dynamic range when compared to the restricted generalized dimension spectrum computed between stages 1 to 5; the dynamic range is also higher than the generalized dimension spectrums computed over stages 1 to 9 (Figure 7.2). Thus, there exists a fractal-scaling break around stage 5, which can also be seen in Figure 7.1 as a change of slopes. In this work, we acknowledge this fractal-scaling-break and compute the generalized dimension spectrum between stages 5 to 9 to exploit the maximum dynamic range in our classification experiments.

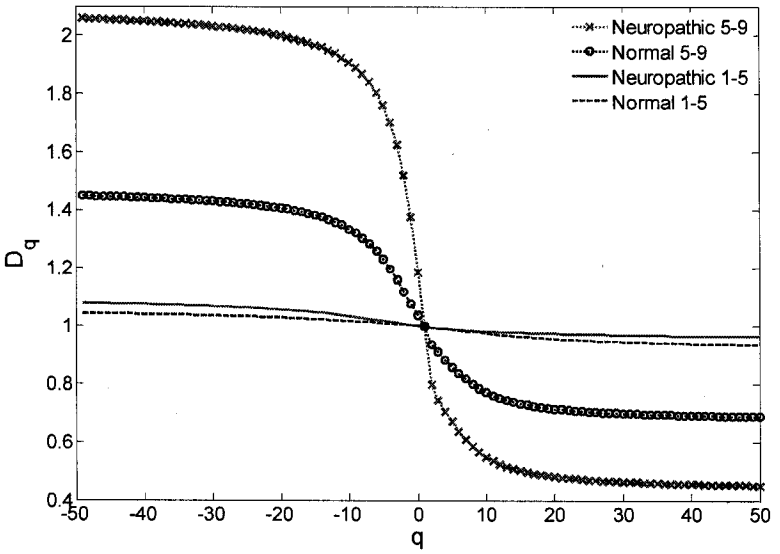

Figure 7.3: Restricted generalized dimension spectrums computed over a wide range of moment orders between scales 1 to 5, and 5 to 9.

7.2.3. Classification results

Figure 7.4 compares histograms of the D_{-50} to the NT when signals are clean and when signals are distorted with additive white Gaussian noise with a noise power (NP) of 10 dB. Note the average power of simulated signals is 17 dB. The vertical axes of the histograms represent the number of samples in each bin. The histograms with more overlap between the normal and neuropathic samples lead to a lower classification accuracy. The classification accuracy (CA), using the NT, decreases in the presence of additive noise. The classification accuracy using the D_{-50} also decreases in the presence of additive noise; however, as shown in Figure 7.5, D_{-50} is more robust compared to NT.

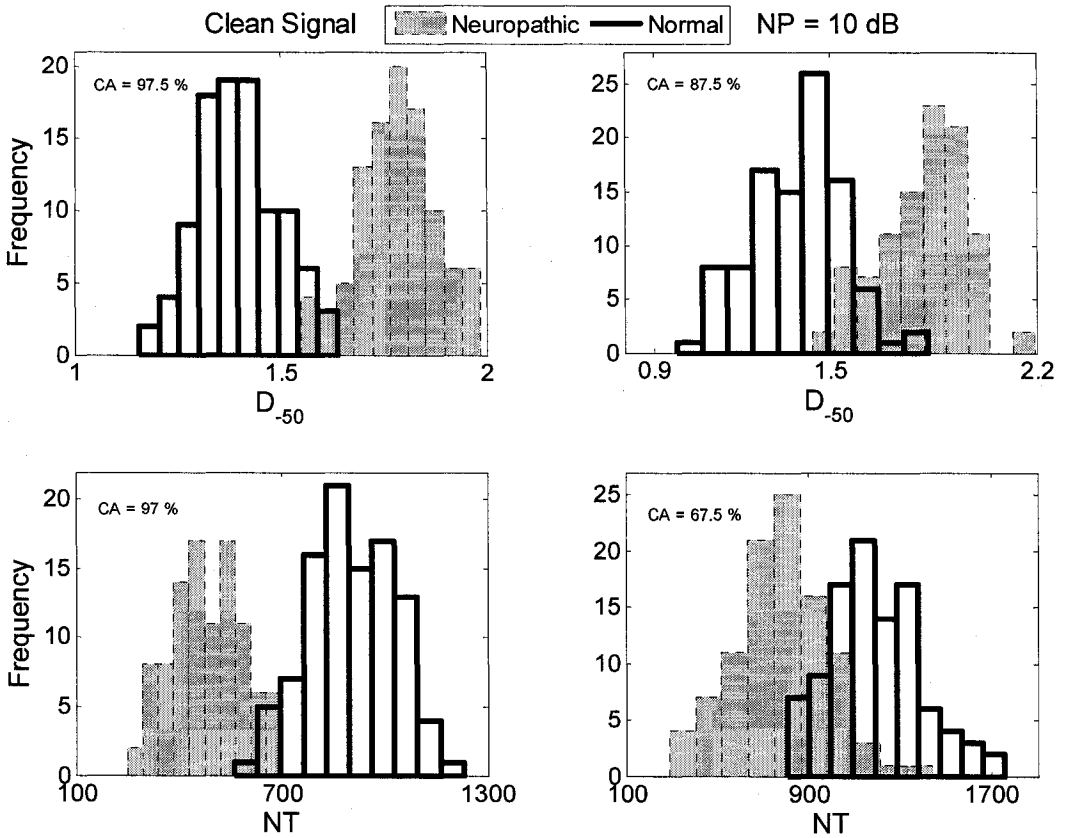

Figure 7.4: Histogram of D_{-50} and NT. When the noise level is increased the D_{-50} outperforms the NT.

In the presence of additive white Gaussian noise, the NT will dramatically change which results in a lowered classification accuracy; however, summation and combination of samples within the MCM model has suppressing effects on noise. The D_{-50} outperforms the NT for classification especially in the presence of additive white Gaussian noise.

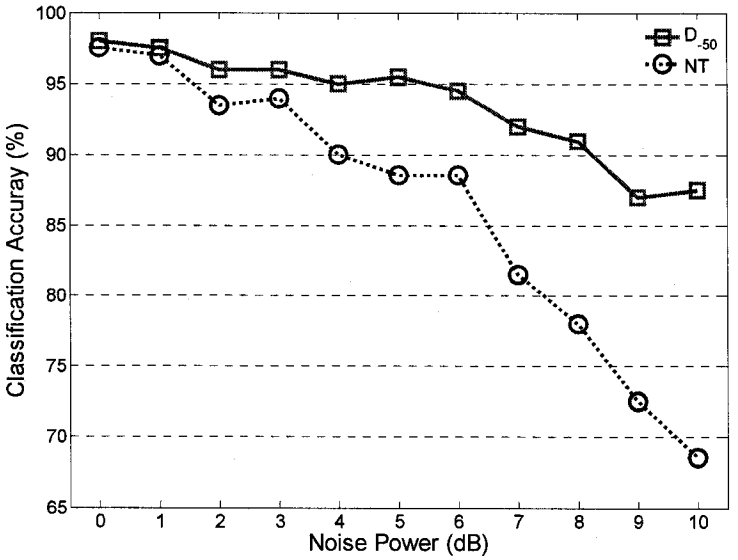

Figure 7.5: Comparison of classification accuracy using D_{-50} and NT at different noise levels.

7.3. Conclusions

In this chapter, we have presented a new method for multi-scale analysis of MESs using the MCM model. Results show that we can analyze the MES on a wide range of scales and that different scales are more appropriate for particular applications. A method for the discrimination of normal and neuropathic MESs was presented, along with the appropriate scale ranges for this analysis.

It was demonstrated that the generalized dimension spectrum is robust to additive white Gaussian noise compared to the conventional NT; the MCM modeling suppresses the noise by summation and combination of the samples. Results show this new method provides a reliable measure for quantitative analysis of MESs.

In terms of computational complexity, this approach is directly applicable to the signal and requires 0.98 s for 1.024 s signals and is comparable to the number of turns which requires 0.96 s.

Future research will validate these findings with human experimental data. It would also be interesting to analyze the power spectrum of the MCM model at different levels to see whether a scale-dependent power spectrum representation is useful to complement the scale-independent power spectrum.

Chapter 8

8. Chaos: Fatigue estimation using LZ complexity measure

In section 3.5, we have shown the MESs are not fully random or fully chaotic. It seems well-justified to exploit the deterministic complexity that can occur under highly non-linear deterministic and chaotic settings. As well, one can look for parameters that reflect the myoelectric manifestation of fatigue to complement conventional measures. In this chapter we present a LZ complexity measure for analysis of MESs and fatigue estimation.

The LZ complexity measure and its variants [Lempel and Ziv, 1976] have been widely used to identify and quantify irregularity and deterministic complexity in signals [Aboy *et al.*, 2006; Hu *et al.*, 2006; Nagarajan, 2002; Zhang *et al.*, 2001]. In general, LZ complexity measures the rate of generation and occurrences of distinct deterministic patterns along a signal, as well as synchronization among the samples [Gao *et al.*, 2007]. It is also related to the entropy rate of the underlying source responsible for a time series [Gao *et al.*, 2007].

It is expected that when the muscle CV decreases with fatigue and the MES frequency content is shifted towards lower frequencies, the number of distinct patterns and the rate of their occurrence also change in the MES; moreover, it is expected that a greater degree of synchronization among the firing MUs occurs [Merletti and Parker, 2004]. The most remarkable characteristic of the LZ measure is its insensitivity to the actual patterns, so it is reflecting primarily the rate of their creation and synchronization. This characteristic makes it a unique analysis technique for MESs. If we consider the confounding effects during dynamic contractions affect mainly the MES patterns, while muscle fatigue affects primarily the rate of creation, occurrence and

synchronization of the patterns, one would expect a more accurate muscle fatigue index based on the LZ complexity measure relative to conventional frequency parameters.

In this Chapter we present a LZ measure, which is enhanced to a multi-level symbolizing algorithm to avoid the effects of noise between the MUAPs in the MES. Moreover, we evaluate the LZ measure for fatigue monitoring with a human experiment and compare it to the conventional MDN during static, cyclic and random contractions.

8.1. Experimental methods

8.1.1. LZ complexity measure

To compute the LZ measure, a MES numerical sequence must first be transformed into a symbolic sequence. The use of symbolic techniques to map a time series into a sequence retaining its dynamics has been quite popular [Abasolo *et al.*, 2006; Wu and Xu, 1991]. Conventionally, the signal $x(i)$ is converted into a binary sequence $s(i)$ by comparing the signal with a threshold value ξ_T [Zhang *et al.*, 2001]. That is, whenever the signal $x(i)$ is smaller than ξ_T, one maps the signal to 0; otherwise, to 1. This can be expressed mathematically as,

$$s(i) = \begin{cases} 0, & if \quad x(i) < \xi_T \\ 1, & otherwise \end{cases} . \qquad (8.1)$$

The symbolic sequence P_s is formed as,

$$P_s = s(1), s(2), ..., s(N) . \qquad (8.2)$$

This sequence can be parsed to obtain distinct patterns. Several methods have been proposed to perform parsing. In this work, we use the parsing method proposed by the original authors of LZ

complexity [Lempel and Ziv, 1976], which is the most widely used method. This parsing method is described below.

Let the symbolic sequence P_s be divided into substrings P_s (i,j), which start at position i and end at position j; that is, when $i \leq j$, P_s (i,j) = s(i)...s(j) and, when $i > j$, P_s (i,j) = ø, which is the null set. Let $V(P_s)$ denote the power set of substrings in the sequence P_s excluding the null set (e.g., if P_s = 001, then $V(P_s)$ = {0, 1, 00, 01, 001}). The parsing procedure involves a left-to-right scan of the sequence P_s. A substring $P_s(i,j)$ is compared to $V(P_S(1,j\text{-}1))$. If P_s (i,j) is present in $V(P_s(1, j\text{-}1))$, then P_s (i,j) and $V(P_s$ $(1,j\text{-}1))$ are updated to P_s $(i,j\text{+}1)$ and $V(P_s(1,j))$, respectively, and the process repeats. If the substring is not present, then $s(j)$ is marked to indicate the end of a new component, and P_s (i,j) and $V(P_s$ $(1,j\text{-}1))$ are updated to P_s $(j\text{+}1,j\text{+}1)$ and $V(P_s$ $(1,j))$, respectively. The process continues until $j = N$, where the N is the length of the symbolic sequence P_s. For example, the sequence 1011010 would be parsed as 1.0.11.010., where the period is used to indicate the end of a pattern. Now let $c(N)$ denote the number of distinct patterns after parsing of the source sequence. In the example, the number of distinct patterns is $c(N)$ = 4. Lempel and Ziv have shown that the total number of subsequences present in P_s, denoted as $T(N)$, has an upper bound in this form

$$T(N) \leq c(N)[\log_\alpha \{c(N)\} + 1], \qquad (8.3)$$

where α is the number of symbols present in the sequence (in this binary symbolizing procedure $\alpha = 2$). The LZ complexity measure is a normalized version of the upper bound defined as,

$$LZ = c(N)[\log_\alpha \{c(N)\} + 1]/N . \qquad (8.4)$$

It is possible to transform the signal $x(i)$ into more than two symbols; however, previous studies have only examined the binary conversion to estimate the LZ complexity in biomedical signals [Wu and Xu, 1991; Xu *et al.*, 1997]. In this work, we examine a multi-level symbolizing approach.

8.1.2. Multi-level symbolizing approach

When estimating the LZ complexity of MES, the conventional binary symbolizing procedure might be affected by a false sense of complexity. This is due to the presence of low amplitude noise between the MUAPs in the MES. The noise will influence the number of distinct patterns greatly, even though the noise is irrelevant to the actual myoelectric information in the MES. To mitigate the effects of noise, we propose a multi-level symbolizing procedure. In our proposed approach, we symbolize the MES with three different levels: 1) positive portion of an individual or superimposed action potential, 2) signal content with low amplitude containing the noise between the MUAPs, and 3) negative portion of an individual or superimposed action potential. We perform a *k*-means clustering procedure with constrained centroid positions [Duda *et al.*, 2001] to symbolize the raw MES to a ternary symbol sequence. With this procedure, Eq.(8.1) is extended to

$$s(i) = \begin{cases} 1 \ if \leftarrow x(i) \in cluster\#1 \\ 0 \ if \leftarrow x(i) \in cluster\#2 \\ -1 \ if \leftarrow x(i) \in cluster\#3 \end{cases}. \qquad (8.5)$$

The centroid of the first category corresponds to the level 1 symbols; the *k*-means clustering procedure initializes the position of the first centroid as the maximum value of the signal. The centroid of the second category corresponds to the level 2 symbols; the *k*-means clustering

procedure initializes the position of the second centroid as the mean signal value, which is zero after the removal of the mean. The centroid of the third category corresponds to the level 3 symbols; the *k*-means clustering procedure initializes the position of the third centroid as the minimum value of the signal.

Figure 8.1 shows an example of both binary (2 level) and ternary (3 level) symbolizing procedures applied to a MES segment. It is clear that the rate of symbol changes is higher in the binary symbol sequence than ternary symbol sequence. Inclusion of the third symbol enables the symbolizing procedure to account for low amplitude noise between MUAPs.

The Lempel and Ziv parsing procedure described in section 8.2.1 could be generalized to more than 2 symbols. In this work, we employ this parsing procedure with the proposed multi-level symbolizing approach.

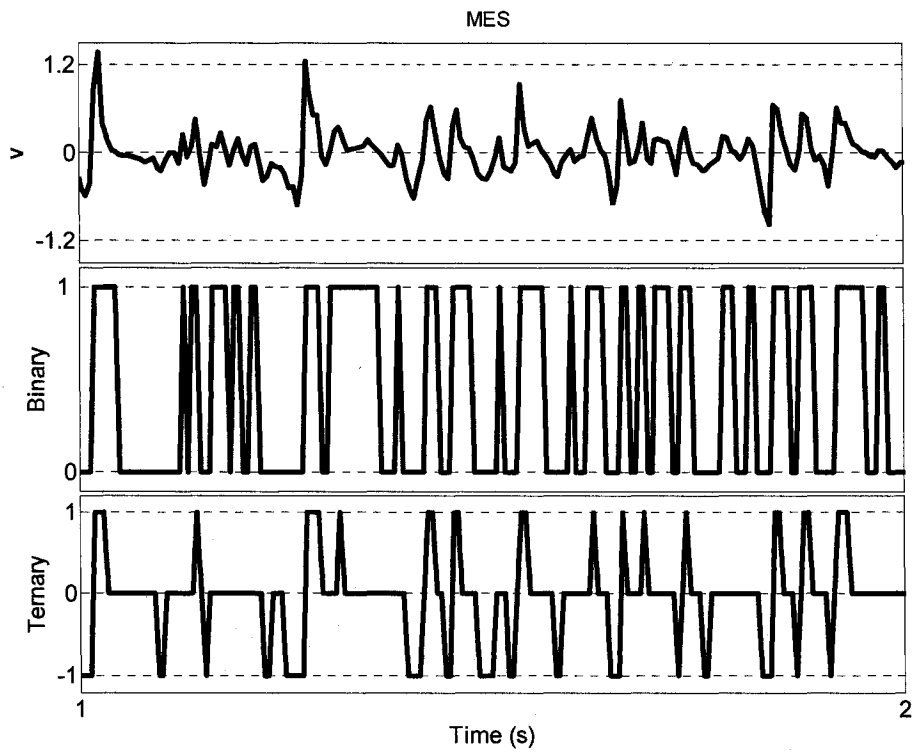

Figure 8.1: An example of binary and ternary symbolized signals.

8.1.3. Data

The fatiguing data recorded during static, cyclic and random contractions were used in this experiment (refer to section 4.3). Pre-processing was similar to section 6.2.1. Data were then divided into 5 s non-overlapping analysis windows (roughly corresponding a full arm extension or flexion at rate 32°/s); for each analysis window the level of fatigue was assumed to be constant.

8.2. Analytic methods

Three different MES parameters were evaluated and compared: 1) the LZ measure obtained by the binary symbolizing procedure, 2) the LZ measure obtained by the ternary symbolizing procedure, and 3) the conventional MDN. The binary LZ measure, denoted as LZ_2, was estimated by symbolizing the raw 5 s MES analysis windows with a single threshold that was set to zero, along with the described parsing algorithm in section 8.2.1. The ternary LZ measure, denoted as LZ_3, was estimated by symbolizing the raw 5 s MES analysis windows using the *k*-means procedure described in section 8.2.2, along with the described parsing algorithm in section 8.2.1. The MDN was computed as the 50th percentile frequency from the estimated power spectrum for each 5 s analysis window. The power spectrum was estimated using Welch's non-parametric method [Monson, 1996], with a 1024 sample (1 s) Hamming window and 50 % window overlap.

8.2.1. Statistics and performance analysis

A generalized linear model repeated measures procedure was used to examine differences between the fatigue indices LZ_2, LZ_3, and MDN, as well as contraction conditions between all

subjects. An ANOVA was used to evaluate differences between the fatigue indices and contraction conditions.

Performance of each fatigue index (i.e., LZ_2, LZ_3, and MDN) was assessed in terms its linear regression, assuming an ideal case is a linear monotonic decrease from the beginning of the contraction until complete exhaustion. In other words, after approximating the evolution of indices with a linear regression, a linear regression coefficient was defined in this form

$$r = \left| \frac{\sum_{i=1}^{N_t} (I_i - \bar{I})(t_i - \bar{t})}{\left[\sum_{i=1}^{N_t} (I_i - \bar{I})^2 \sum_{i=1}^{N_t} (t_i - \bar{t})^2 \right]^{1/2}} \right|, \qquad (8.6)$$

where

$$\bar{I} = \frac{1}{N_t} \sum_{i=1}^{N_t} I_i \text{ and } \bar{t} = \frac{1}{N_t} \sum_{i=1}^{N_t} t_i \,. \qquad (8.7)$$

I_i denotes the fatigue index value at the analysis window number t_i and N_t is the total number of analysis windows.

8.3. Results

8.3.1 Comparison of fatigue indices

Figure 8.2, shows the normalized fatigue indices MDN, LZ_2, and LZ_3 for all three tests for one subject. The increased linear regression can be seen visually as a lower variance in the data about the linear regression line. Figure 8.3, depicts the average linear regression coefficients across all subjects for all three tests and the inter-subject variability in the form of error bars.

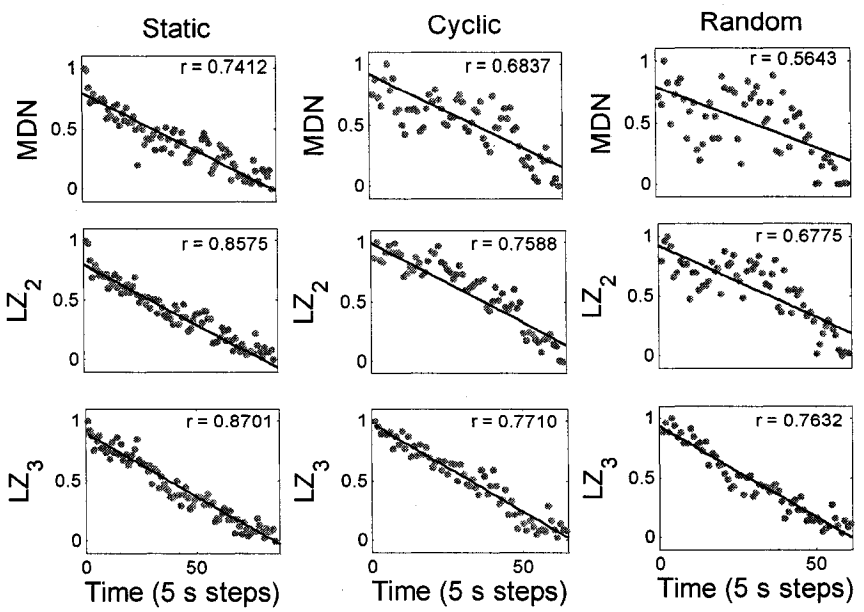

Figure 8.2: Fatigue indices normalized for better visualization and comparison from subject 2.

According to the results of repeated measures procedure MDN, LZ_2, and LZ_3, are significantly different ($p < 0.001$). The contraction condition also significantly affects the fatigue indices MDN, LZ_2, and LZ_3 ($p < 0.001$).

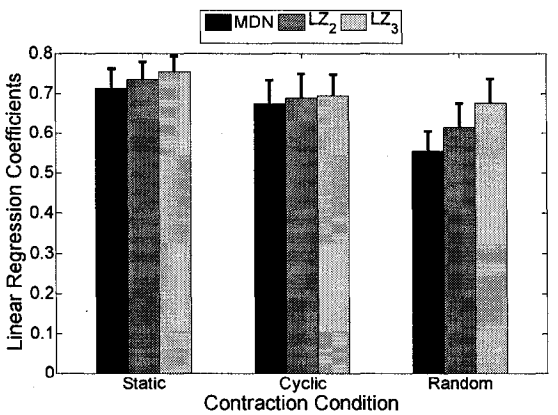

Figure 8.3: Comparison of MDN, LZ_2 and LZ_3 during static, cyclic and random contractions.

Table 8.1, lists the linear regression coefficients for all 10 subjects. The number of cases where LZ_3 had the highest linear regression coefficient are, 8/10 for static contractions, 8/10 for cyclic

contractions, 9/10 for random contractions. The number of cases where LZ_2 had a higher linear regression coefficient compared to MDN are, 7/10 for static contractions, 7/10 for cyclic contractions, 9/10 for random contractions. The LZ_2 was higher than LZ_3 only in one case during cyclic contractions.

Table 8.1: Linear regression coefficients for all 10 subjects.

Subject	Parameter	Static	Cyclic	Random
S1	MDN	0.6917	0.6159	0.6391
	LZ_2	0.6913	0.6230	0.5627
	LZ_3	0.7312	0.6411	0.5784
S2	MDN	0.7412	0.6837	0.5643
	LZ_2	0.8575	0.7588	0.6775
	LZ_3	0.8701	0.7710	0.7632
S3	MDN	0.7079	0.6613	0.5078
	LZ_2	0.7261	0.6508	0.7085
	LZ_3	0.7613	0.6811	0.7289
S4	MDN	0.6411	0.6223	0.5239
	LZ_2	0.7136	0.6477	0.6183
	LZ_3	0.7515	0.6642	0.6393
S5	MDN	0.6543	0.6117	0.5867
	LZ_2	0.7373	0.6523	0.6005
	LZ_3	0.7610	0.6731	0.6231
S6	MDN	0.8210	0.7592	0.6278
	LZ_2	0.7138	0.8034	0.6790
	LZ_3	0.7521	0.7702	0.7211
S7	MDN	0.7303	0.7899	0.5183
	LZ_2	0.7293	0.6911	0.6071
	LZ_3	0.7523	0.7103	0.7523
S8	MDN	0.7185	0.6792	0.5629
	LZ_2	0.7211	0.6276	0.6168
	LZ_3	0.7513	0.6721	0.7132
S9	MDN	0.7128	0.6642	0.5347
	LZ_2	0.7213	0.7281	0.5423
	LZ_3	0.7520	0.7315	0.7121
S10	MDN	0.7037	0.6509	0.4814
	LZ_2	0.7235	0.7017	0.5391
	LZ_3	0.7587	0.7109	0.6329

8.4. Discussion

The LZ measure outperforms the MDN in terms of linear regression. This could be explained by the insensitivity of the LZ complexity measure to the actual deterministic patterns, which changes with contractile force and/or muscle length, and its primary sensitivity to the rate of creation of patterns, which is influenced greatly by the muscle CV. Meanwhile the MDN is influenced greatly by the changes of frequency content due to a muscle movement (i.e., changes in force and joint angle).

The LZ_3 outperforms the LZ_2 in terms of linear regression. This could be explained by its robustness to low amplitude noise between the MUAPs. With a binary symbolizing procedure, low amplitude noise appears to cause a false sense of complexity.

Overall, the LZ complexity measure tracks virtual deterministic MUAP signatures (single or superimposed) and reflects primarily the duration and rate of creation of MUAPs in the MES. The results suggest that the duration and the rate of creation of MUAPs are affected mainly by the muscle fiber CV and myoelectric manifestation of muscle fatigue; this is consistent with the expansion of MUAPs due to the lowered muscle CV. The decrease in the LZ measure due to the fatigue could also be attributed to the formation of trivial correlations along the MES and higher degrees of determinism, which is likely caused by the MUAPs expanded in time; this also implies an increased degree of synchronization between the firing MUs. This is another factor contributing to the higher performance of the LZ measure, which reflects both changes of CV and synchronization of firing MUs. Previous studies have shown the MDN is not a reliable measure for synchrony [Merletti and Parker, 2004].

The results are also consistent with the results of experiment presented in Chapter 6. With the progress of fatigue the estimated Hurst exponent using DFA shows an increase, which implies,

the persistence of the MES is increased. This is also a confirmation that the correlation along the MES is increased with fatigue. A decreased deterministic complexity is also consistent with an increased persistence as both suggest the randomness of the signal is decreased. The LZ measure could be used in conjunction with the Hurst exponent for a better understanding of the fatigue effects on fractal and chaotic characteristics of the MES.

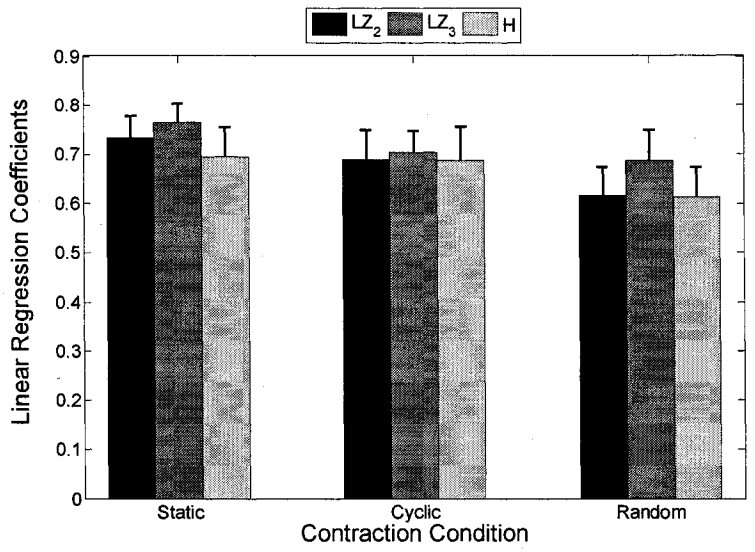

Figure 8.4: Comparison of LZ_2, LZ_3 and H, during static, cyclic and random contractions.

Comparison of the optimum Hurst exponent for fatigue estimation introduced in chapter 6 to the LZ measure is also interesting. Figure 8.4, depicts the average linear regression coefficients of LZ_2, LZ_3, and optimum Hurst exponent (H), across all subjects for all three tests and the inter-subject variability in the form of error bars. The number of cases where LZ_3 had a higher linear regression coefficient compared to optimum Hurst exponent are, 9/10 for static contractions, 6/10 for cyclic contractions, 8/10 for random contractions. The number of cases where LZ_2 had a higher linear regression coefficient compared to optimal Hurst exponent are, 7/10 for static

contractions, 4/10 for cyclic contractions, 5/10 for random contractions. The LZ_3 outperforms the optimum Hurst exponent in all contraction conditions. The LZ_2 outperforms the optimum Hurst during static contractions and its performance is comparable during cyclic and random contractions. Note the optimum Hurst exponent was computed for 4 s analysis windows while the LZ is computed for 5 s analysis windows.

8.5. Conclusions

In this chapter, the LZ complexity was proposed as a measure of muscular fatigue. The LZ complexity measure has demonstrated improvement over the conventional MDN for the assessment of myoelectric manifestation of fatigue. A ternary (3-symbol) LZ complexity measure was introduced. The use of a ternary symbolizing procedure accounts for low amplitude noise in the MES. This ternary LZ complexity measure outperforms the binary (2-symbol) LZ measure for fatigue monitoring.

The LZ measure is interesting as it reflects the myoelectric manifestation of fatigue caused by the changes of CV as well as MU synchronization, which is not present in conventional fatigue indices based on the frequency content. The LZ measure is computationally inexpensive. In addition, the LZ measure does not make any assumption of stationarity, unlike other analysis techniques (e.g., power spectrum estimations used to compute MDN). These characteristics of LZ measure makes it well suited for analysis of MES; especially during dynamic contractions, when the signal is highly non-stationary.

In terms of computational complexity, the most time consuming part of this approach is the parsing procedure. However, the overall required time is comparable to the Welch's method for power spectrum estimation and is not more than 10 s in for 5s signals.

Chapter 9

9. Conclusions and future directions

9.1. Conclusions

In this work, we have presented four major paradigms for multi-scale analysis of MESs schematically shown in Figure 9.1.

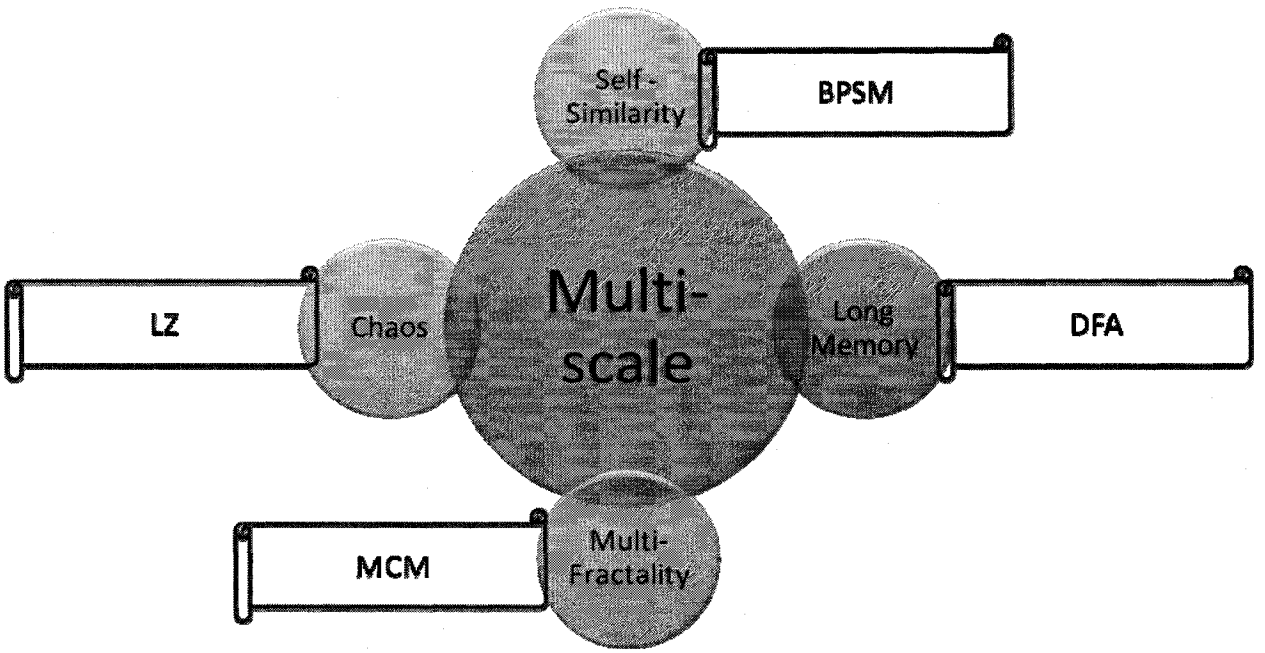

Figure 9.1: Schematics of the material presented in this work.

1. *Self-similarity*: A novel multi-scale bi-phase power-law was introduced which accurately characterizes surface MES power spectrum recorded during moderate contractions. We have presented the bi-phase power-law along with a novel methodology named BPSM. BPSM provides unique parameters that are distinctly sensitive to force, joint angle, and fatigue. These parameters could be used as complementary information for conventional

myoelectric parameters that are confounded when muscle moves during a prolonged contraction.

2. *Long memory*: A method for quantitative analysis of long memory, known as DFA was introduced in the context of MESs. It was shown the MESs show both mono- and multi-fractality. It was also shown the MESs are characterized with several fractal-scaling-breaks that could be exploited for fatigue estimation. A new approach for fatigue estimation was presented to compute an optimum Hurst exponent. The optimum Hurst exponent outperforms the MDN for fatigue estimation during cyclic and random contractions.

3. *Multi-fractality*: A unique multi-fractal process known as MCM was introduced in the context of MESs. It was demonstrated that the MESs show multiplicative multi-fractality. A framework for analysis of MESs using MCM was presented to utilize generalized dimension spectrum for discerning neuropathic conditions. This new framework has unique characteristics such as suppressing effects on interfering noise and outperforms the conventional NT for discerning neuropathic conditions in the presence of additive white noise.

4. *Chaos*: An interesting framework known as power-law sensitivity to initial condition was used to analyze MESs. This new framework suggests the MESs are not fully random or fully chaotic but they resemble random fractals and chaotic motions on different scales. The LZ measure was introduced as a substitute for time-dependent exponent curves in the context of MESs. It was shown that the binary LZ measure might be affected by a false sense of complexity due to inadequacy of two symbols to characterize MUAPs. A new

ternary LZ measure was introduced which resolves the limitations of the binary LZ measure. The LZ measure was also discussed for fatigue estimation. Our experiments confirmed anticipated features of the LZ measure to be well suited for fatigue estimation. The LZ measure outperforms conventional MDN for fatigue estimation during static, cyclic and random contractions.

Results demonstrate several potential applications and are promising for analysis of MESs and potentially other biological signals.

9.2. Future directions

1. *Self-similarity*: The bi-phase power-law is accurate when the MES power spectrum is approximately bi-phase. Alternative approaches could be taken to resolve this limitation for MES power spectrums that are not bi-phase. To exploit the MES power spectrum, an interesting potential approach is to introduce more fractional-orders and model the power spectrum. Other fractional-order differential equations that show multi-scale characteristics are yet to be found to improve the bi-phase power-law. The BPSM parameters need to be examined in conjunction with other parameters in the context of multi-parameter fatigue estimation similar to neural network-based approaches. This type of analysis is also attractive for other biological signals which do not show strict $1/f$ behaviour such as electroencephalograms.

2. *Long memory:* The MES is highly transient and multi-resolution analysis is often useful for analysis of this signal. Multi-scale analysis using multi-resolution approaches are expected to be well-suited for analysis of MES. Wavelet-based estimation of Hurst exponent needs to be examined in this case. The new approach for fatigue estimation

could be readily generalized for discerning pathological MESs. Further research should examine ability of DFA for this task.

3. *Multi-fractality*: The MCM model is restricted to time series. Future studies will examine generalization of MCM to multi-dimensions. This will be very interesting for multi-channel MESs. MCM is relatively new and it is interesting to examine this type of analysis for other biological signals as well.

4. *Chaos*: The time-dependent exponent curves must be further researched in the context of MESs. It is expected that a different form of representation such as transformation to scale-dependent Lyapunov exponents will improve the ability of exponent curves to characterize MESs. This type of analysis is also very new and needs to be further researched for analysis of MESs and other biological signals. Future research will also examine different parsing procedures for computing the LZ measure. The LZ measure could be also used along with the Hurst exponent and generalized dimension spectrum for more in-depth study of the effects of fatigue on multi-scale characteristics of MESs.

Each of the experiments presented in this work could be generalized to other contraction protocols or neuromuscular conditions. The simulated data could be altered to emulate myopathic conditions and different stages of a disorder. It is interesting to examine DFA and MCM in such cases. The contraction protocol could be also altered to be closer to muscle activity in daily life. For example it is interesting to record the activity of a muscle for hours and examine the changes of fatigue during a normal daily activity or an exercise.

Appendix A: Mono-phase power-law's probabilistic self-similarity and generation of syntactic FBM.

Derivations in this appendix are based on [Turner *et al.*, 1998]. Consider a time series $\{x(t)\}$ generated by a fractional-order differential equation in this form

$$\frac{d^q}{dt^q}x(t) = n(t), \qquad \text{(A.1)}$$

where $q > 0$, and $n(t)$ is white Gaussian noise with a constant power spectrum. When $1 < q < 2$ the solution to this fractional-order differential equation could be found in this form

$$\frac{d^q}{dt^q}x(t) = \frac{1}{2\pi}\int_{-\infty}^{+\infty}(ik)^q X(k)e^{(ikt)}dk, \qquad \text{(A.2)}$$

where $X(k)$ is the Fourier transform of $x(t)$ given by

$$X(k) = \int_{-\infty}^{+\infty}x(t)e^{(ikt)}dk. \qquad \text{(A.3)}$$

The k is the spatial frequency. Using this definition the solution to Eq.(A.1) becomes

$$x(t) = \frac{1}{2\pi}\int_{-\infty}^{+\infty}(ik)^{-q}N(k)e^{(ikt)}dk, \qquad \text{(A.4)}$$

where $N(k)$ is the Fourier transform of $n(t)$. The solution is expressed in terms of the inverse Fourier transform of the product of two functions, $(ik)^{-q}$ and $N(k)$. Application of convolution theorem allows us to write this result in this form

$$x(t) = \int h(t-y)n(y)dy, \qquad \text{(A.5)}$$

where h is given by

$$h(t)=\frac{1}{2\pi}\int_{-\infty}^{+\infty}(ik)^{-q}e^{(ikt)}dk\,. \qquad \text{(A.6)}$$

Substituting p for ik, $h(t)$ can be written in terms of the inverse Laplace transform of p^{-q}. Since

$$L\left[x^{q}\right]=\frac{\Gamma(q+1)}{p^{q+1}}, \qquad \text{(A.7)}$$

when q > 1, and Re{p} > 0, where L is taken to denote the Laplace transform and Γ is the Gamma function as

$$\Gamma(q)=\int_{0}^{+\infty}t^{q-1}e^{-t}dt\,. \qquad \text{(A.8)}$$

We can write

$$t^{q}=L^{-1}\left[\frac{\Gamma(q+1)}{p^{q+1}}\right], \qquad \text{(A.9)}$$

or

$$L^{-1}\left[\frac{1}{p^{q}}\right]=\frac{1}{\Gamma(q)}t^{q-1}\,. \qquad \text{(A.10)}$$

Thus the solution to Eq.(A.1) can be written in the form

$$x(t)=\frac{1}{\Gamma(q)}\int_{0}^{t}\frac{n(y)}{(t-y)^{1-q}}dy\,. \qquad \text{(A.11)}$$

This is the Liouville-Riemann transform and is an example of fractional integral. Now consider

$$x'(t) = \frac{1}{\Gamma(q)} \int_0^t \frac{n(\lambda y)}{(t-y)^{1-q}} dy, \qquad \text{(A.12)}$$

where λ is a scaling parameter. Substituting $z = \lambda y$, we obtain

$$x_\lambda(t) = \frac{1}{\lambda^q} \frac{1}{\Gamma(q)} \int_0^{\lambda t} \frac{n(z)}{(\lambda t - z)^{1-q}} dz = \frac{1}{\lambda^q} x(\lambda t). \qquad \text{(A.13)}$$

Since x(t) is a random process Eq.(A.13) is statistically satisfied or

$$\Pr\{x_\lambda(t)\} = \frac{1}{\lambda^q} \Pr\{x(\lambda t)\}, \qquad \text{(A.14)}$$

where Pr{.} denotes the probability distribution of samples. Eq.(A.14) is consistent with Eq.(3.4) introduced in chapter 3 and q is equal to the Hurst exponent. Moreover this procedure could be used to generate fractional Brownian motion as shown in Figure A.1.

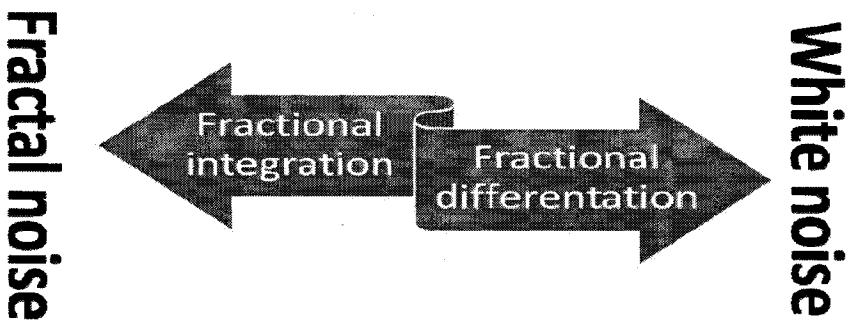

Figure A.1: Generating FBM (fractal noise) by filtering white noise.

Appendix B: Bi-phase power-law's extended probabilistic self-similarity.

Derivations in this appendix are based on a similar approach in [Turner *et al.*, 1998]. Consider the bi-phase power-law in this form

$$S(f)=c\left(\frac{f}{f_0}\right)^{2g}\Big/\left(\left(\frac{f}{f_0}\right)^{2}+1\right)^{q+g}. \qquad \text{(B.1)}$$

First, we rewrite the Eq.(B.1) by manipulating ($Q = q + g$, $G = g$, and $K = cf_0^{2q}$) in this form

$$S(f)=K\left(f^{2G}\right)\Big/\left(f^2+f_0^2\right)^{Q}. \qquad \text{(B.2)}$$

Eq. (B.2) corresponds to a noise type $x(t)$ which has complex Fourier spectrum in this form

$$X(f)=H(f)N(f), \qquad \text{(B.3)}$$

where $N(f)$ is the Fourier transform of white noise and $H(f)$ is a transfer function in this form

$$H(f)=\frac{(if)^G}{(f_0+if)^Q}. \qquad \text{(B.4)}$$

The solution to Eq.(B.3) is given by

$$x(t)=\frac{1}{2\pi}\int_{-\infty}^{+\infty}H(f)N(f)e^{ift}dk. \qquad \text{(B.5)}$$

If we consider the definition of a fractional derivative in terms of the inverse Fourier transform of $(if)^G$ the, using the convolution theorem we can write

$$x(t) = \int h(t-y)\frac{d^G}{dy^G}n(y)dy, \qquad \text{(B.6)}$$

where

$$h(t) = \frac{1}{2\pi}\int_{-\infty}^{+\infty}\frac{1}{(f_0 + if)^Q}e^{ift}df. \qquad \text{(B.6)}$$

Substitution of p for if allows us to write this result in terms of the inverse Laplace transform in this form

$$h(t) = L^{-1}\left[\frac{1}{(f_0 + p)^Q}\right]. \qquad \text{(B.7)}$$

Since

$$L\left[t^Q e^{-f_0 t}\right] = \frac{\Gamma(q+1)}{(f_o + p)^{Q+1}}, \qquad \text{(B.8)}$$

it follows that

$$h(t) = \frac{1}{\Gamma(q)}\frac{e^{-if_0 t}}{t^{1-Q}}. \qquad \text{(B.9)}$$

Hence $x(t)$ can be written in terms of the fractional integral transform as

$$x(t) = \frac{1}{\Gamma(Q)}\int_{-\infty}^{t}\frac{e^{[-f_0(t-y)]}}{(t-y)^{1-Q}}\frac{d^G}{dy^G}n(y)dy. \qquad \text{(B.10)}$$

The scaling characteristics of this transform could be investigated by considering the function

$$
\begin{aligned}
x'(t,f_0) &= \frac{1}{\Gamma(Q)}\int_{-\infty}^{t}\frac{e^{[-f_0(t-y)]}}{(t-y)^{1-Q}}\frac{d^G}{dy^G}n(\lambda y)dy \\
&= \frac{\lambda^G}{\lambda^Q}\frac{1}{\Gamma(Q)}\int_{-\infty}^{\lambda t}\frac{e^{[-(f_0)/\lambda(\lambda t-z)]}}{(\lambda t-z)^{1-Q}}\frac{d^G}{dz^G}n(z)dz \quad , \qquad \text{(B.11)} \\
&= \frac{\lambda^G}{\lambda^Q}x(\lambda t, f_0/\lambda)
\end{aligned}
$$

where z is substituted for λy. Hence there exists a statistical scaling relation in this form

$$
\Pr\{x'(t,f_0)\} = \frac{\lambda^G}{\lambda^Q}\Pr\{x(\lambda t, f_0/\lambda)\}, \qquad \text{(B.12)}
$$

where Pr{.} denotes the probability distribution of samples. Eq.(B.12) is consistent with the Eq.(3.11) introduced in Chapter 3 and shows some form of extended self-similarity.

Appendix C: Least square solution for the bi-phase power-law optimization.

Consider the bi-phase power-law in this form

$$S(f)=c\left(\frac{f}{f_0}\right)^{2g}\Big/\left(\left(\frac{f}{f_0}\right)^2+1\right)^{q+g}. \qquad \text{(C.1)}$$

First, we rewrite the Eq.(B.1) by manipulating ($Q = q + g$, $G = g$, and $K = cf_0^{2q}$) in this form

$$S(f)=K\left(f^{2G}\right)\Big/\left(f^2+f_0^2\right)^{Q}. \qquad \text{(C.2)}$$

Now, consider a logarithmic error function $e(Q, G, C, f_0)$ in the following form with $C = log\ K$,

$$e(Q,G,C,f_0)=\frac{1}{N}\sum_{i=1}^{N}\left(\log S(f_i)-\log\hat{S}(f_i)\right)^2, \qquad \text{(C.3)}$$

where $\hat{S}$ is the estimated power spectrum of the signal, S is the power spectrum of the model, N is the number of power spectrum samples, and f_i is the corresponding frequency of the i^{th} sample. Having an estimate for f_0 (the peak frequency f_m of $\hat{S}$ can be used for the first iteration), Eq. (3.15) is minimized when $\partial e/\partial G = \partial e/\partial Q = \partial e/\partial C = 0$. Differentiating Eq. (3.15) with respect to Q, G, and C, it is easy to show how these parameters can be estimated by a standard least squares approach and by solving a linear system of equations. Differentiating the error, the parameter set (G, Q, C) can be obtained from the solution of the following linear system of equation

$$\begin{bmatrix} a_{11} & a_{12} & a_{13} \\ a_{21} & a_{22} & a_{23} \\ a_{31} & a_{32} & a_{33} \end{bmatrix} \cdot \begin{bmatrix} G \\ Q \\ C \end{bmatrix} = \begin{bmatrix} b_1 \\ b_2 \\ b_3 \end{bmatrix}, \qquad \text{(C.4)}$$

where

$$a_{11} = \sum -2(\log f_i)^2$$
$$a_{12} = \sum \log\left(f_0^2 + f_i^2\right)\log f_i$$
$$a_{13} = \sum -\log f_i$$
$$a_{21} = \sum 2\log\left(f_0^2 + f_i^2\right)\log f_i$$
$$a_{23} = \sum \log\left(f_0^2 + f_i^2\right)$$
$$a_{13} = \sum -2\log f_i$$
$$a_{32} = \sum \log\left(f_0^2 + f_i^2\right)$$
$$a_{33} = \sum -1 = -N$$
$$b_1 = \sum -\log S(f_i)\log f_i$$
$$b_2 = \sum \log S(f_i)\log\left(f_0^2 + f_i^2\right)$$
$$b_3 = \sum \log S(f_i)$$

Note a similar solution is presented in [Turner *et al.*, 1998], which has some mistakes in it.

Appendix D: Published and submitted work.

Journal papers:

Published:

- **Talebinejad M.**, Chan A., Miri A., and Dansereau R. (2008) Fractal analysis of surface electromyography signals: A novel power spectrum-based method. *Journal of Electromyography and Kinesiology*, doi:10.1016/j.jelekin.2008.05.004.

Submitted:

- **Talebinejad M.**, Chan A., and Miri A. (2008) Fatigue estimation using a novel multi-fractal detrended fluctuation analysis-based approach. Submitted to the *Journal of Electromyography and Kinesiology*, JEK-D-08-00127.

- **Talebinejad M.**, Chan A., and Miri A. (2008) Multiplicative multi-fractal modeling of electromyography signals for discerning neuropathic conditions. Submitted to the *IEEE Transaction on Biomedical Engineering*, TBME-00789-2008.

- **Talebinejad M.**, Chan A., and Miri A. (2008) Fatigue estimation using Lempel-Ziv complexity measure. Submitted to the *Journal of Electromyography and Kinesiology*, JEK-D-08-00165.

Conference papers:

1. **Talebinejad M.**, Chan A., Miri A., and Dansereau R. (2006) Fractal analysis of myoelectric signals. *Canadian Medical and Biological Engineering Conference*, Vancouver, BC.

2. **Talebinejad M.**, Chan A., Miri A., and Dansereau R. (2006) Effects of force and joint angle on fractal parameters of myoelectric signals. *IEEE Engineering in Medical and Biology Society Conference*, New York, NY.

3. **Talebinejad M.**, Chan A., and Miri A. (2007) Effects of conduction velocity and spectral compression on fractal parameters of myoelectric signals. *Canadian Medical and Biological Engineering Conference*, Toronto, ON. (**Received an honourable mention at the student paper competition**)

4. **Talebinejad M.**, Miri A., and Chan A. (2008) A computationally efficient HMM-based handwriting verification system. *IEEE Instrumentation and Measurement Technology Conference*, Victoria, BC.

5. **Talebinejad M.**, Chan A., and Miri A. (2008) Fractal analysis of myoelectric signals using piece wise statistically self-affine power-laws. *Canadian Medical and Biological Engineering Conference*, Montreal, QC.

6. **Talebinejad M.**, Chan A., and Miri A. (2008) Multi-scale analysis of myoelectric signals: Assessment of long-range dependencies and fractal-scaling-break. *Canadian Medical and Biological Engineering Conference*, Montreal, QC. (**Received a third place at the student paper competition**)

7. **Talebinejad M.**, Chan A., and Miri A. (2008) Novel power spectrum-based fractal indicators for myoelectric parameters. *International Society of Electrophysiology and Kinesiology Congress*, Niagara Falls, ON.

8. **Talebinejad M.**, Chan A., and Miri A. (2008) Novel fractal indicators with distinct sensitivities to localized muscular fatigue during static contractions. *International Society of Electrophysiology and Kinesiology Congress*, Niagara Falls, ON.

References

Abásolo D., Hornero R., Gómez C., García M., and López M. (2006) Analysis of EEG background activity in Alzheimer's disease patients with Lempel-Ziv complexity and central tendency measure, *Med Eng Phys*, 28, 315–322.

Abel E., Meng H., Forster A., and Holder D. (2006) Singularity characteristics of needle EMG IP signals. *IEEE Trans Biomed Eng*, 53, 219-225.

Aboy M., Hornero R., Abásolo D., and Álvarez D. (2006) Interpretation of the Lempel-Ziv complexity measure in the context of biomedical signal analysis. *IEEE Trans Biomed Eng*, 53, 2282–2288.

Akay M. (1996) *Detection and estimation methods for biomedical signals*. Academic Press.

Amigo J.M., Szczepaski J., Wajnryb E., and Sanchez-Vives M.V. (2004) Estimating the entropy rate of spike trains via Lempel-Ziv complexity. *Neural Comput,* 16, 717-736.

Anmuth C., Goldberg G., and Mayer N. (1994). Fractal dimension of EMG signals recorded with surface electrodes during isometric contractions is linearly correlated with muscle activation. *Muscle Nerve*, 17, 953-954.

Arabadzhiev T.I., Dimitrov G.V., Dimitrov A.G., Chakarov V.E., and Dimitrova N.A. (2008) Factors affecting the turns analysis of the interference EMG signal. *Biomedical Signal Processing and Control*, 3, 145-153.

Arendt-Nielsen L., and Mills K.R. (1985) The relationship between mean power frequency of the EMG spectrum and muscle fiber conduction velocity. *Electroencephalogr Clin Neurophysiol*, 60, 130-134.

Arikidis N., Abel E., and Forster A. (2002) Interscale wavelet maximum—a fine to coarse algorithm for wavelet analysis of the EMG interference pattern. *IEEE Trans Biomed Eng,* 49, 337-344.

Barenblatt G.I. (2003) *Scaling*. Cambridge University Press.

Bassingthwaighte J.B., Liebovitch L.S., and West B.J. (1994) *Fractal physiology*. Oxford University Press.

Bilodeau M., Arsenault A.B., Gravel D., and Bourbonnais D. (1991) EMG power spectra of elbow extensors during ramp and step isometric contractions. *Eur J Appl Physiol*, 63, 24-28.

Bonato P. (2001) Recent advancements in the analysis of dynamic EMG data. *IEEE Eng Med Biol Mag*, 20, 29–32.

Bonato P., D'Alessio T., and Knaflitz M. (1998) A statistical method for measurement of muscle activation intervals from surface myoelectric signal during gait. *IEEE Trans Biomed Eng,* 45, 287-299.

Bonato P., Gagliati G., Knaflitz M. (1996) Analysis of myoelectric signals recorded during dynamic contractions. *IEEE Eng Med Biol Mag*, 15, 102-111.

Bonato P., Roy S.H., Knaflitz M., and De Luca C.J. (2001) Time-frequency parameters of the surface myoelectric signal for assessing muscle fatigue during cyclic dynamic contractions. *IEEE Trans Biomed Eng*, 48, 745–753.

Burk R.E. (1981) Motor units: Anatomy, physiology and functional organization. in Brooks V.B. *Handbook of physiology: The nervous system.* American Physiological Society 345-422.

Cencini M., Falcioni M., Olbrich E., Kantz H., and Vulpiani A. (2000) Chaos or noise: Difficulties of a distinction. *Phys Rev E*, 62, 427-437.

Chan A., and Green G. (2007) Myoelectric control development toolbox. *31th Can Med Biol Eng Conf*, M0056.

Chan A., Englehart K., Hudgins B., and Lovely D. (2006) Multi-expert automatic speech recognition using acoustic and myoelectric signals. *IEEE Trans Biomed Eng,* 53, 676-685.

Chang, Y.C., and Chang, S. (2002) A fast estimation algorithm on the Hurst parameter of discrete-time fractional Brownian motion. *IEEE Trans Signal Proc,* 50, 554-559.

Chang, S., Hu, S.J., and Lin, W.C. (2004) Fractal dynamics and synchronization of rhythms in urodynamics of female Wistar rats. *J Neuro Meth,* 139, 271-279.

Chang, S., Li, S.-J., Chiang, M.-J., Hu, S.-J., and Hsyu, M.-C. (2007) Fractal dimension estimation via spectral distribution function and its application to physiological signals. *IEEE Trans Biomed Eng,* 54, 1895-1898.

Chang, S., Mao, S.T., Hu, S.J., Lin, W.C., and Cheng, C.L. (2000) Studies of detrusor-sphincter synergia and dyssynergia during micturition in rats via fractional Brownian motion. *IEEE Trans*

Biomed Eng, 47, 1066-1073.

Chen Z., Hu K.,. Carpena P., Bernaola-Galvan P., Stanley H.E., and Ivanov P.C. (2005) Effects of non-linear filters on detrended fluctuation analysis, *Phys Rev E*, 71 011104.

Chen Z., Ivanov P.C., Hu K., and Stanley H.E. (2002) Effects of non-stationeries on detrended fluctuation analysis, *Phys Rev E*, 65 041107.

Christodoulou I.C., and Pattichis C.S. (1999) Unsupervised pattern recognition for classification of EMG signals. *IEEE Trans Biomed Eng*, 46, 169-178.

Clancy E.A., and Farry K.A. (2000) Adaptive whitening of electromyogram to improve amplitude estimation. *IEEE Trans Biomed Eng*, 47, 709-719.

Clancy E.A., and Hogan N. (1999) Probability density of the surface electromyogram and its relation to amplitude detectors. *IEEE Trans Biomed Eng,*46, 730-739.

Costa M., Goldberger A.L., and Peng C.K. (2005) Multiscale entropy analysis of biological signals. *Phys Rev E*, 71, 021906.

De Luca C. J. (1984) Myoelectrical manifestations of localized muscular fatigue in humans. *CRC Crit Rev Biomed Eng*, 11, 251–279.

De Luca C. J. (1979) Physiology and mathematics of myoelectric signals. *IEEE Trans Biomed Eng,* 26, 313-326.

Duda R.O., Hart P.E., and Stork D.G. (2001) *Pattern classification.* Wiley.

Englehart, K., Hudgins, B., and Chan A.D.C. (2003) Continuous Multifunction Myoelectric Control using Pattern Recognition. *Technology and Disability*, 15, 95-103.

Englehart, K., and Hudgins B. (2003) A robust, real time control scheme for multifunction myoelectric control. *IEEE Trans Biomed Eng*, 50, 848- 854.

Englehart, K., Hudgins, B., and Parker, P.A (2001) A Wavelet Based Continuous Classification Scheme for Multifunction Myoelectric Control. *IEEE Trans Biomed Eng,* 48, 302-311.

Englehart K.B., and Parker P.A. (1994) Single motor unit myoelectric signal analysis with nonstationary data. *IEEE Trans Biomed Eng,* 41, 168-180.

Farina D., Cescon C., and Merletti R. (2002) Influence of anatomical, physical and detection system parameters on surface EMG. *Biol Cybern*, 86, 445-456.

Farina D., Crosetti A., and Merletti R. (2001) A model for the generation of synthetic intramuscular EMG signals to test decomposition algorithms. *IEEE Trans Biomed Eng,* 48, 66-77.

Farina D., Fattorini F., Felici F., and Fillogoi G.C. (2002) Nonlinear surface EMG analysis to detect changes of motor unit conduction velocity and synchronization. *J Appl Physiol*, 93, 1753-1763.

Farina D., and Merletti R. (2000) Comparison of algorithms for estimation of EMG variables during isometric contractions. *J Electromyogr Kinesiol*, 10, 337-350.

Farina D., and Merletti R. (2001) Effects of electrode shape on spectral features of surface detected motor unit action potentials. *Acta Physiol Phamacol Bulg*, 26, 63-66.

Farina D., Merletti R., Nazzaro M., and Caruso I. (2001) Effects of joint angle on EMG variables in muscles of the leg and thigh. *IEEE Eng Med Biol Mag*, 20, 62-71.

Farina D., Muhammad W., Fortunato E., Meste E., Merletti R., and Rix H. (2001) Estimation of single motor unit conduction velocity from the surface EMG signal detected with linear electrode arrays. *Med Biol Eng Comput*, 39, 225-236.

Finsterer J. (2001) EMG-interference pattern analysis. *J Electromyogra Kinesio*, 11, 231-246.

Gao J.B. (1997) Recognizing randomness in a time series. *Physica D*, 106, 49-56.

Gao J.B. (2000) Multiplicative multifractal modeling of long-range-dependent traffic in computer communication networks. PhD dissertation, EE Dept, UCLA.

Gao J.B., Hu J., Tung W.W., Cao Y.H. (2005) Power-law sensitivity to initial condition in a time series with applications to epileptic seizure detection. *Physica A*, 353, 613-624.

Gao J.B., Hu J., Tung W.W., Cao Y.H. (2006) Distinguishing chaos from noise by scale-dependent Lyapunov exponent. *Phys Rev E* , 4, 066204.

Gao J.B., Hu J., Tung W.W., Cao Y.H. (2006) Assessment of long range correlation in time series: How to avoid pitfalls. *Phys Rev E*, 73, 016117.

Gao J.B., and Royshowdhury V.P. (2000) Multifractal gene finder, Technical report. Electrical Engineering Department, UCLA.

Gao J.B., Yinhe C., Ten W., and HU J. (2007) Multiscale analysis of complex time series. New Jersey: Wiley Press.

Gitter, J., and Czerniecki, M. 1995. Fractal analysis of the electromyographic interference pattern. *J Neurophysio Meth*, 58, 103-108.

Gupta, V., Suryanarayanan, S., and Reddy, N. 1997. Fractal analysis of surface EMG signals from the biceps. *International Journal of Medical Informatics*, 45, 185-192.

Hamilton-Wright A., and Stashuk D. (2005) Physiologically based simulation of clinical EMG signals. *IEEE Trans Biomed Eng*, 52, 171-182.

Hamilton-Wright A., and Stashuk D. (2006) A decision support framework for clinical needle EMG. *IEEE Trans Biomed Eng*, 24, 116-121.

Henneman E. (1981) Recruitment of motoneurons: The size principle. In: Motor unit types, recruitment, and plasticity in health and disease. *Progr Clin Neurophysiol*, 9, 26-60.

Hu J. (2007) new approaches to Multiscale signal processing. PhD dissertation, EE Dept, University of Florida.

Hu J., Gao J.B., and Pricipe J.C. (2006) Analysis of biomedical signals by the Lempel-Ziv complexity: The effect of finite data size. *IEEE Trans Biomed Eng,*53, 2606-2609.

Hu K., Ivanov P.C., Chen Z., Carpena P., and Stanley H.E. (2001) Effects of trend on detrended fluctuation analysis. *Phys Rev E* ,64, 011114.

Hudgins B., Parker P., and Scott R. (1993) A new strategy for multifunction myoelectric control. IEEE Trans Biomed Eng, 40, 82-94.Hwa R.C., and Ferree T.C. (2002) Scaling properties of fluctuations in the human electroencephalogram. *Phys Rev E* ,66, 021901.

Kantelhardt J.W., Bunde E., Rego H.H.A., Havlin S., and Bunde A. (2001) Detecting long-range correlations with detrended fluctuation analysis. *Physica A*, 295, 441-454.

Kantelhardt J.W., Zschiegner S.A., Bunde E., Havlin S., Bunde A., and Stanley H.E. (2002) Multifractal detrended fluctuation analysis of nonstationary time series. *Physica A*, 316, 87-114.

Karlsson S., Yu J., and Akay M. (1999) Enhancement of spectral analysis of myoelectric signals during static contractions using wavelet methods. *IEEE Trans Biomed Eng,*46, 670-684.

Karlsson S., Yu J., and Akay M. (2000) Time-frequency analysis of myoelectric signals during dynamic contractions: A comparative study. *IEEE Trans Biomed Eng,* 47, 228-238.

Lempel A., and Ziv J. (1976) On the complexity of finite sequences. *IEEE Trans Info Theory*, 22, 75-81.

MacIsaac D., Parker P., and Scott R., (2001a) The short-time Fourier transform and muscle fatigue in dynamic contractions, *J Electromyogr Kinesiol*, 11, 439–449.

MacIsaac D., Parker P., Scott R., Englehart K., and Cechetto A. (2001b) Influence of dynamic factors on myoelectric signal estimation, *IEEE Eng Med Biol Mag*, 20, 84–89.

MacIsaac D., Parker P., Englehart K., Rogers D. (2006) Fatigue estimation with a multivariable myoelectric mapping function, *IEEE Trans Biomed Eng*, 53, 694-700.

Mandelbrot B.B. (1974) Intermittent turbulence in self-similar cascades: Divergence of high moments and dimension of carrier. *J Fluid Mech*, 62, 331-358.

Mandelbrot B.B. (1982) *The fractal geometry of nature*. Freeman.

Mandelbrot B.B. (1997) *Fractals and scaling in finance*. Springer.

Mandelbrot B.B., and Ness V. (1968) Fractional Brownian motions, fractional noises and applications. *SIAM Rev*, 10, 422-437.

Merletti R., Gulisashvili A., and Lo Conte L.R. (1995) Estimation of shape characteristics of surface muscle signal spectra from time domain data. *IEEE Trans Biomed Eng,* 42, 769-776.

Merletti R., Farina D., Gazzoni M., and Schieroni M.P. (2002) Effects of age on muscle functions investigated with surface electromyography. *Muscle Nerve*, 25, 65-76.

Merletti R., Holobar A., and Farina D. (2008) Two dimensional high density surface EMG (HD-EMG) technology and applications. *Proc XVIIth ISEK Congr*, BLK1.1.

Merletti R., and Parker P. (2004) *Electromyography: Physiology, engineering and noninvasive applications*. IEEE Press Series in Biomedical Engineering.

Mesin L., Cescon C., Gazzoni M., Merletti R., and Rainoldi A. (2008) A new method to estimate myoelectric manifestation of muscle fatigue. *Proc XVIIth ISEK Congr*, MFO1.5.

Monson H. (1996) *Statistical Digital Signal Processing and Modeling*. Wiley Press, New York.

Nagarajan R. (2002) Quantifying physiological data with Lempel-Ziv complexity: Certain issues. *IEEE Trans Biomed Eng,* 49, 1371-1373.

Okajima Y., Tomita Y., Ushijima R., and Chino N. (2000) Motor unit sound in needle electromyography: Assessing normal and neuropathic units. *Muscle Nerve*, 23, 1076-1083.

Oswiecimka P., Kwapien J., and Drozdz S. (2005) Multifractality in the stock market: Price increments versus waiting times. *Physica A*, 347, 626-638.

Peng C.K., Buldyrev S.V., Havlin S., Simons M., Stanley H.E., and Goldberger A.L. (1994) Mosaic Organization of DNA nucleotides. Phys Rev E, 49, 1685-1689.

Potvin J.R., and Brown S.H.M. (2004) Less is more: high pass filtering to remove up to 99% of the surface EMG signal power, improves EMG-based biceps brachii muscle force estimates. *J Electromyogr Kinesiol*, 14, 389-399.

Proakis J.G., and Manolakis D.K. (2006) *Digital signal processing*. Prentice Hall.

Rangayyan R. (2005) *Biomedical signal analysis: A case study approach*. IEEE Press.

Ravier P., Buttelli O., Jennane R., and Couratier P. (2005) An EMG fractal indicator having different sensitivities to changes in force and muscle fatigue during voluntary static muscle contractions. *J Electromyogr Kinesiol*, 15, 210-221.

Scheme E., Hudgins B., and Parker P. (2007) Myoelectric signal classification for phoneme-based speech recognition. *IEEE Trans Biomed Eng*, 54, 694-699.

She Z., Jackson E., and Orszag S. (1991) Structure and dynamics of homogeneous turbulence: Model and simulations. *Proc R Soc Lond A*, 434, 101-124.

Shields, R. 2006. Fractal dimension of the EMG interference pattern: preliminary observations and comparisons with other measures of interference pattern analysis. *Journal of Clinical Neurophysiology*, 10, 117-118.

Sprott J.C, (2003) *Chaos and time series analysis*. Oxford University Press.

Stalberg E., and Falck B. (1997) The role of electromyography in neurology. *Electroencephalo Clin Neurophysio*, 103, 579–598.

SzcZepaski J., Amigo J.M., Wajnryb E., and Sanchez M.V. (2003) Application of Lempel-Ziv complexity to the analysis of neural discharges. *Networks*, 14, 335-350.

Talebinejad M., Miri A., Chan A. (2008a) Multi-scale analysis of myoelectric signals: Assessment of long-range dependencies and fractal-scaling-break. *31th Can Med Biol Eng Conf*, A4-5.

Talebinejad M., Miri A., Chan A. (2008b) Spectrum-based fractal analysis of myoelectric signals using piecewise statistically self-affine power-laws. *31th Can Med Biol Eng Conf*, A8-3.

Talebinejad M., Miri A., Chan A. (2008c) Novel power spectrum-based fractal indicators for myoelectric parameters. *Proc XVIIth ISEK Congr*, MFO5.

Talebinejad M., Miri A., Chan A. (2008d) Novel fractal indicators with distinct sensitivities to localized muscular fatigue during static contractions. *Proc XVIIth ISEK Congr*, MFO12.

Talebinejad M., Chan A., Miri A. (2007) Effects of conduction velocity and spectral compression on fractal parameters of myoelectric signals. *30th Can Med Biol Eng Conf*, M0087.

Talebinejad M., Chan A., Miri A., and Dansereau R. (2006a) Fractal analysis of myoelectric signals. *29th Can Med Biol Eng Conf*, SC-8.1.

Talebinejad M., Chan A., Miri A., Dansereau R. (2006b) Effects of force and joint angle on fractal parameters of myoelectric signals. *IEEE Conf Eng Biol Soc*, 3423-3426.

Talebinejad M., Chan A., Miri A., Dansereau R. (2008e) Fractal analysis of surface electromyography signals: A novel power spectrum-based method. *J Electromyogr Kinesiol*, doi:10.1016/j.jelekin.2008.05.004.

Talkner P., and Weber R.O. (2000) Power spectrum and detrended fluctuation analysis: Applications to daily temperatures. *Phys Rev E*, 62, 150-160.

Tatom F. (1989) The application of fractional calculus to the simulation of stochastic processes. Technical Report, Huntsville: Engineering Analysis Inc.

Tsallis C., Plastino A.R., and Zheng W.M. (1997) Power-law sensitivity to initial condition: New entropic representation. *Chaos Solitons Fractals*, 8, 885-891.

Turner M., Blackledge J., and Andrews P. (1998) *Fractal geometry in digital imaging.* Academic Press.

Xu Z., and Xiao S. (1997) Fractal dimension of surface EMG and its determinants, *IEEE Engineering in Medicine and Biology Conference*, 1570-1573.

Zhang X.S., Roy R.J., and Jensen E.W. (2001) EEG complexity as a measure of depth of anesthesia for patients. *IEEE Trans Biomed Eng,* 46, 548-555.

Zheng Y., Gao J.B., Sanchez J.C., principe J.C, and Okun M.S. (2005) Multiplicative multifractal modeling and discrimination of human neural activity. *Phys Rev Lett A*, 344, 253-264.

Zwarts M.J., Drost G., and Stegeman D.F. (2000) Recent progress in the diagnostic use of surface EMG for neurological diseases. *J Electromyogr Kinesiol*, 10, 287-291.